Title
Minimum Bias Measurements with the ATLAS Detector at the CERN Large Hadron Collider

Author
Leyton, Michael A.

Publication Date
2009

Peer reviewed|Thesis/dissertation

Minimum Bias Measurements with the ATLAS Detector at the CERN Large Hadron Collider

by

Michael A. Leyton

B.S. (Stanford University) 2003
M.A. (University of California, Berkeley) 2006

A dissertation submitted in partial satisfaction of the
requirements for the degree of
Doctor of Philosophy

in

Physics

in the

GRADUATE DIVISION
of the
UNIVERSITY OF CALIFORNIA, BERKELEY

Committee in charge:
Professor James L. Siegrist, Chair
Professor Robert G. Jacobsen
Professor Eugene E. Haller

Fall 2009

Minimum Bias Measurements with the ATLAS Detector

at the CERN Large Hadron Collider

by

Michael A. Leyton

Abstract

Minimum Bias Measurements with the ATLAS Detector

at the CERN Large Hadron Collider

by

Michael A. Leyton

Doctor of Philosophy in Physics

University of California, Berkeley

Professor James L. Siegrist, Chair

The Large Hadron Collider (LHC) at CERN[1] will collide bunches of protons (p) at a center-of-mass energy of $\sqrt{s} = 14$ TeV and a rate of 40 MHz. The unprecedented collision energy and interaction rate at the LHC will allow us to explore the TeV mass scale and take a major step forward in our understanding of the fundamental nature of matter. The initial physics run of the LHC is expected to start in November 2009 and continue until the end of 2010, with collisions at $\sqrt{s} = 900$ GeV, 7 TeV and 10 TeV.

ATLAS (A Toroidal LHC ApparatuS) is a 4π general-purpose detector designed for studying LHC collisions at the particle level. The design and layout of ATLAS are intended to cover the wide spectrum of physics signatures that are possible at the TeV mass scale. Construction and installation of the ATLAS detector at CERN are now complete.

This dissertation focuses on measuring the properties of inelastic pp interactions at the LHC with the ATLAS detector. A method for measuring the central pseudorapidity density $\frac{\mathrm{d}N_{\mathrm{ch}}}{\mathrm{d}\eta}$ and

[1] Organisation Européenne pour la Recherche Nucléaire

transverse momentum spectrum $\frac{\mathrm{d}N_{\mathrm{ch}}}{\mathrm{d}p_T}$ of charged particles during early, low-luminosity running of the LHC is described herein. The method also extracts the transverse-momentum dependence of the charged-particle invariant yield $E\frac{\mathrm{d}^3N_{\mathrm{ch}}}{\mathrm{d}^3p}$.

The analysis presented here has been prepared using a full detector simulation. Triggers used to select inelastic interactions are described and evaluated using a sample of simulated events. ATLAS reconstruction software is briefly discussed and used to reconstruct the simulated data. A set of track selection criteria is defined and the performance of the reconstruction is evaluated in terms of tracking efficiency and background contamination. A track-based analysis to measure the inclusive distributions is presented and then validated using the simulated event sample. Finally, various sources of systematic uncertainties are estimated and discussed.

Professor James L. Siegrist
Dissertation Committee Chair

to Anna and Ferran,

my love and my light.

Contents

List of Figures

List of Tables

Acknowledgments

First and foremost, I thank my advisor Jim Siegrist for his eternal words of wisdom and encouragement throughout these many years. His easy-going attitude and *laissez-faire* philosophy helped me endure six years of graduate school with minimal (but a non-zero number of) freak-outs.

Many thanks to Kevin Einsweiler, Gil Gilchriese and Ulrich Husemann, who all served as informal secondary advisors during my studies. I also thank William Bell, Craig Buttar, Beate Heinemann, Sami Kama, Regina Kwee, Arthur Moraes, Peter Steinberg and the Minimum Bias group for many fruitful discussions, as well as the continuous stream of comments and corrections. I also take this opportunity to thank the thousands of physicists, engineers, technicians and students working on ATLAS and the LHC, who collectively put in countless hours of their time and effort into the design, construction, installation and commissioning of these projects.

On a personal note, I give thanks to Mom and Dad, my two pillars of support, who made all of this a possibility for me. And to Anna and Ferran, the motivational driving force behind my finishing this dissertation, who stood by me through thick and through thin.

Introduction

Experiments in modern particle physics have allowed us to probe nature at its most fundamental level, from the early scattering experiments of Ernest Rutherford, to the development of the cyclotron by Ernest O. Lawrence, to modern-day synchrotrons, fixed-target accelerators and two-beam colliders. In this time, the complexity of particle physics experiments has grown exponentially. Today, particle accelerators such as the Large Hadron Collider (LHC) require tens of years of research and development by international collaborations made up of several thousand people.

The LHC will accelerate protons to velocities near the speed of light and collide them at high energies. By studying these collisions in detail, we can learn about the origin of the universe and the fundamental forces of nature. Detectors situated around the interaction point are used to reconstruct the collisions at the particle level. ATLAS (A Toroidal Lhc ApparatuS) is one of four such detectors at the LHC. The high energies, interaction rates, radiation doses, and particle multiplicities expected from the harsh environment at the LHC have set new standards for the design of detectors such as ATLAS.

Construction and installation of the ATLAS detector are now complete. While some data with cosmic rays has been taken in 2008 and 2009, the experiment enthusiastically awaits data from the LHC. In preparation, the simulation and online/offline reconstruction software for ATLAS have been written. Many recent changes to the software technology and framework have also been incorporated that reflect a more accurate modeling of the detector. A greatly improved understanding of

calibration and alignment techniques is now in place and their practical impact on the performance of the detector has been studied.

The focus of this dissertation is on measuring the properties of proton-proton interactions at the LHC with the ATLAS detector. The analysis presented here is possible with very early data, ideally from low-luminosity running of the LHC. These measurements are important for understanding the physics behind the proton-proton collisions, as well as for commissioning the ATLAS detector. They are also useful for studying properties of the underlying event, since these interactions will be a major background for all other studies at the LHC. The studies reported here are based on a full simulation of the ATLAS detector.

The outline of this thesis is as follows:

- Chapter 1 gives a brief overview of the LHC accelerator complex and the ATLAS detector. Focus is given to the components of the detector that are crucial for the analysis.
- Chapter 2 explains some of the background and theory important for the measurement. Monte Carlo simulation of LHC data is presented and discussed.
- Chapter 3 describes how events for the analysis are triggered and selected. Efficiencies and acceptances of the trigger are evaluated using simulated data.
- Chapter 4 describes how charged particle tracks are reconstructed in ATLAS.
- Chapter 5 studies the performance of the reconstruction software using simulated inelastic events. Selection criteria for reconstructed tracks used in the analysis are also given.
- Chapter 6 details the analysis procedure for applying corrections to the selected data. Results of the analysis are presented and discussed.
- Chapter 7 discusses the sources of various systematic uncertainties on the measurement. An estimate is given for each source and a total systematic uncertainty is assigned.

- Chapter 8 describes how the analysis of measured data will differ from the simulated analysis presented here. A series of cross-checks are proposed that will help minimize the uncertainty on the measurement.

Part I

Background

Chapter 1

ATLAS & LHC

The Large Hadron Collider will extend the frontiers of particle physics into new energy regimes, allowing us to fully explore the TeV mass scale. A wide spectrum of physics signatures are possible at this energy scale, including some coming from new physics phenomena. These processes have been used to guide the design and physics requirements of the ATLAS detector. In this chapter, a brief overview of the LHC complex and the ATLAS detector is given, with special focus on the detector sub-systems that are needed for the analysis.

1.1 Large Hadron Collider

The Large Hadron Collider (LHC) [1, 2] is the main accelerator complex at CERN[1]. The LHC will accelerate two counter-rotating proton (p) beams and collide them head-on at a center-of-mass energy of $\sqrt{s} = 14$ TeV and a rate of 40 MHz. Collisions will take place at four points along the ring. The LHC will also collide heavy ions (A) at an energy of 5.5 TeV per nucleon pair.

The main parameters of the LHC accelerator are given in Table 1.1. Both the center-of-mass energy ($\sqrt{s}$) and the luminosity ($\mathcal{L}$) are unprecedented for a hadron collider. An average of about

[1] Organisation Européenne pour la Recherche Nucléaire, near Geneva, Switzerland

18 interactions per bunch crossing are expected at the design luminosity of $\mathcal{L} = 10^{34}$ cm^{-2}s^{-1} [3]. A bunch spacing of only 25 ns means that there will be about 10^9 proton-proton interactions per second. This high luminosity is needed to observe many of the rare and interesting physics processes that are possible at the LHC energy scale.

Parameter	**Value**	**Unit**
Circumference	26659	m
Beam energy	7	TeV
Injection energy	0.45	TeV
Dipole field at 0.45 TeV	0.535	T
Dipole field at 7 TeV	8.33	T
Helium temperature	1.8	K
Coil aperture	56	mm
Distance between apertures	194	mm
Luminosity	10^{34}	cm^{-2}s^{-1}
Luminosity lifetime	10	h
Bunch spacing	25	ns
Particles per bunch	10^{11}	
Bunches per beam	2808	

Table 1.1: Main parameters of the LHC. Taken from [1].

The acceleration of protons inside the LHC takes place in various stages of the accelerator complex. Bunches of 10^{11} protons are first accelerated to an energy of 50 MeV by a dedicated linear accelerator. The proton bunches are then transferred to the Proton Synchotron Booster, which increases the energy to 1.4 GeV. The Proton Synchotron accelerates the protons to an energy of 26 GeV before injecting them into the Super Proton Synchrotron (SPS), where they are accelerated to 450 GeV. The SPS then injects the protons into the LHC ring in both clockwise and counter-clockwise directions. There they are accelerated to their final energy of 7 TeV. 1200 dipole magnets along the LHC ring ensure that the protons stay on track. The dipoles provide a magnetic field of up to 9 T.

Construction of the LHC was completed in Summer 2008 in the same tunnel that was used for the Large Electron Positron (LEP) accelerator. A brief commissioning run took place immediately afterwards, but was interrupted due to a critical magnet failure. The initial physics run of the LHC

is currently expected to start in November 2009 [4]. First collisions will take place at $\sqrt{s} = 900$ GeV, followed immediately by collisions at $\sqrt{s} = 7$ TeV. Once a significant data sample has been collected and the operations team has gained experience with running the machine, the center-of-mass energy will be ramped up to $\sqrt{s} = 10$ TeV.

Four large-scale detectors have been constructed at the beam collision points: ALICE, ATLAS, CMS and LHCb. Figure 1.1 shows a schematic layout of the LHC and the four detectors. ATLAS [5, 6] and CMS [7, 8] are general-purpose detectors with 4π coverage, designed for high-luminosity studies at the LHC. The design and layout of ATLAS and CMS are meant to cover a wide range of physics. The ATLAS detector is described in more detail in the following sections.

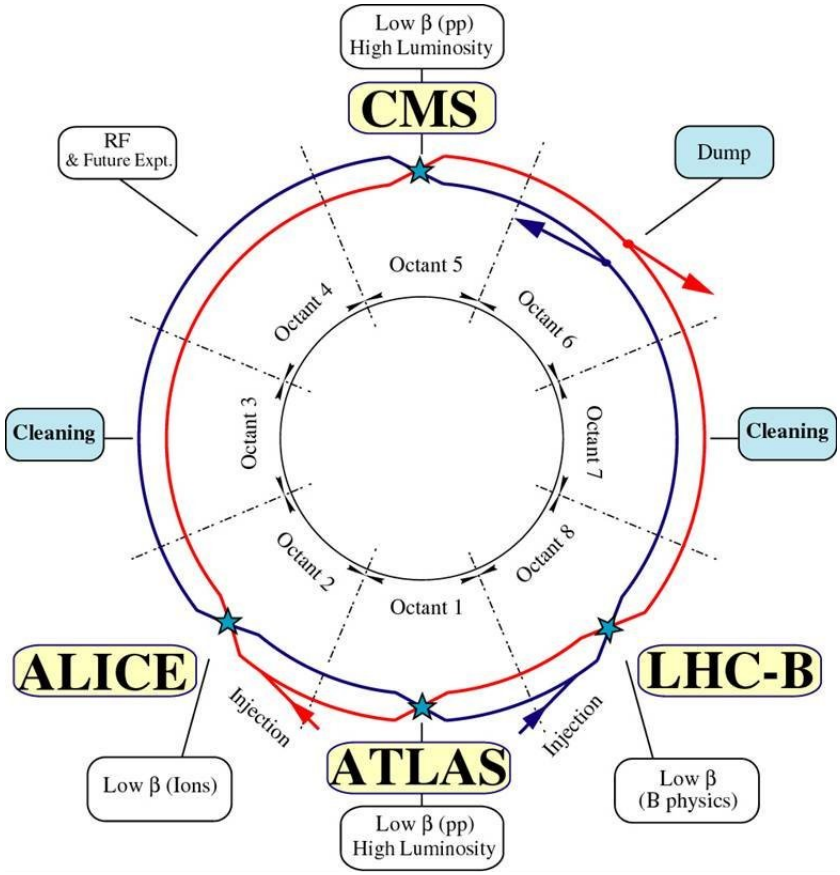

Figure 1.1: Schematic layout of the LHC complex with its four experiments: ALICE, ATLAS, CMS and LHCb. Taken from [2].

The LHCb detector [9,10] is dedicated to studying CP-violation in the B-system. Its design is therefore optimized for the measurement of B-mesons. Because the production and decay vertices of B-mesons are difficult to reconstruct when there is more than one interaction per bunch crossing, LHCb uses a lower luminosity of about $\mathcal{L} = 10^{32}$ cm^{-2}s^{-1} by defocusing the proton beams near the interaction point.

The ALICE detector [11,12] will study the quark-gluon plasma by detecting particles that are produced in heavy-ion collisions at the LHC. The quark-gluon plasma is a hadronic state where quarks and gluons are no longer in bound states (such as in protons), but instead move freely in a plasma. The extreme energy densities in heavy-ion collisions should be sufficient to create a quark-gluon plasma for a fraction of a second.

1.2 Physics at the LHC

The unprecedented center-of-mass energy and luminosity of the LHC will provide a rich physics potential, ranging from more precise measurements of Standard Model parameters to the search for new physics phenomena [6]. The Standard Model is our current picture of the elementary particles and their interactions. Although it is well-established for many years now, the LHC will allow more precise measurements and tests of the theory. The high luminosity and enhanced cross sections at the LHC will produce a large number of interactions and a large sample of statistics with which to precisely test Quantum Chromodynamics (QCD), electroweak interactions and flavor physics. For example, the top quark will be produced at the LHC at a rate of a few tens of Hz, providing the opportunity to test its couplings and spin.

One of the main motivations behind the LHC is to investigate the origin of particle masses. In the Standard Model, mass is given to particles by the Higgs mechanism, which predicts the existence of a Higgs boson (H). The LHC will be able to discover or exclude a Higgs boson in the mass range 110 GeV/c^2 $< m_H <$ 1 TeV/c^2 [2]. Because the search for the Higgs boson is a

particularly important part of the physics program at the LHC, it has been used as a benchmark to establish the performance of various LHC detector sub-systems. It is particularly useful for this type of design studies since there is a range of Higgs production and decay mechanisms that depend on m_H. The LHC detectors must be able to identify the $H \rightarrow \gamma\gamma$ decay channel, as well as the $H \rightarrow ZZ \rightarrow llll$ decay channel, for all possible Higgs mass ranges.

Discovery of physics beyond the Standard Model is also an important part of the LHC program. For example, new heavy gauge bosons W' and Z' could be accessible for masses up to about 6 TeV/c^2 [6]. The theory of supersymmetry, which relates fermions and bosons, also predicts new particles to be found in the TeV mass range. This theory postulates that for each particle p with spin s there exists a supersymmetric partner particle $\tilde{p}$ with spin $|s - 1/2|$ (e.g. q $(s = 1/2)$ $\rightarrow \tilde{q}$ $(s = 0)$ squarks). The LHC will provide an answer whether supersymmetric particles exist within a mass range of 0.1–2 TeV/c^2.

Another question that will be addressed by the LHC is whether quarks and leptons are elementary particles as they are pictured today or if they are made up of sub-constituents. Finally, several new models propose the existence of extra dimensions that lead to a characteristic energy scale of quantum gravity in the TeV range.

1.3 Physics Requirements

Many of the new physics phenomena mentioned in the previous section have cross sections of 1 pb or less (1 barn (b) = 10^{-24} cm^2). Although the design luminosity at the LHC has purposely been chosen to overcome these small cross sections, these 'interesting' physics processes must still compete with the immense background coming from the inelastic proton-proton cross section of 80 mb. This presents a serious experimental difficulty since every new physics process will be accompanied by 23 inelastic events per bunch crossing on average [6].

The nature of proton-proton collisions imposes another experimental difficulty. The large number of particles expected to be produced are often grouped into sprays of particles called *jets*. Since jets often have a large boost, the particles in a jet are usually nearly collinear. A detector with fine granularity is therefore needed to distinguish particles within a jet. This granularity requirement becomes less important for the detector elements further away from the interaction point since the particle flux decreases as $1/R^2$.

Because the cross sections for QCD jet production dominate over the rare processes mentioned in the previous section, it is important to identify experimental signatures of the physics processes in question. These final state signatures, such as missing transverse energy ($\not{E}_T$) or secondary vertices, imposes even further demands on the particle-identification capabilities of the detector [6].

The benchmark physics goals discussed here have been converted into a set of general requirements for the LHC detectors [6]:

- "Due to the experimental conditions at the LHC, the detectors require fast, radiation-hard electronics and sensor elements. In addition, high detector granularity is needed to handle the particle fluxes and to reduce the influence of overlapping events.
- Large acceptance in pseudorapidity with almost full azimuthal angle coverage is required.
- Good charged-particle momentum resolution and reconstruction efficiency in the inner tracker are essential. For offline tagging of τ-leptons and b-jets, vertex detectors close to the interaction region are required to observe secondary vertices.
- Very good electromagnetic (EM) calorimetry for electron and photon identification and measurements, complemented by full-coverage hadronic calorimetry for accurate jet and missing transverse energy measurements, are important requirements, as these measurements form the basis of many of the studies mentioned above.
- Good muon identification and momentum resolution over a wide range of momenta and the ability to determine unambiguously the charge of high p_T muons are fundamental requirements.
- Highly efficient triggering on low transverse-momentum objects with sufficient background rejection, is a prerequisite to achieve an acceptable trigger rate for most physics processes of interest."

In the following sections, the ATLAS detector is described in the context of these physics requirements.

1.4 ATLAS Detector

ATLAS (A Toroidal LHC ApparatuS) is a 4π general-purpose detector designed for high-luminosity studies at the LHC. Construction and installation of the ATLAS detector at CERN are now complete [6]. The detector is situated at 'Point 1', the interaction point near the CERN Meyrin site.

The overall layout of the ATLAS detector is shown in Figure 1.2. Like most colliding beam experiments, it has approximate cylindrical symmetry. The detector is organized in a central *barrel* and two *end-caps* that close either end. In the barrel, the active detector elements form cylindrical layers around the beam pipe, while in the end-caps, they are organized in disks or wheels.

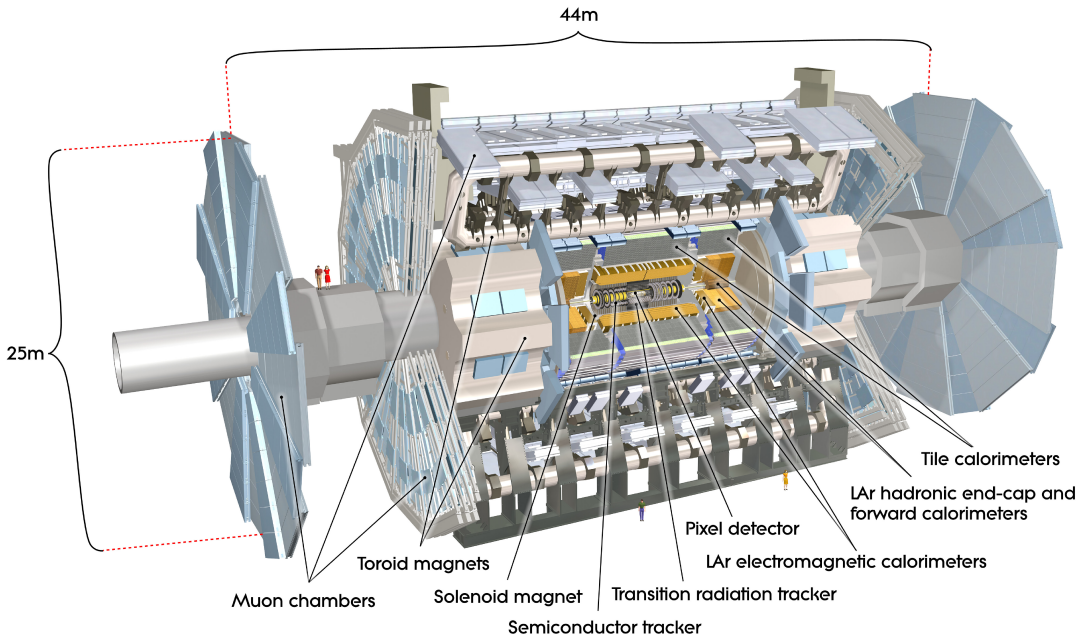

Figure 1.2: Cut-away view of the ATLAS detector. The dimensions of the detector are 25 m in height and 44 m in length. The overall weight of the detector is approximately 7000 tons. The various subsystems have been indicated. Taken from [6].

The origin of the ATLAS coordinate system is defined as the nominal interaction point. The beam direction defines the z-axis and the x-y plane (transverse to the beam direction). The positive

x-axis is defined as pointing from the interaction point to the center of the LHC ring and the positive y-axis is defined as pointing upwards. The 'A'-side ('C'-side) of the detector is defined as the side with positive (negative) z. ATLAS is nominally forward-backward symmetric with respect to the interaction point [6].

The cylindrical symmetry of the detector makes a cylindrical coordinate system useful. The azimuthal angle ϕ is measured as usual around the beam axis and the polar angle θ is the angle from the beam axis. The distance to the z-axis is called R. The pseudorapidity η is often used in hadron collider experiments instead of the polar angle θ. It is defined as

$$\eta = -\ln\left(\tan\frac{\theta}{2}\right). \tag{1.1}$$

The pseudorapidity is a convenient quantity because the particle multiplicity is approximately constant as a function of η. It will be used extensively in this dissertation. In the massless limit it is equal to the rapidity y, which can be written as

$$y = \frac{1}{2}\ln\left(\frac{E+p_z}{E-p_z}\right). \tag{1.2}$$

The transverse momentum p_T, the transverse energy E_T, and the missing transverse energy $\not{E}_T$ are defined in the x-y plane. The distance ΔR in the pseudorapidity-azimuthal angle space is equal to $\Delta R = \sqrt{\Delta\eta^2 + \Delta\phi^2}$.

The active detector elements in ATLAS can be divided into three sub-systems:

- The **Inner Detector** is the inner-most sub-system, responsible for detecting the tracks of charged particles. It is immersed in a 2 T solenoidal field for measuring track momentum.
- The **Calorimeters**, built around the Inner Detector, are responsible for measuring the energies of particles and jets. The calorimeters are specialized for measuring electromagnetic or hadronic particles.

- The **Muon Spectrometer** measures the momentum of muons, the only (known) charged particle that can penetrate through the calorimeters. The muon system also includes chambers for triggering on these particles.

The various subsystems of ATLAS are described in more detail in the following sections. Special focus is given to the Inner Detector since it is the most important detector for the measurements described in this thesis.

The magnet configuration in ATLAS consists of a thin superconducting solenoid surrounding the Inner Detector cavity and three large superconducting toroids (one barrel and two end-caps) arranged with an eight-fold azimuthal symmetry around the calorimeters. This fundamental choice has driven the design of most of the detector [6].

The main performance goals of ATLAS are listed in Table 1.2. Excellent momentum resolution at high momenta is possible in part because of the large tracking volume and long lever arm. The ATLAS calorimeters are thick in order to fully contain showers and minimize the amount of *punch-through*, or leakage of energy, into the muon chambers. Fast electronics are required in all sub-systems to keep up with the LHC bunch crossing rate.

Detector component	**Required resolution**	**η coverage**
Tracking	$\sigma_{p_T}/p_T = 0.05\% \cdot p_T \oplus 1\%$	± 2.5
EM Calorimetry	$\sigma_E/E = 10\%/\sqrt{E} \oplus 0.7\%$	± 3.2
Hadronic calorimetry (jets)		
barrel and end-cap	$\sigma_E/E = 50\%/\sqrt{E} \oplus 3\%$	± 3.2
forward	$\sigma_E/E = 100\%/\sqrt{E} \oplus 10\%$	$3.1 < \lvert\eta\rvert < 4.9$
Muon spectrometer	$\sigma_{p_T}/p_T = 10\%$ at $p_T = 1$ TeV/c	± 2.7

Table 1.2: General performance goals of the ATLAS detector. Note that for high-p_T muons, the performance of the Muon Spectrometer is independent of the Inner Detector. The units for E and p_T are GeV and GeV/c, respectively. The $\oplus$ symbol denotes addition in quadrature. Taken from [6].

1.5 Inner Detector

The Inner Detector (ID) [6,13] is the sub-detector of ATLAS closest to the interaction point. It is responsible for reconstructing the trajectories, or *tracks*, of charged particles that are produced in collisions at the LHC. Approximately 1000 particles are expected to be produced every 25 ns within the ID volume [6], creating a very large track density in the detector.

The charge, momentum and direction of each track are measured, as well as the impact parameter, defined as the distance of closest approach to the beamline. The ID is also responsible for reconstructing both primary and secondary vertices, which are needed to identify e.g. B-mesons and converted photons. The Inner Detector is immersed in a 2 T magnetic field generated by a central solenoid. By measuring the curvature of the tracks in the magnetic field, the momentum of the particles can be determined.

The layout of the Inner Detector is illustrated in Figure 1.3. The ID consists of three independent, but complementary, sub-detectors:

- a silicon pixel detector at inner radii with very high granularity, providing high-resolution pattern recognition with discrete 3-dimensional space-points;
- a silicon strip detector (SemiConducting Tracker, or SCT) surrounding the pixel detector, providing 3-dimensional space-points from stereo pairs of hits;
- a straw tracker (Transition Radiation Tracker, or TRT) at larger radii, comprised of many layers of gaseous straw tube elements interleaved with transition radiation material and providing a large number of measurements in the bending plane.

By combining precision trackers at small radii with the straw tracker at a larger radius, high-precision, robust pattern recognition can be obtained in both R-ϕ and z coordinates [6]. The silicon detectors allow precise measurements of the impact parameter as well as vertexing for heavy-flavor and τ-lepton tagging. The innermost layer of pixels, called the b-layer, at a radius of 5 cm, enhances the performance of secondary vertex measurements. The straw hits provide continuous tracking to

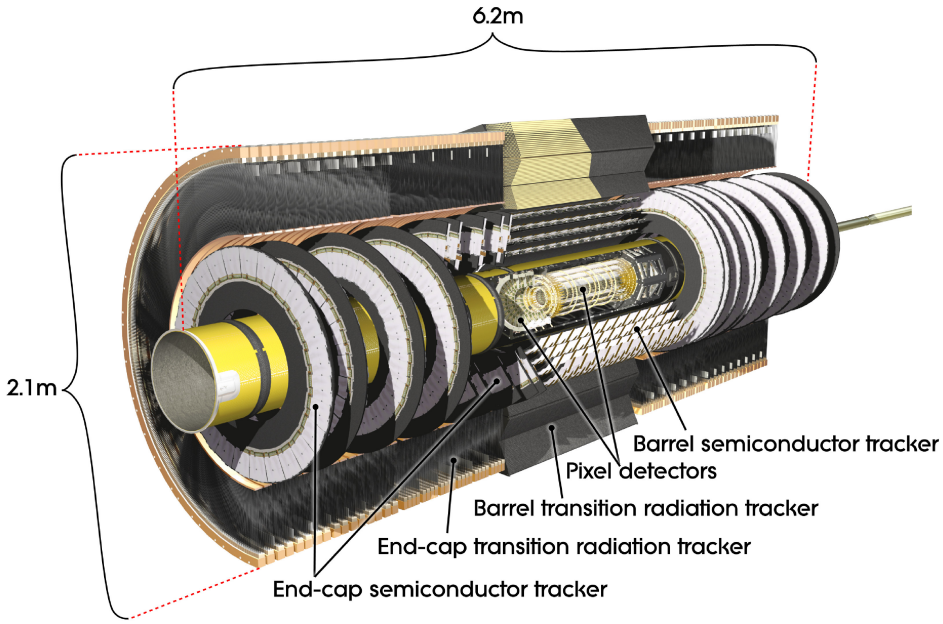

Figure 1.3: Cut-away view of the ATLAS Inner Detector. Taken from [6].

enhance the pattern recognition and significantly improve the momentum resolution due to the large number of measurements and the longer measured track length. The straw tracker also provides electron identification (complementary to that of the calorimeter) by detecting transition-radiation photons in the gas mixture of the straw tubes.

The Inner Detector covers the pseudorapidity region $|\eta| < 2.5$. The acceptance is made as large as possible to prevent particles from escaping undetected. Although the precision tracking detectors (pixels and SCT) cover the region $|\eta| < 2.5$, the TRT only covers the region $|\eta| < 2.0$ (omitting the outermost TRT wheels). The ID is contained within a cylindrical envelope of length ± 3512 mm and radius 1150 mm. The envelopes of each sub-detector are listed in Table 1.3. An R-z view of the ID is shown in Figure 1.4.

Figure 1.5 shows the sensors and structural elements traversed by tracks with $p_T = 10$ GeV/c in the barrel and end-cap regions. The various components of the Inner Detector are described in more detail in the following sub-sections.

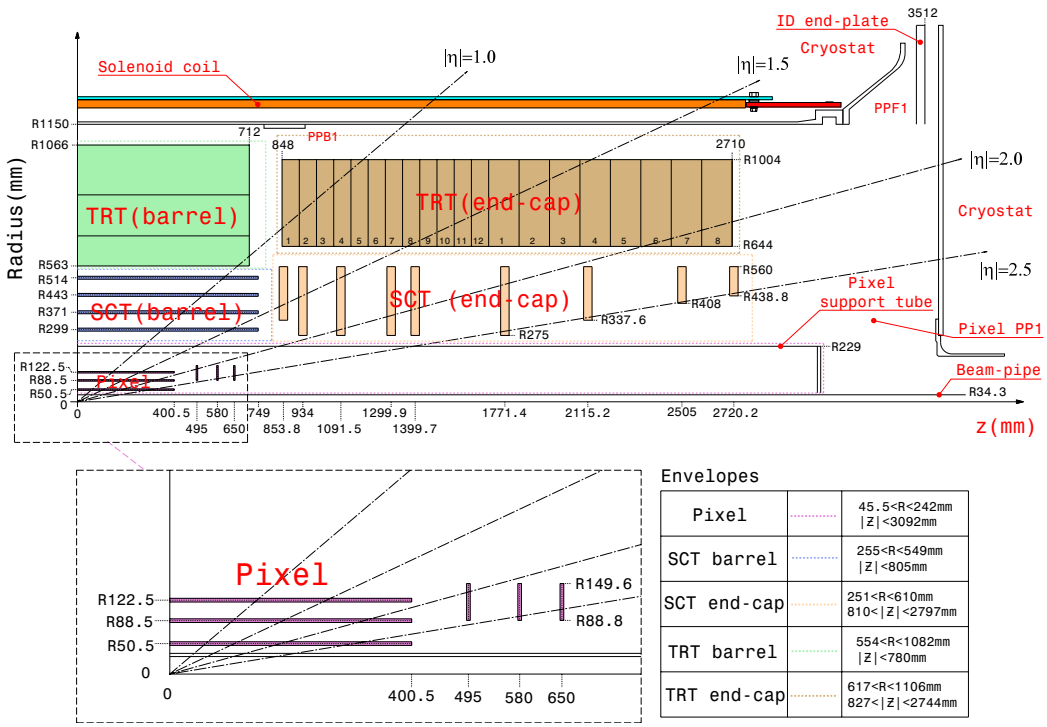

Figure 1.4: R-z view of a quarter-section of the ATLAS Inner Detector showing each of the major detector elements with its active dimensions and envelopes. The labels PP1, PPB1 and PPF1 indicate the patch-panels for the ID services. Taken from [6].

Item		**Radial extension (mm)**	**Length (mm)**
Overall ID envelope		$0 < R < 1150$	$0 < \|z\| < 3512$
Beam-pipe		$29 < R < 36$	
Pixel	Overall envelope	$45.5 < R < 242$	$0 < \|z\| < 3092$
3 cylindrical layers	Sensitive barrel	$50.5 < R < 122.5$	$0 < \|z\| < 400.5$
2×3 disks	Sensitive end-cap	$88.8 < R < 149.6$	$495 < \|z\| < 650$
SCT	Overall envelope	$255 < R < 549$ (barrel)	$0 < \|z\| < 805$
		$251 < R < 610$ (end-cap)	$810 < \|z\| < 2797$
4 cylindrical layers	Sensitive barrel	$299 < R < 514$	$0 < \|z\| < 749$
2×9 disks	Sensitive end-cap	$275 < R < 560$	$839 < \|z\| < 2735$
TRT	Overall envelope	$554 < R < 1082$ (barrel)	$0 < \|z\| < 780$
		$617 < R < 1106$ (end-cap)	$827 < \|z\| < 2744$
73 straw planes	Sensitive barrel	$563 < R < 1066$	$0 < \|z\| < 712$
160 straw planes	Sensitive end-cap	$644 < R < 1004$	$848 < \|z\| < 2710$

Table 1.3: Main parameters of the Inner Detector. Taken from [6].

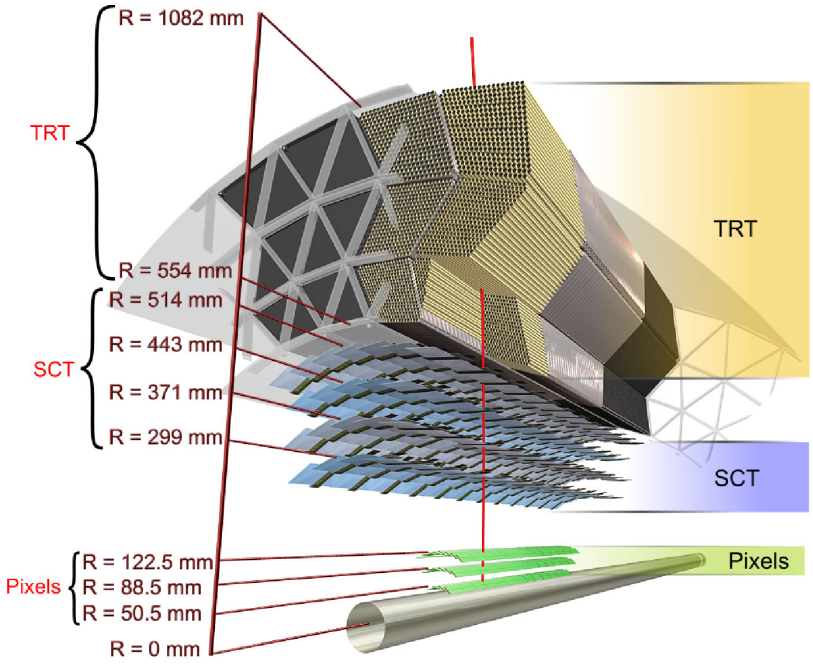

(a)

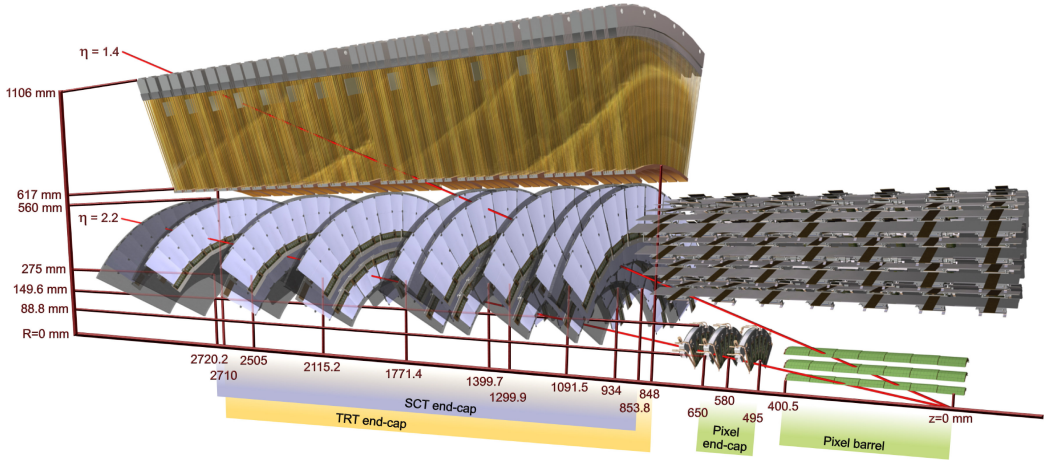

(b)

Figure 1.5: (a) Sensors and structural elements traversed by a charged track with $p_T = 10$ GeV/c in the Inner Detector barrel ($\eta = 0.3$). The track successively traverses the beam-pipe, the three barrel layers of the pixel detector, the four double layers of the barrel SCT and approximately 36 axial straws contained in the barrel TRT. Taken from [6]. (b) Sensors and structural elements traversed by two charged tracks with $p_T = 10$ GeV/c in the Inner Detector end-cap ($\eta = 1.4$ and $\eta = 2.2$). The end-cap track at $\eta = 1.4$ successively traverses the beam-pipe, the three barrel layers of the pixel detector, four of the double-layered SCT end-cap disks and approximately 40 straws contained in the TRT end-cap wheels. In contrast, the track at $\eta = 2.2$ traverses only the first of the barrel pixel layers, two end-cap pixel disks and the last four disks of the end-cap SCT. The coverage of the end-cap TRT does not extend beyond $|\eta| = 2$. Taken from [6].

1.5.1 Pixel detector

The silicon pixel detector [6, 13] is positioned closest to the beamline in ATLAS and provides the highest granularity around the vertex region. The active silicon sensors of the pixel detector are segmented into small rectangles in R-ϕ and z, called *pixels*. The pixel detector is extremely important for the pattern recognition in ATLAS. Its very high granularity and proximity to the interaction point dominate the impact parameter resolution and give it an excellent two-track resolution. This is further explained in Chapter 4.

In the barrel region, the detector elements are arranged on concentric cylinders around the beam axis, while in the forward (end-cap) regions, they are located on disks perpendicular to the beam axis. There are three layers in the barrel, at distances of 50.5, 88.5 and 122.5 mm from the beamline, and three disks in each of the forward regions. Three pixel layers are typically crossed by each track.

When a charged particle traverses the silicon sensor, free electron-hole pairs are produced in the silicon. The electrons are made to drift to the readout side of the sensor by applying a bias voltage across the sensor, creating an electric field. A discriminator in the readout electronics determines if the deposited charge is above threshold. The typical operating threshold is 4000 e^-. If the signal is above threshold, the hit pixel address, a hit time stamp and a digitized amplitude (the time over threshold, or ToT) are transferred to buffers at the periphery of the readout chip and then written out. The amount of deposited charge can be determined from the ToT.

A module of the pixel detector consists of a silicon sensor of area 63.4×24.4 mm^2 and thickness 250 μm, as well as 16 front-end electronics chips thinned to 180 μm thickness, with 2880 electronics channels each. The electronics channels are bump-bonded (In or PbSn) to the pixel sensor elements. The size of most pixels is 50×400 μm^2 (R-$\phi \times z$). About 10% of the pixels have size 50×600 μm^2 (called 'long' pixels). Because the readout chips do not cover the entire silicon surface, the pixels that lie between two chips share a readout channel with another pixel. These pixels are called *ganged*

pixels. If a particle hits such a pixel, then the reconstruction software must decide which pixel was actually hit (see Section 4.4.1).

There are 46,080 readout channels (47,268 pixels) per module and 1,744 modules in the pixel detector, giving a total of approximately 80.4 million readout channels. The intrinsic accuracies are 10 μm (R-ϕ) and 115 μm (z) in the barrel and 10 μm (R-ϕ) and 115 μm (R) in the disks [6]. These values are slightly better than the usual (pitch/$\sqrt{12}$) due to charge sharing between neighboring pixels, which is dependent on the incident angle. From commissioning studies and data with cosmic rays, 96% of all modules are operational, with a hit efficiency of 99.8% in the three barrel layers [14].

The active sensors and front-end electronics of the pixel detector require substantial power for operation. This includes bias voltage (HV) for the silicon sensors and low voltage (LV) for the front-end electronics. The power system for the pixel detector also includes remotely-programmable regulator stations, which protect the front-end electronics against transients. Testing of these electrical services is detailed in Appendix C.

1.5.2 SCT detector

The SemiConductor Tracker (SCT) [6,13] surrounds the pixel detector and gives one-dimensional position measurements using silicon sensors segmented in *strips*. A module in the SCT has two sensors that are glued back-to-back with a small relative angle (around 40 mrad). The stereo strips make it possible to measure both coordinates by finding the intersection of two strips in the sensor. The SCT contributes to the resolution of the impact parameter, the momentum, and the z-position of the vertex. Its high granularity also makes it important for the pattern recognition.

Like the pixel detector, the SCT modules are arranged on cylindrical layers in the barrel region and disks in the end-cap regions. There are four layers in the barrel and nine disk layers in each end-cap. One set of strips in each barrel layer is parallel to the beam direction, measuring R-ϕ. Two 64 mm long sensors with a strip pitch of 80 μm are daisy-chained, with the strips oriented on the long side of the rectangle. The circuit board with the readout chips (called a 'hybrid') is installed near

the middle of the sensor. The sensors are wedge-shaped in the end-cap region and the strips have a fan geometry to match the wedge shape of the sensor. One set of strips run radially and another set of stereo strips run at an angle of 40 mrad. The mean pitch of the strips is also approximately 80 μm. The length of the strips in the end-cap modules is either 6 or 12 cm, depending on the module type.

In both the barrel and the end-cap, the modules are mounted such that each track will encounter eight strip layers (four space points) on average. There are 768 strips per sensor, 2112 modules in the barrel and 988 modules in each of the two end-caps. The total number of readout channels in the SCT is approximately 6.3 million. Unlike the pixel modules, the readout of the SCT modules is binary. This limits the spatial resolution to about 23 μm per sensor. The intrinsic accuracies per module are 17 μm (R-ϕ) and 580 μm (z) in the barrel and 17 μm (R-ϕ) and 580 μm (R) in the disks.

The expected threshold setting during data taking is 1 fC (about 16,000 e^-) [15]. The threshold is calibrated for each channel by injecting charge using a calibration capacitor. The physical value of the threshold in fC and the noise level can be determined by measuring the number of hits. The noise level is required to be less than 5×10^{-4} for a tracking efficiency of at least 99% [15]. Commissioning tests have shown that these requirements are met [16].

1.5.3 TRT detector

The Transition Radiation Tracker (TRT) [6, 13] is the outermost sub-detector in the Inner Detector. It provides continuous tracking (or track-following) up to $|\eta| < 2.0$ using 4 mm diameter straw tubes with a gold-plated tungsten wire in the middle. The straws in the barrel region are 144 cm long and parallel to the beam axis, with their wires divided into two halves at approximately $\eta = 0$. The straws in the end-cap are 37 cm long and arranged radially in wheels.

The straws of the TRT are filled with a 70:27:3 Xe:CO_2:O_2 gas mixture that ionizes when a particle traverses it. The ionization clusters are collected by applying a large potential difference

between the wall of the straw and the wire. The distance of the particle to the wire can be determined by measuring the time it takes these clusters to reach the wire. This distance is called the *drift radius* and the resolution of this measurement is about 170 μm [15].

The xenon gas in the straws is also sensitive to transition radiation photons that are produced in the radiator material (polyethylene-polypropylene) between the straws. Because the number of transition radiation photons depends on the relativistic factor $\gamma = E/m$ of the particle, electrons produce many more photons than other particles. An electron identification efficiency of 99%, with a pion rejection factor of 100, can be achieved for energies greater than 1 GeV [15].

The 52,544 straws in the barrel are arranged in 73 cylindrical layers. All charged tracks with $p_T > 0.5$ GeV/c and $|\eta| < 2.0$ will traverse at least 36 straws (every other layer on average), except in the transition region between the barrel and end-caps ($0.8 < |\eta| < 1.0$) [6]. There are 18 wheels in each end-cap and 319,488 straws in total. The four outermost wheels in each end-cap will not be installed initially [15]. The total number of readout channels in the TRT is approximately 351,000.

The occupancy in the TRT is much higher than in the pixels and SCT due to the large straw size relative to a pixel or strip. At LHC design luminosity, some straws are expected to have an occupancy of up to 50% [15]. To reduce the occupancy, the wires in the barrel are electrically separated in the middle by a glass wire-joint. This results in two independent halves that are read out on either side of the straw. The wires in the first nine layers have two wire-joints, resulting in two active lengths of 36 cm on either side and a dead region in the middle.

The TRT can only provide R-ϕ information, with an intrinsic accuracy of 130 μm per straw. However, the TRT significantly improves the momentum resolution due to its long lever arm. For example, the momentum resolution for a muon with $p_T = 500$ GeV/c improves by roughly a factor of two when the TRT is included [15]. In addition, electron identification allows the possibility of applying an appropriate model in the track fit.

1.5.4 Solenoid magnet

The Inner Detector is immersed in a superconducting solenoid magnet that generates a field of about 2 T at a nominal current of 7.73 kA [6]. The magnet is 5.8 m long, with an inner diameter of 2.46 m and an outer diameter of 2.56 m. The single-layer coil is wound with a high-strength Al-stabilized NbTi conductor, specially developed for achieving a high field while optimizing thickness [6].

Figure 1.6 shows the R and z-dependence of the radial (Br) and axial (Bz) components of the magnetic field. At nominal current, the total measured field is 1.998 T at the interaction point, and drops steeply from about 1.8 T at $z = 1.7$ m to about 0.9 T at the end of the ID cavity [6]. The inhomogeneity of the magnetic field in the forward region requires the use of a field map in simulation and reconstruction.

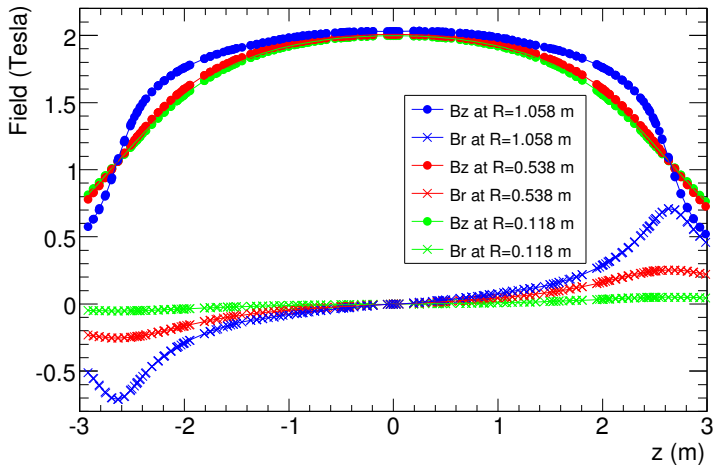

Figure 1.6: R and z-dependence of the radial (Br) and axial (Bz) magnetic field components in the Inner Detector cavity, at fixed azimuth. The symbols denote the measured axial and radial field components and the lines are the result of the fit described in [6]. Taken from [6].

The momentum resolution is directly related to the bending power of the magnet, which is given by the field integral $\int B \cdot \mathrm{d}l$. This quantity ranges from about 2 T·m at $|\eta| = 0$ to about 0.5 T·m at $|\eta| = 2.5$. This is because the field strength in the end-caps is lower than in the barrel

and because tracks in the very forward region ($|\eta| > 1.85$) exit the tracker longitudinally (along z) before reaching the solenoid. The latter reduces the length of the measured trajectory in the R-ϕ plane ('lever arm'), increasing the relative extrapolation distance to the beamline [15]. Thus, the resolution on the impact parameter is also worse in the forward region. The resolutions in the forward region are further worsened due to the extra material relative to the barrel region.

1.5.5 Material budget

The overall weight ($\sim$ 4.5 tons) and material budget of the Inner Detector are much larger than those of previous tracking detectors. Material includes active sensors, as well as inert material such as cables and cooling and support structures. Particles that traverse any of this material will interact with it. This can have severe consequences for the reconstruction. The most important ones are:

- multiple Coulomb scattering of charged particles, causing them to deviate from their ideal trajectory;
- hadronic interactions between hadrons and the detector material, producing a stream of secondary particles;
- bremsstrahlung of electrons, causing them to suffer from highly fluctuating energy losses; and
- conversion of photons into an electron-positron pair ($\gamma \rightarrow e^+e^-$).

Although the reconstruction can correct for these effects to a certain extent (see Chapter 4), these types of interactions always reduce the performance of the reconstruction. For this reason, the amount of material in the ID is kept to a minimum by using lightweight, low-Z materials (such as carbon fiber) for the support structures.

A detailed modeling of the material in the ID has been implemented in the simulation. Figure 1.7 shows the amount of material traversed by a straight track as a function of $|\eta|$ at the exit of the ID envelope. The material is expressed in terms of radiation lengths (X_0) and interaction lengths (λ).

The radiation length is the length over which the energy of an electron is, on average, reduced by a factor of e. The interaction length is the mean free path of a particle before undergoing an inelastic interaction.

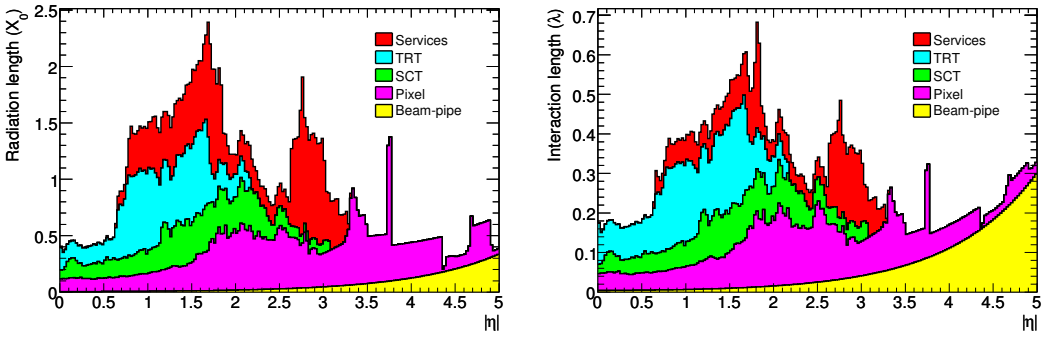

(a) (b)

Figure 1.7: Material distribution X_0 (a) and λ (b) at the exit of the ID envelope, including the services and thermal enclosures. The distribution is shown as a function of $|\eta|$ and averaged over ϕ. The breakdown indicates the contributions of external services and of individual sub-detectors, including services in their active volume. Taken from [6].

There is a huge contribution from non-active service and structural material at the interface of the barrel and end-cap regions ($|\eta| \approx 0.8$). This is due to cooling connections at the end of the SCT and TRT barrels, electrical connections for the TRT, and barrel services for the SCT and TRT [6]. Another large contribution comes from the pixel services at $|\eta| > 2.7$. A large fraction of the service and structural material is external to the active ID envelope, which deteriorates the calorimeter resolution but not the tracking performance [6].

1.6 Calorimeters

The calorimeters in ATLAS identify and measure the energy of charged and neutral particles, as well as jets. They also detect missing transverse energy ($\not{E}_T$) by summing all of the measured energy deposits. Missing energy can be a sign of interesting new physics, such as the production of supersymmetric particles.

Sampling calorimeters, such as the ones in ATLAS, have both a passive and active medium, made of distinct materials. The passive medium is usually a dense material, which acts as an absorber and produces a particle shower when an incoming particle hits it. Particles that are created in this shower are detected in the active medium. The passive and active medium are typically interleaved. The advantage of this strategy is that each material can be specialized for its task. A dense material can be used to produce a shower that evolves quickly in a limited space. The disadvantage is that some of the energy is deposited in passive material and not measured. The total energy in the shower must therefore be estimated.

Two types of active materials are used for the ATLAS calorimeters: liquid argon (LAr) and scintillating plastic. Particles that traverse the liquid argon create charge by ionization, which is collected on readout electrodes. The scintillating plastic is doped with fluorescent dye molecules, which emit light when the atoms in the plastic are excited by a passing particle. This light is detected and amplified by photomultiplier tubes. Several types of material are used for the passive absorbers, depending on space constraints and availability: lead, iron, copper and tungsten.

The layout of the calorimeters in ATLAS is shown in Figure 1.8. The entire calorimeter system covers the range $|\eta| < 4.9$. ATLAS has separate electromagnetic and hadronic calorimeters up to $|\eta| = 3.2$. Electromagnetic calorimeters are specifically designed to measure the energy of particles that interact primarily via the electromagnetic interaction, while hadronic calorimeters are designed to measure particles that interact via the strong nuclear force, including jets of particles formed by hadronization of quarks and gluons, as well as hadronically-decaying τ-leptons. A special combined electromagnetic and hadronic calorimeter extends the pseudorapidity coverage between $3.1 < |\eta| < 4.9$. The various calorimeter sub-systems are described in more detail in the following sub-sections.

Each calorimeter uses a different technique suited to particular requirements of the physics processes of interest and of the radiation environment over the large range in η. The fine granularity of the electromagnetic (EM) calorimeter is ideally suited for precision measurements of electrons

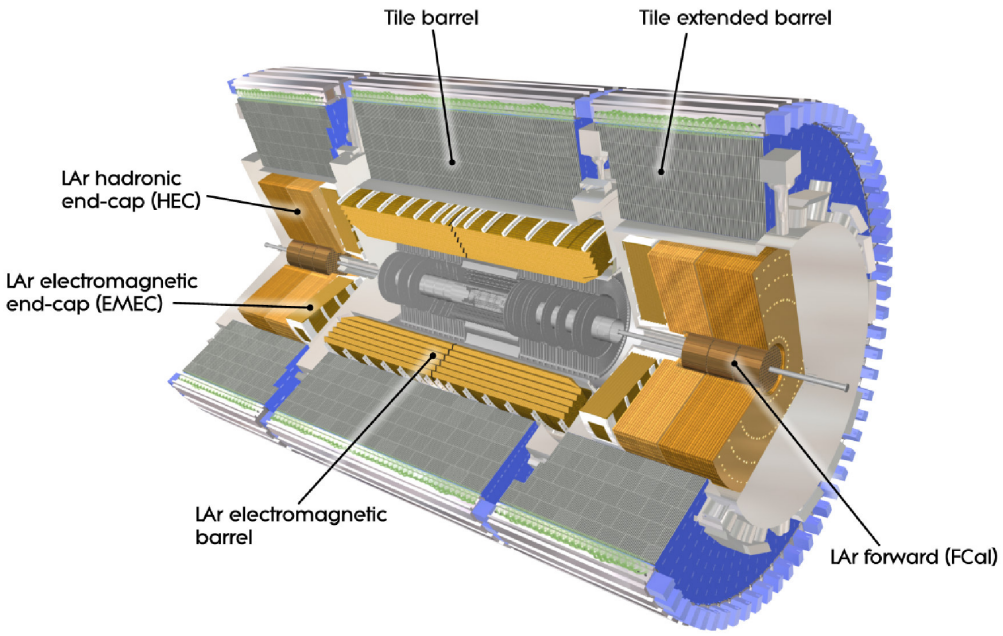

Figure 1.8: Cut-away view of the ATLAS calorimeter system. Taken from [6].

and photons, over an η region matched to the Inner Detector ($|\eta| < 3.2$) [6]. The EM calorimeter has excellent performance in terms of energy and position resolution. The coarser granularity of the rest of the calorimeter is sufficient to satisfy the physics requirements for jet reconstruction and $\not{E}_T$ measurements [6].

Depth is an important design criterion for calorimeters since they should contain particle showers well and limit punch-through into the muon system. The total thickness of the EM calorimeter is greater than 22 radiation lengths (X_0) in the barrel and greater than $24X_0$ in the end-caps. There are about 9.7 interaction lengths (λ) of active calorimeter in the barrel and 10λ in the end-caps. The total thickness, including 1.3λ from the outer support, is 11λ at $\eta = 0$. Both measurements and simulations have shown that this is sufficient for reducing punch-through well below the irreducible level of prompt or decay muons [6].

1.6.1 Electromagnetic calorimeter

The electromagnetic (EM) calorimeter [6,17] is divided into a barrel part ($|\eta| < 1.475$) and two end-cap components ($1.375 < |\eta| < 3.2$), each housed in its own cryostat. The barrel calorimeter consists of two identical half-barrels, separated by a small gap of 4 mm at $z = 0$. Each end-cap calorimeter is mechanically divided into two coaxial wheels: an outer wheel covering the region $1.375 < |\eta| < 2.5$ and an inner wheel covering the region $2.5 < |\eta| < 3.2$.

The EM calorimeter uses liquid argon (LAr) as the active medium with accordion-shaped kapton electrodes and lead absorber plates as the passive medium. The accordion geometry provides complete ϕ symmetry without azimuthal cracks, which would degrade the energy resolution. The thickness of the lead in the absorber plates has been optimized for energy resolution as a function of η [6]. The readout electrodes, made of copper and kapton, are installed between the lead plates. The electrodes are separated from the lead by plastic meshes and the remaining space is filled with liquid argon.

The EM calorimeter is divided into three longitudinal compartments, or *samplings*, over the region $|\eta| < 2.5$. The innermost compartment is finely segmented in η, which makes a good separation of γ/π^0 and e/π possible. Electrons and photons lose most of their energy in the middle compartment. The last compartment completes the energy measurement for showers that extend past the middle compartment, distinguishing between electromagnetic and hadronic showers. For the end-cap inner wheel, the calorimeter is segmented in two sections in depth and has a coarser lateral granularity than for the rest of the acceptance [6].

1.6.2 Hadronic calorimeters

The hadronic calorimeters [6, 18] use two different technologies: scintillator-tile in the barrel region $|\eta| < 1.7$ and liquid argon in the end-caps $|\eta| > 1.5$. Since hadronic showers are much longer and wider than electromagnetic showers, the hadronic calorimeter needs to be much thicker than the EM calorimeter. The total thickness of the calorimeters is more than 10λ.

The barrel part, called the **Tile Calorimeter**, is placed directly outside the EM calorimeter envelope and is separated into a large central barrel ($|\eta| < 1.0$) and two smaller extended barrel cylinders ($0.8 < |\eta| < 1.7$) on either side. The barrel and extended barrels are divided azimuthally into 64 modules. The Tile Calorimeter uses steel plates as the absorber and scintillating tiles as the active material. The tiles are placed radially, staggered in depth, and cells are formed by grouping tiles together. The tiles are read out into two separate photomultiplier tubes by wavelength-shifting optical fibers. The total number of readout channels is about 10,000. The total detector thickness at the outer edge of the tile-instrumented region is 9.7λ at $\eta = 0$ [6].

The end-cap part, called the **Hadronic End-cap Calorimeter (HEC)**, is located directly behind the end-cap electromagnetic calorimeter and consists of two independent wheels per end-cap. The HEC extends from $1.5 < |\eta| < 3.2$, thereby overlapping with the Forward Calorimeter and the Tile Calorimeter. Each wheel is made up of 32 identical wedge-shaped modules. The HEC uses liquid argon as the active medium because of its higher radiation tolerance and copper plates as the absorber material, arranged in a parallel-plate geometry. The copper plates are interleaved with 8.5 mm LAr gaps and three parallel electrodes, thus dividing the gap into four 1.8 mm drift spaces.

1.6.3 Forward calorimeter

The Forward Calorimeter (FCal) [6,17] covers the region $3.1 < |\eta| < 4.9$ and is about 10λ deep. It is split longitudinally into an electromagnetic compartment made of copper and two hadronic compartments made of tungsten. Each compartment has a metal matrix with regularly spaced channels that hold the tube and rod-shaped electrode structures parallel to the beam axis. The space between the tubes and rods is filled with liquid argon. The FCal is integrated into the end-cap cryostats, which provides a more uniform coverage and reduces the radiation background levels in the Muon Spectrometer [6].

1.7 Muon Spectrometer

The Muon Spectrometer (MS) [6,19] is the largest sub-detector, defining the overall dimensions of ATLAS. Since high-p_T muons are a signature of interesting physics, muon trigger and reconstruction are a very important part of the overall physics performance goals of ATLAS. The muon system is designed to achieve a momentum resolution of 10% for muons with $p_T = 1$ TeV/c. This amounts to measuring the sagitta of the muon with a precision of 50 μm or better [15].

The conceptual layout of the MS is shown in Figure 1.9. The muon system is instrumented with separate trigger and high-precision tracking chambers and a superconducting magnet system, which are all completely independent from the Inner Detector. The magnetic field is provided by a large barrel toroid over the range $|\eta| < 1.4$ and by two smaller end-cap toroids inserted into both ends of the barrel toroid for the range $1.6 < |\eta| < 2.7$. In the transition region ($1.4 < |\eta| < 1.6$), a combination of barrel and end-cap fields is used to bend the muon tracks. The magnetic field generated by this configuration is mostly orthogonal to the muon trajectories. The toroids have air-filled cores, minimizing multiple scattering that would degrade the momentum resolution [6].

The air-core system has an average field strength of 0.5 T. The barrel toroid provides 1.5 to 5.5 T·m of bending power in the range $|\eta| < 1.4$, while the end-cap toroids provide 1 to 7.5 T·m in the region $1.6 < |\eta| < 2.7$. The bending power is lower in the transition regions where the two magnets overlap ($1.4 < |\eta| < 1.6$) [6].

Excellent momentum resolution for muons is achieved with three layers of high-precision tracking chambers. In the barrel region, the chambers are arranged in cylindrical layers around the beam axis. In the transition and end-cap regions, the chambers are installed in planes perpendicular to the beam. The muon instrumentation also includes trigger chambers with timing resolution of the order of 1.5 to 4 ns. Four types of detection chambers are used in the MS: Monitored Drift Tube chambers (MDTs), Cathode Strip Chambers (CSCs), Resistive Plate Chambers (RPCs), and Thin Gap Chambers (TGCs).

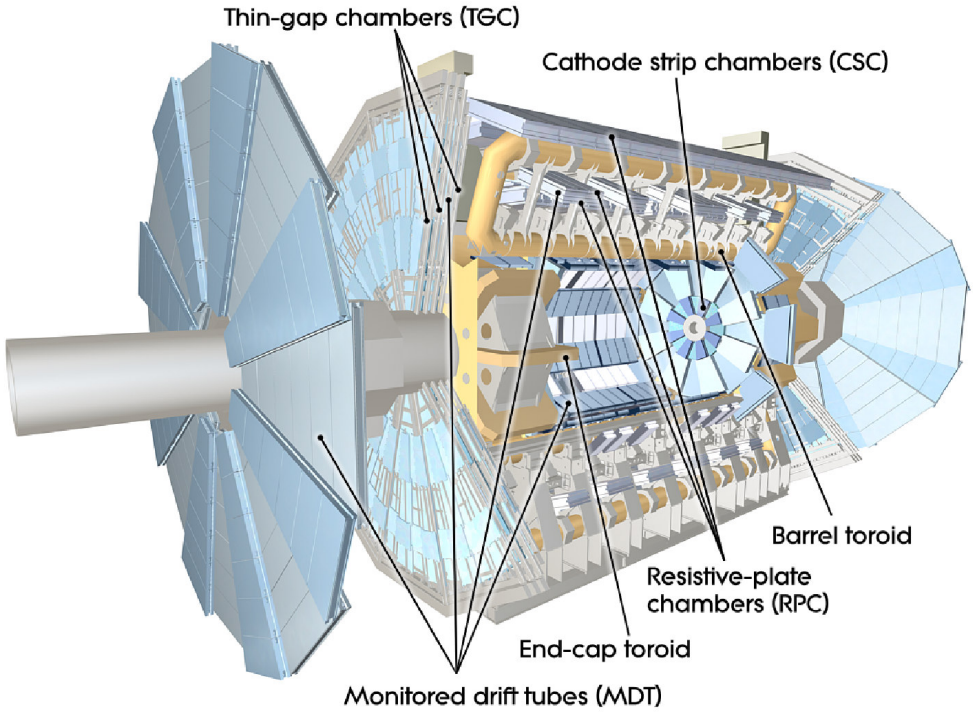

Figure 1.9: Cut-away view of the ATLAS muon system. Taken from [6].

The MDT chambers provide precise muon tracking in the principal bending direction of the magnetic field over most of the η range. The tubes are made of aluminum and have a diameter of 30 mm. The resolution on the drift distance is around 80 μm [15]. At large pseudorapidity ($2 < |\eta| < 2.7$), CSCs are used instead of MDT chambers due to the demanding rate and background conditions [6]. The CSCs are multi-wire proportional chambers with cathodes segmented into strips. The spatial resolution on the precision coordinate is around 60 μm [15].

The trigger system covers the range $|\eta| < 2.4$. Resistive Plate Chambers (RPCs) are used in the barrel and Thin Gap Chambers (TGCs) in the end-cap regions. These chambers measure the muon coordinate in the direction orthogonal to the one measured by the tracking chambers. They also provide bunch-crossing identification and well-defined p_T thresholds [6]. Resistive Plate Chambers (RPCs) are used in the barrel and Thin Gap Chambers (TGCs) in the end-cap regions.

1.8 Trigger System

The ATLAS trigger system [6, 20] is designed to select events with interesting physics from the initial bunch crossing rate of 40 MHz. It is based on three levels of event selection and must provide sufficient rejection to reduce the rate to 200 Hz, compatible with offline computing power and storage capacity limitations. Each trigger level refines the decisions made at the previous level and applies additional selection criteria if necessary.

The Level-1 (L1) trigger system [21] uses a subset of the total detector information to make a decision on whether or not to continue processing an event. It reduces the data rate to approximately 75 kHz, a limitation of the bandwidth in the readout system. The subsequent two levels, collectively known as the High-Level Trigger (HLT) [22], are the Level-2 (L2) trigger and the Event Filter (EF). They provide the reduction to a final data-taking rate of approximately 200 Hz.

The L1 trigger is hardware-based and uses a limited amount of the total detector information to make a decision in less than 2.5 μs. The L1 trigger searches for high-p_T muons, electrons, photons, jets, and τ-leptons decaying into hadrons, as well as large $\not{E}_T$ and total E_T. Its selection is based on data from the calorimeters (with reduced granularity) and from the muon trigger chambers. In the case of the muon trigger, a coarse estimate of the momentum is obtained from the RPC and TGC hits and the trigger is fired if the muon has a sufficiently high p_T. The calorimeter trigger is based on the total measured energy and the missing transverse energy in the event [6].

Muon and calorimeter L1 triggers are processed by a central trigger processor, which implements a trigger *menu* made up of combinations of trigger selections. To optimize use of the bandwidth as the luminosity and background conditions change, certain trigger menu items are 'pre-scaled' by the central trigger processor. Events that pass the L1 trigger selection are then transferred to the next stage of electronics and data acquisition. The L1 trigger also defines one or more Regions-of-Interest (RoIs) for each event. The RoIs are the geographical coordinates in η and ϕ of those regions in the detector which the trigger used for its selection process. The RoI data also include information on the

type of feature identified and the criteria passed, e.g. a threshold. This information is subsequently used by the high-level trigger [6].

The L2 trigger is software-based and is seeded by the RoI information provided by the L1 trigger. At full granularity and precision, selections in the L2 trigger use data from all subsystems within the RoI. The L2 menus are designed to reduce the trigger rate to approximately 3.5 kHz, with an event processing time of about 40 ms, averaged over all events [6].

The final stage of the event selection is carried out by the Event Filter (EF), which reduces the event rate to roughly 200 Hz. The EF has access to the whole event, with full granularity. Selections in the EF use offline analysis procedures, such as detailed reconstruction algorithms. The average event processing time in the EF is about four seconds. The EF runs on a dedicated computer farm near ATLAS. The events that pass the EF are written to mass storage and are available for further analysis with the ATLAS offline software.

A discussion of the trigger used for this analysis is deferred to Chapter 3.

Chapter 2

Minimum Bias at the LHC

Inelastic interactions have previously been studied over a wide range of energies. In particular, results from experiments at CERN and Fermilab have been used to tune current Monte Carlo event generators. However, due to uncertainties in the modeling of the energy dependence of soft interactions, these generators give widely varying predictions when extrapolated to LHC energies [23].

In this chapter, some theoretical background pertinent to the measurement is given. Two event generators commonly used to simulate inelastic events are described. Current uncertainties in the modeling of soft pp inelastic interactions at the LHC energy scale are discussed. Important observables are defined and the event generators are used to make LHC predictions.

2.1 QCD and the Parton Model

Quantum Chromodynamics (QCD) [24–26] is a gauge field theory that describes the interactions of colored quarks and gluons. At short distances, or equivalently high-energies, the effective coupling is small and perturbative techniques can be used to make calculations or predictions from the theory. Perturbative QCD provides an excellent description of data from a wide range of high-energy collider processes.

In the parton model, a hadron (e.g. a proton) is composed of a number of point-like constituents, called *partons*. Partons have been matched to quarks and gluons after a series of experimental and theoretical successes, including the observation of Bjorken scaling [27]. The parton model remains a justifiable approximation at high energies.

Essentially all physics processes at the LHC will arise from interactions between quarks and gluons [23]. The high-energy proton collisions at the LHC can therefore be described in terms of parton interactions [28, 29]. QCD has been successful in describing *hard* interactions, involving large transverse momenta with respect to the collision axis (p_T) [24–26]. These interactions happen at small distances with large momentum transfers that can produce massive particles.

Problems arise, however, when using QCD to describe *soft* partonic interactions, known as 'minimum bias' events. These interactions are in fact, the dominant processes in collisions at hadron colliders such as the LHC. These interactions appear at large distances between incoming protons in such a way that the protons interact as a whole with small momentum transfer. This means that particles in the final state have small transverse momentum ($p_T \sim 0.5$ GeV/c) and continue traveling along the direction of the beam.

Two effects contribute to the breakdown of QCD for soft interactions. The first is that at low energies, perturbative expansions in α_s are no longer practical since the strong coupling constant α_s approaches unity and the higher-order terms cannot be ignored. The second is that at a momentum transfer of about a few GeV/c, the QCD cross section σ_{QCD} for a $2 \rightarrow 2$ parton scattering exceeds the pp cross section [23]. This problem is solved by introducing the concept of *Multiple Partonic Interactions* (MPI). Since each of the incoming hadrons can be viewed as a beam of partons, it is possible to have several parton-parton interactions when the hadrons collide. Multiple parton scatterings have been observed in hadron collisions by experiments such as AFS [30] and UA2 [31] and directly measured by the CDF Collaboration [32–34].

2.2 Monte Carlo Event Generators

Although soft partonic processes are not well-described by QCD, they can be reasonably described by appropriately-tuned models in Monte Carlo (MC) event generators. Current models of high-energy hadron collisions typically combine perturbative QCD to describe high-p_T scatterings with an alternative phenomenological approach to describe soft processes [23]. Examples of these are the PYTHIA and PHOJET MC event generators. PYTHIA uses a modified version of QCD in which divergences are phenomenologically corrected to reproduce experimental observations [35], while PHOJET uses the Dual Parton Model (DPM) [36–39].

PYTHIA and PHOJET are discussed in more detail in the following sub-sections. Focus is given on their treatment and modeling of soft interactions in hadron-hadron collisions.

2.2.1 PYTHIA

PYTHIA [40–42] is a general-purpose MC event generator for hadronic events in pp, e^+e^-, and ep colliders. It has been developed mainly for high-p_T physics and contains a sub-process library covering QCD, the Standard Model, SUSY and other more 'exotic' physics areas. The PYTHIA framework also contains generation machinery for initial and final-state parton showers, underlying event, and hadronization and decays. Major changes related to the description of minimum bias interactions have been introduced in the latest releases [40–44].

In PYTHIA, the total rate of parton interactions is assumed to be given by perturbative QCD [23]. For reasonably large values of p_T ($p_T \geq 2$ GeV/c), it uses standard perturbative QCD to describe the parton scatterings. For soft interactions, it attempts to extend the perturbative high-p_T picture of parton interactions down to the low-p_T region by introducing a cut-off parameter $p_{T_{\min}}$ in order to correct divergences as $p_T \to 0$. $p_{T_{\min}}$is the minimum transverse momentum of the parton-parton collisions. It effectively controls the average number of parton-parton interactions, hence the average particle multiplicity. The interaction cross section is written as [23]

$$\sigma_{\rm int}(p_{T_{\rm min}}) \quad = \quad \int_{p_{T_{\rm min}}^2}^{s/4} \frac{{\rm d}\sigma}{{\rm d}p_T^2} {\rm d}p_T^2, \tag{2.1}$$

where $\frac{{\rm d}\sigma}{{\rm d}p_T^2}$ is the differential cross-section describing a $2 \rightarrow 2$ parton scattering. In the MPI picture, events with interaction cross sections greater than the total cross section are interpreted as having more than one parton-parton interaction taking place in the event [23].

There are two strategies in PYTHIA for introducing the $p_{T_{\rm min}}$ cut-off parameter into the model: a hard cut-off and a smooth turn-off. In the 'cut-off' scenario, the differential cross section drops to 0 for $p_T < p_{T_{\rm min}}$. In the 'turn-off' scenario, an impact-parameter-dependent[1] approach is introduced [35]. A small impact parameter ($p_T \gg p_{T_{\rm min}}$) corresponds to a large overlap between the two colliding hadrons, and hence an enhanced probability of multiple interactions. A large impact parameter ($p_T < p_{T_{\rm min}}$) means a high probability that no parton-parton interaction will take place in the event [23]. The PYTHIA tune used by ATLAS uses a model with a continuous turn-off of the cross section at $p_{T_{\rm min}}$, as well as hadronic matter in the colliding hadrons described by two concentric Gaussian distributions [42]. More details on the 'ATLAS' PYTHIA tune can be found in [23].

A sophisticated treatment of color, flavor and momentum correlations inside PYTHIA ensures conservation between all scatterings in an event and the partons of each incoming hadron. After the parton interaction cross sections are estimated by the model, the resulting partons are fragmented into colorless hadrons [23].

2.2.2 PHOJET

PHOJET [45,46] has been developed to model minimum bias events with a realistic superposition of the various diffractive and non-diffractive particle production processes (see Section 2.3). It can be used to simulate hadronic multi-particle production at high energies for hadron-hadron, photon-hadron, and photon-photon interactions.

[1]The impact parameter b is defined as the distance of closest approach that would result for two particles in a collision if the particle trajectories were undeflected by the collision.

PHOJET is formulated as a two-component model. It combines ideas of the Dual Parton Model (DPM) [36–39] to describe the dominant soft processes, with perturbative QCD [24–26] to generate hard interactions [45, 46]. The soft and hard components are combined by calculating scattering amplitudes while preserving unitarity [45]. A p_T cut-off similar to the one used in PYTHIA is used to separate the soft and hard processes.

The DPM describes soft processes by combining non-perturbative topological expansions of QCD with principles such as duality, unitarity, Regge behavior and the parton model [23]. In the DPM, the leading contribution to multi-particle production in hadron-hadron collisions comes from a single Pomeron exchange between the colliding hadrons. Double Pomeron exchanges account for the remaining activity in the event [23]. Multiple Pomeron exchange is included as an additional component to preserve unitarity.

Parameters of the model include couplings, Pomeron intercepts and slope parameters. These parameters are determined by comparing cross section predictions with available data. The fragmentation of soft-chains or hard-scattered partons is done using the same model found in PYTHIA.

2.2.3 Tuning

The PYTHIA and PHOJET event generators have been tuned to agree with previous studies of inelastic interactions over a wide range of different energies. These include measurements from the CERN ISR [47] and Sp$\bar{\text{p}}$S [48–50], as well as the Tevatron at Fermilab [51–54]. By modeling the energy dependence of these results, the event generators are able to make predictions at LHC energies [23]. However, due to large uncertainties in this extrapolation, the generators give widely varying predictions at LHC energies.

The analysis presented in this dissertation is based on events generated with PYTHIA version 6.420, configured with the `mc09` 'ATLAS' tune parameter set as defined in [55]. Events generated with PHOJET version 1.12.35 will be used as a reference to evaluate uncertainties on particular quantities throughout this chapter.

2.3 Total Cross Section

The total proton-proton cross section (σ_{tot}) at the LHC can be written as a sum of elastic (σ_{elas}) and inelastic (σ_{inel}) components. The inelastic portion can be further divided into non-diffractive (σ_{nd}), single-diffractive (σ_{sd}) and double-diffractive (σ_{dd}) components [56]. The total cross section can thus be written as a function of the center-of-mass-energy $\sqrt{s}$ as [23]

$$\sigma_{\text{tot}}(\sqrt{s}) \quad = \quad \sigma_{\text{elas}}(\sqrt{s}) + \sigma_{\text{nd}}(\sqrt{s}) + \sigma_{\text{sd}}(\sqrt{s}) + \sigma_{\text{dd}}(\sqrt{s}). \tag{2.2}$$

Central diffraction is not included here since it is only simulated by PHOJET and not by PYTHIA. Since it contributes only about 1% to the total cross section, it is not considered further in this analysis [3].

2.3.1 Components

Figure 2.1 shows a schematic view of elastic, single-diffractive, and double-diffractive inelastic hadron interactions in the η-ϕ phase space. The angle ϕ is the azimuthal scattering direction and η is the pseudorapidity as defined in Equation 1.1. In elastic scattering, the incoming protons interact very weakly by exchanging a color singlet [57]. Neither of the protons break apart and they continue traveling in their original respective directions. As shown in Figure 2.1, the proton separation in pseudorapidity is maximum for elastic scattering.

In single and double diffraction, one or both of the protons are excited into a high mass color singlet state which then decays [57]. This creates a spray of particles at high pseudorapidity. Single and double diffraction also correspond to color singlet exchange between the protons. The outgoing remnants are therefore no longer color singlets, causing quark-antiquark pairs to be pulled out of the vacuum [57]. As shown in Figure 2.1, single and double diffractive events display *rapidity gaps*, or clear separations in pseudorapidity between the systems traveling in the forward and backward directions.

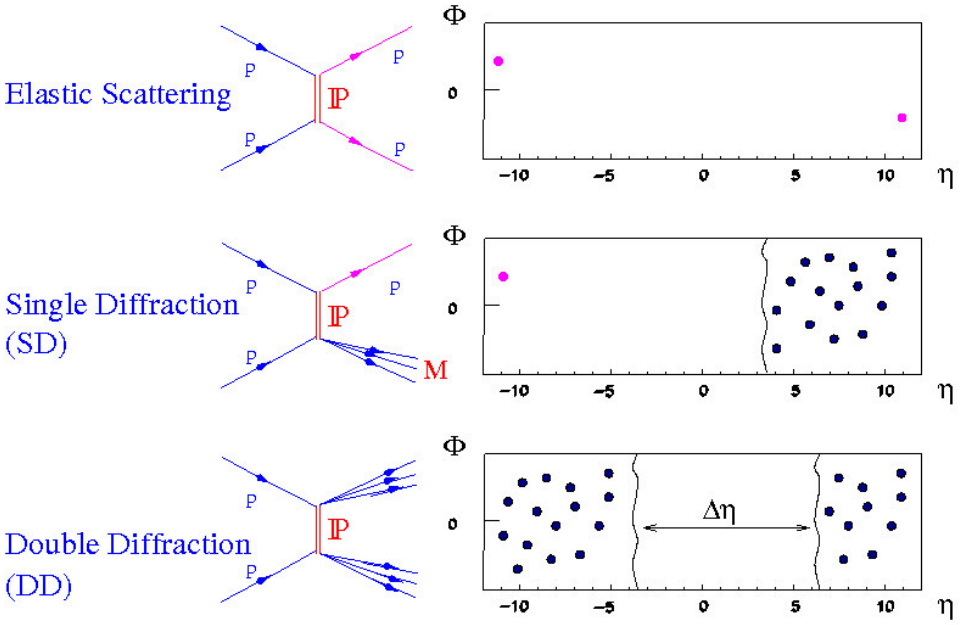

Figure 2.1: Schematic view of elastic, single-diffractive and double-diffractive processes in the η-ϕ phase space, along with their corresponding Feynman diagrams. Taken from [58].

The majority of the total cross section comes from the non-diffractive component. In these events, the protons collide head-on. Since the quarks approach each other very closely, the interaction proceeds predominantly by the exchange of a single gluon between two passing quarks; all others act as spectators. The non-diffractive component involves color exchange between partons and the separation of color, with both soft and hard components [57]. Most of the time, the color exchange occurs through a soft interaction, creating an abundance of soft particles in the central region with a uniform distribution in rapidity, as well as many particles flying down the beam pipe. Occasionally there is a hard scattering among the constituent partons producing outgoing particles and jets with high transverse momentum [57]. The particles in the central region have on average higher transverse momentum than in the diffractive scenarios.

2.3.2 LHC predictions

PYTHIA generates the total *pp* cross section using a parameterization derived from the Pomeron exchange model [59]. The optical theorem relation [60]

$$\sigma_{\text{elas}} = \frac{\sigma_{\text{tot}}^2}{16\pi B_{\text{elas}}} \tag{2.3}$$

is then used to calculate the elastic cross section, where B_{elas} is the elastic slope parameter, a measure of the transverse size of the scattering objects [45]. The total *pp* cross section predicted by PYTHIA at $\sqrt{s} = 14$ TeV is 102 mb, of which 22 mb come from the elastic contribution and 79 mb from the inelastic contribution. The contributions from single and double-diffractive scattering are estimated to be 14 and 10 mb, respectively. The non-single diffractive cross section, given by $\sigma_{\text{nsd}} = \sigma_{\text{inel}} - \sigma_{\text{sd}}$, is about 65 mb.

In PHOJET, the differential elastic cross section is first written as a function of the scattering amplitude. The total *pp* cross section is then estimated using the optical theorem relation from Equation 2.3. The total *pp* cross section predicted by PHOJET at $\sqrt{s} = 14$ TeV is 119 mb, split into elastic (34 mb) and inelastic (85 mb) parts. A different parameterization for the elastic slope B_{elas} is used in PHOJET [23]. The resulting total *pp* cross section is proportional to $\ln^2 s$ [61] and does not violate the Froissart-Martin bound which postulates that $\sigma_{\text{tot}} < A \ln^2 s$, where the constant $A = \pi\hbar^2 c^4/m_\pi^2$ is about 62 mb [62].

A summary of the predicted cross sections from PYTHIA and PHOJET at two LHC energies ($\sqrt{s} = 10$ TeV and 14 TeV) is given in Table 2.1. Although there is good agreement between the predicted cross sections and the experimental data for energies below 1 TeV, the predictions begin to diverge at roughly the same energy [23]. The total cross section predictions for PYTHIA and PHOJET give a 17% difference. Recent theoretical studies predict $\sigma_{\text{tot}} = 106.3 \pm 5.1_{\text{syst.}} \pm 2.4_{\text{stat.}}$ mb for *pp* collisions at the LHC [63].

The elastic cross sections also present a considerable divergence at LHC energies [23]. This is because the difference in σ_{tot} is squared to obtain σ_{elas} (see Equation 2.3). At $\sqrt{s} = 14$ TeV, PYTHIA

predicts $\sigma_{\text{elas}} = 22$ mb while PHOJET estimates $\sigma_{\text{elas}} = 34$ mb, a 55% difference. The discrepancy is less pronounced for σ_{inel}.

Physics process	**Cross section (mb)**			
	$\sqrt{s} = 10$ TeV		$\sqrt{s} = 14$ TeV	
	PHOJET	PYTHIA	PHOJET	PYTHIA
Non-diffractive	64.9	51.6	68.0	54.7
Single diffractive.	10.9	14.0	11.0	14.3
Double diffractive	4.0	9.8	4.1	10.3
Central diffractive	1.4	–	1.4	–
Elastic	31.9	20.8	34.4	22.2
Inelastic	81.2	75.4	84.5	79.3
Total	113.1	96.2	118.9	101.5

Table 2.1: Cross section predictions for pp collisions at $\sqrt{s} = 10$ TeV and 14 TeV from PYTHIA and PHOJET. In both event generators, the inelastic cross section is obtained by subtracting the elastic from the total cross section.

2.4 Minimum Bias

The trigger used to accept inelastic events is usually known as a *minimum bias* trigger. Although it is designed to avoid bias in the sample, some bias is usually introduced due to minimum energy thresholds or limited geometrical acceptance of the trigger [3]. The term 'minimum bias', therefore, is experimentally defined. It generically refers to events selected with a loose trigger that accepts a large fraction of the inelastic cross section. However, slightly different definitions are made by each experiment.

Minimum bias events are usually associated with the non-single-diffractive (NSD) inelastic portion of the total cross section (see Equation 2.2): $\sigma_{\text{nsd}} = \sigma_{\text{tot}} - \sigma_{\text{elas}} - \sigma_{\text{sd}}$. This is mostly for historical reasons, since the trigger used to select inelastic events in previous hadron collider experiments typically required a forward-backward coincidence, thus suppressing single-diffractive interactions. Elastic scattering was not included since the trigger only accepted events with activity in the central

region. The NSD definition has been used at the ISR [47] and UA5 [48–50] and more recently at CDF [51, 52] and E735 [53, 54].

Although minimum bias is often defined experimentally as non-single diffractive events, some theoretical groups have chosen to identify minimum bias with non-diffractive inelastic interactions [56]. However, it is experimentally difficult to separate double-diffractive from non-diffractive events. On a practical note, the experimentally preferred choice for NSD inelastic interactions does not differ considerably from the theoretical non-diffractive preference, since their cross sections would hardly differ by more than about 15% at current collider energies [23].

The definition of minimum bias used in this dissertation is deferred to Chapter 3, following a discussion of the minimum bias triggers in ATLAS.

2.5 Minimum Bias Observables

Minimum bias data have been collected in the energy range $\sqrt{s} = 200$ GeV to 1.8 TeV [47–54]. Measurements typically focus on charged particle data, corrected for contributions from π^0, K_S and Λ decays. Other measurements include energy flow of charged and neutral particles and forward-backward correlations. These measurements give information about the production and decay of hadrons. They also allow Monte Carlo models to be tested and constrained, especially their energy dependence. Finally, these studies provide a baseline for heavy-ion collisions, since QCD effects need to be disentangled from effects due to scaling of the number of nucleons.

Minimum bias events are dominated by soft interactions, with low transverse momentum and low particle multiplicity. The simplest minimum bias measurement one can make is the average charged particle multiplicity per event $\langle n_{\mathrm{ch}} \rangle$, followed by the charged particle pseudorapidity density $\frac{\mathrm{d}N_{\mathrm{ch}}}{\mathrm{d}\eta}$ and transverse momentum spectrum $\frac{\mathrm{d}N_{\mathrm{ch}}}{\mathrm{d}p_T}$. The latter two are described in detail in the following sub-sections. Both Pythia and Phojet have been shown in the past to give a reasonable description of these observables for a wide range of pp and $p\bar{p}$ data.

At the LHC, these minimum bias studies are possible with very early data (1–10 pb^{-1}), ideally during low-luminosity running, when the number of pp collisions per bunch crossing is less than or equal to 1. At higher luminosities, minimum bias will be a major background, with an average of 18 minimum bias interactions per bunch crossing at LHC design luminosity [3]. It is therefore very important to have an accurate model of minimum bias for all other high-p_T physics measurements. A proper model of minimum bias events will also help characterize the soft part of the underlying event in high-p_T collisions.

2.5.1 Pseudorapidity density

The pseudorapidity distribution of particles produced in pp collisions is strongly correlated with the rate of parton-parton scattering. This is because part of the collision energy that would otherwise have been carried by beam remnants in the forward region is converted into soft particles which populate the central region [23].

Figure 2.2 shows a comparison of PYTHIA and PHOJET predictions for the central charged particle density in NSD $p\bar{p}$ events, over a wide range of center-of-mass energies [3]. The data points shown have been corrected back to the particle level for various effects including detector and trigger efficiencies. Two different tunings of PYTHIA version 6.214 are shown: the ATLAS tune and CDF tune-A. These are compared with the central charged particle density generated by PHOJET version 1.12.

As the collision energy increases, the rate of multiple parton interactions also increases, producing a rise in the central pseudorapidity density. An accurate event generator model should create the right amount of multiple parton scattering, while taking into account the expected variation with the collision energy. One of the main parameters used to regulate the rate of parton-parton interactions in PYTHIA is $p_{T_{\text{min}}}$. Low values of $p_{T_{\text{min}}}$ produce high rates of parton-parton scatterings and hence high particle multiplicity.

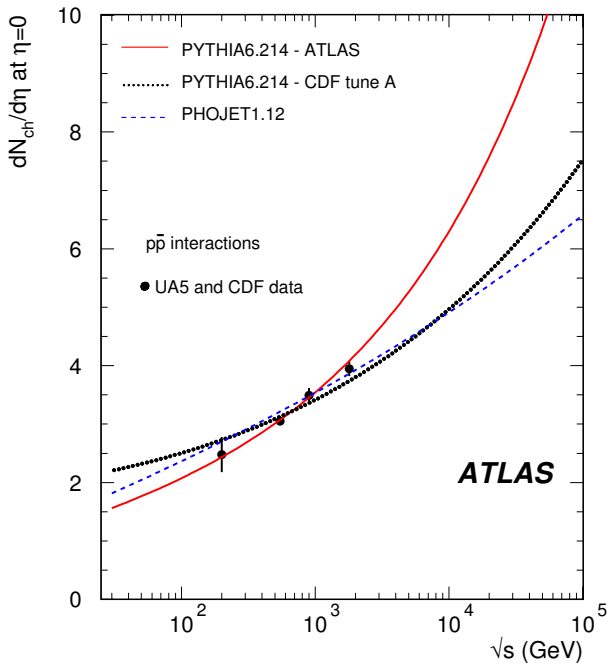

Figure 2.2: Central charged particle density for non-single diffractive inelastic collisions as a function of center-of-mass energy $\sqrt{s}$. The lines show predictions from PYTHIA using the ATLAS tune and CDF tune-A, and from PHOJET. The data points are from UA5 and CDF $p\bar{p}$ data. Taken from [3].

Figure 2.2 shows that PYTHIA and PHOJET predict drastically different behaviors for the central particle density of non-single diffractive interactions at LHC energies, despite having been tuned to agree with data [23]. The uncertainty in these predictions arises because the energy dependence of soft hadronic processes is not well understood. Measuring the central particle density at different LHC collision energies will therefore be crucial for choosing between models and for determining the proper energy dependence [3].

Figure 2.3 shows the charged particle pseudorapidity distribution for inelastic pp collisions generated by PYTHIA and PHOJET at $\sqrt{s} = 14$ TeV. Distributions are shown for the various physics processes separately: single-diffractive, double-diffractive and non-diffractive interactions. The figure shows a plateau in the central region ($|\eta| < 2.5$) and a falling density in the fragmentation region ($\eta \to \eta_{\max}$).

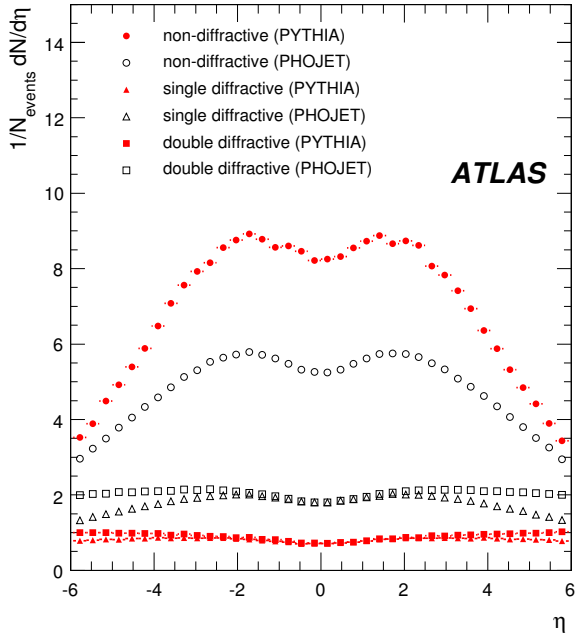

Figure 2.3: Pseudorapidity distribution of stable charged particles in inelastic pp collisions generated by PYTHIA and PHOJET at $\sqrt{s} = 14$ TeV. Taken from [3].

The central charged particle density $\mathrm{d}N_{\mathrm{ch}}/\mathrm{d}\eta|_{\eta=0}$ generated by PYTHIA and PHOJET is 6.8 and 5.1, respectively [23]. In the central region, $\mathrm{d}N_{\mathrm{ch}}/\mathrm{d}\eta$ is about 7 and 5.5, respectively [23]. Thus PYTHIA generates about 27% more charged particles in the central region than PHOJET. The dip at $\eta = 0$ is a consequence of plotting the pseudorapidity η instead of the rapidity y since the two are only equal only for massless particles.

2.5.2 Transverse momentum spectrum

Figure 2.4 shows the p_T spectrum of charged particles produced in inelastic pp collisions generated by PYTHIA and PHOJET at $\sqrt{s} = 14$ TeV. Distributions are shown for the various physics processes separately: single-diffractive, double-diffractive and non-diffractive interactions. Inelastic events at the LHC are expected to be dominated by soft low-p_T particles, with a peak between 0.2 and 0.25 GeV/c.

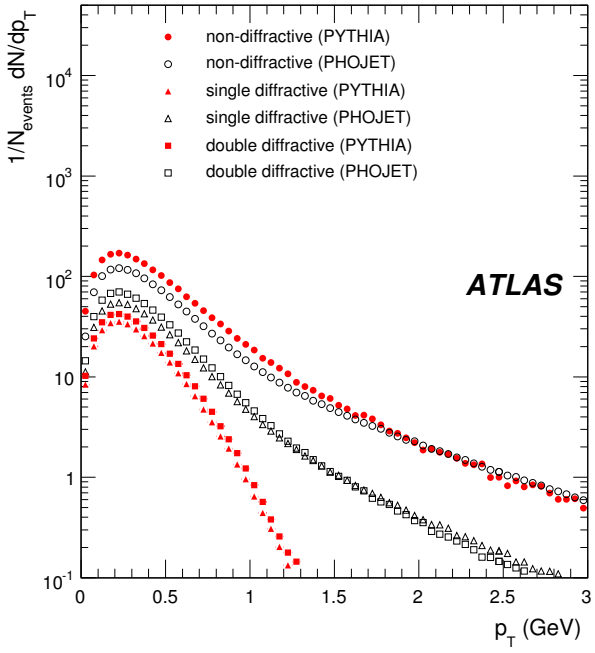

Figure 2.4: Transverse momentum spectrum of stable charged particles in inelastic pp collisions generated by PYTHIA and PHOJET at $\sqrt{s} = 14$ TeV. Taken from [3].

At very low momenta ($p_T \leq 0.5$ GeV/c), the particle density predicted by PYTHIA is about 40% greater than the corresponding PHOJET prediction. At higher values of p_T, the difference is much smaller and both spectra become virtually indistinguishable. The low-p_T bins account for most of the particle multiplicity.

The average transverse momentum $\langle p_T \rangle$ of charged particles in the central region is important since it is very sensitive to the MPI tuning [64]. The PYTHIA and PHOJET predictions for $\langle p_T \rangle$ at $\eta = 0$ in pp collisions at $\sqrt{s} = 14$ TeV are 0.55 GeV/c and 0.64 GeV/c, respectively [23]. This difference of 16% is partly explained by PHOJET generating fewer particles on average than PYTHIA in minimum bias collisions at the LHC. Therefore, PHOJET predicts a greater average p_T per particle than PYTHIA [23].

2.6 Measuring Minimum Bias with ATLAS

The subject of this dissertation is the measurement of the $\mathrm{d}N_{\mathrm{ch}}/\mathrm{d}\eta$ and $\mathrm{d}N_{\mathrm{ch}}/\mathrm{d}p_T$ distributions of charged particles produced in minimum bias pp collisions at the LHC during early low-luminosity running. Both measurements require low statistics (between 10K and 100K events) and can potentially be made using LHC collision data from 'day 1'. Due to the wide range in the predictions of these observables, a first measurement to within 10% can already discriminate between the different models. This gives a starting point for tuning the Monte Carlo event generators in question.

Figure 2.3 shows that minimum bias (NSD) collisions at the LHC are expected to produce between 5.1 and 6.8 charged particles per unit of pseudorapidity at $\eta = 0$. However, ATLAS will only measure a fraction of these particles since the analysis is restricted to the range $|\eta| < 2.5$, due to the acceptance of the Inner Detector (see Chapter 1), and $p_T > 0.15$ GeV/c, due to the poor reconstruction efficiency for tracks below this p_T (see Chapter 4).

It is also important to remember that any minimum bias measurement made by ATLAS will depend on the trigger used for the measurement. Although Figures 2.3 and 2.4 show the individual contributions from single-diffractive, double-diffractive and non-diffractive events, the actual measurement by ATLAS will group all components together, weighted by their cross sections and by the acceptance of the trigger for each type of event. An analysis using a trigger that predominantly accepts non-diffractive events and suppresses single and double-diffractive events would measure the central pseudorapidity density at $\eta = 0$ to be close to the non-diffractive value of about 8 (Pythia prediction). A trigger that accepts all three processes with no bias, such as a random trigger, would only measure about 6 charged particles per unit η since single and double-diffractive collisions do not produce many particles at $\eta = 0$. For this reason it is important to have several minimum bias triggers that select different amounts of each component, since this will help separate the individual contributions [57]. The ATLAS minimum bias triggers are discussed in the next chapter.

Part II

Event & Track Selection

Chapter 3

Minimum Bias Trigger

A minimum bias trigger is intended to select inelastic collisions while avoiding biasing the sample. As the name implies, however, some bias is usually introduced e.g. due to minimum energy thresholds or limited geometrical acceptance of the trigger [3]. Several types of minimum bias triggers have been implemented by ATLAS in order to cover various phases of LHC running. These triggers are described in this chapter. Special focus is given on two of the strategies and a summary of their efficiencies and biases is given. A minimum bias trigger is chosen for the analysis and the final event selection criteria are presented. The trigger studies discussed in this chapter have previously been shown in [3] and are summarized here only for completeness.

3.1 Trigger Strategy

The main backgrounds when triggering on inelastic events are beam-gas collisions and beam-halo interactions. Beam-gas events come from the interaction of circulating protons with residual gas in the beam pipe. They can occur anywhere over the entire length of ATLAS. Beam-halo events come from interactions in the tertiary collimators[1] of the LHC. Both beam-gas and beam-

[1]The tertiary collimators [65] are placed around the interaction points of the LHC in order to protect the superconducting triplets and the detectors from any beam losses.

halo backgrounds can provide spurious triggers that can distort the shape and characteristics of the event sample [3]. Another potential background comes from empty events, or events which contain only noise from the detector. The minimum bias trigger must be able to reject such events in order to optimize the use of the trigger bandwidth [3].

A *random trigger* is an ideal minimum bias trigger since it accepts all types of inelastic collisions equally with zero bias. However, random triggering is very inefficient at low luminosities ($\mathcal{L} < 10^{30}$ cm^{-2}s^{-1}) since the probability of an interaction during a bunch crossing is $< 1\%$ [3]. The random trigger in ATLAS is applied at Level-1 [66] (see Section 1.8) and implemented with beam pickup.

At higher trigger levels, signals in the Inner Detector can be used to suppress empty bunch crossings (noise events). The so-called *spacepoint* and *track triggers* select events with a minimum number of silicon hits or reconstructed tracks or both. The random and track triggers are often combined into a *random-based track trigger* [3]. Implementation of the random-based track trigger in ATLAS is described in Section 3.2.

The spacepoint and track triggers, however, are limited by the acceptance of the Inner Detector ($|\eta| < 2.5$), which is clearly blind to any inelastic events with activity concentrated in the forward region. The alternative is to use trigger hardware dedicated for detecting inelastic or elastic processes. Some examples of these triggers in ATLAS are described in Sections 3.3 and 3.4.

A luminosity of $\mathcal{L} = 10^{31}$ cm^{-2}s^{-1} and a bunch spacing of 75 ns have been used for the trigger studies presented here. The rate of inelastic events under these conditions is 792 kHz, or about 0.06 interactions per bunch crossing on average [3]. Trigger efficiencies have been calculated using 100,000 single-diffractive, double-diffractive and non-diffractive events simulated with Pythia at $\sqrt{s} = 14$ TeV, as well as simulated beam-gas interactions. The trigger efficiency has been calculated as the fraction of events satisfying the trigger logic.

3.2 Random-based Track Trigger

The ATLAS random-based track trigger [3,67] combines random event selection at Level-1 with signals from the Inner Detector in the High Level Trigger. In particular, hit counts from the silicon sub-detectors are used at Level-2 and fully reconstructed tracks are used in the Event Filter. See Section 1.8 for a description of the various trigger levels.

The random trigger at Level-1 prevents bias in the event selection. After a random event selection at Level-1, activity in the Inner Detector is measured at Level-2 by counting the number of *spacepoints*[2] in the pixel and SCT detectors. To reject empty (noise) events, a minimum number of spacepoints is required before the event is passed on to the next trigger level. Tracks are then reconstructed and counted at the Event Filter trigger level. Any events below a minimum number of tracks are discarded.

The performance of the random-based track trigger has been studied in [3, 67, 68]. The Level-2 trigger efficiency as a function of the number of pixel and SCT spacepoints is shown in Figure 3.1. Curves have been drawn for each of the inelastic physics processes (single-diffractive, double-diffractive and non-diffractive) as well as for empty-event and beam-gas backgrounds.

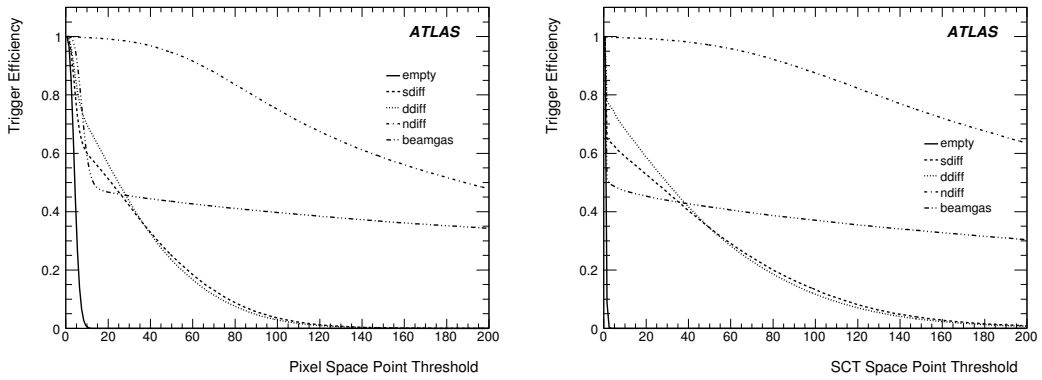

(a) (b)

Figure 3.1: Trigger efficiency at Level-2 versus the number of spacepoints in the pixel (a) and SCT (b) detectors for various physics processes simulated at $\sqrt{s} = 14$ TeV. Taken from [3].

[2]The formation of spacepoints from clusters in the pixel detector or the SCT is described in Section 4.3.1.

The efficiency of selecting empty events drops dramatically with the number of spacepoints. This shows that a modest constraint on either the number of pixel or SCT spacepoints will strongly suppress background events, while preserving almost 100% of the non-diffractive events [3]. A threshold of 12 pixel spacepoints and 3 SCT spacepoints has been chosen in order to obtain a signal-to-background ratio of 100 : 1 (non-diffractive : empty events) [3]. This corresponds to a trigger efficiency for empty events of less than 5×10^{-4}, assuming a 0.05 probability of a pp non-diffractive inelastic interaction [3].

Although the spacepoint trigger considerably reduces the number of accepted beam-gas events at Level-2, this rate can be further reduced in the Event Filter by requiring a minimum number of reconstructed tracks in the Inner Detector. A full track reconstruction scan ($p_T > 0.2$ GeV/c) is performed at the Event Filter for all events passing Level-2. Figure 3.2 shows the trigger efficiency at the Event Filter as a function of the number of reconstructed tracks. Tracks are required to have a longitudinal impact parameter z_0 less than 200 mm [68]. Track parameterization and reconstruction are discussed in more detail in Chapter 4.

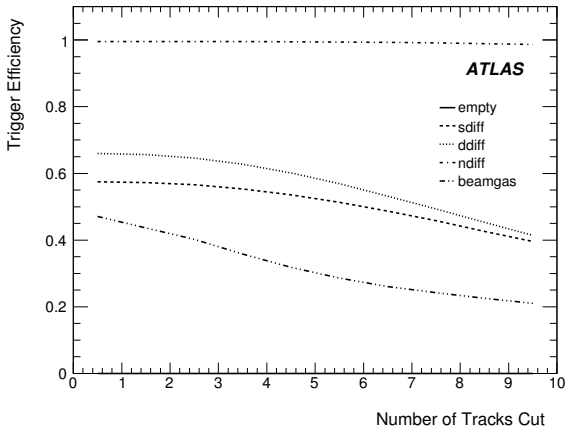

Figure 3.2: Trigger efficiency at the Event Filter versus the number of reconstructed tracks with $z_0 < 200$ mm, for various physics processes simulated at $\sqrt{s} = 14$ TeV satisfying the Level-2 spacepoint requirement. Taken from [3].

A requirement of at least two reconstructed tracks has been proposed in [3], rejecting an additional 10% of beam-gas events. The total rejection of beam-gas events is more than 60% [68]. Since diffractive collisions are also suppressed by this trigger condition, the minimum number of reconstructed tracks should not be increased. A summary of the efficiencies for the ATLAS random-based track trigger can be found in Section 3.6.

3.3 MBTS Trigger

The MBTS trigger [3,69] uses signals from the Minimum Bias Trigger Scintillators [70] to select inelastic events. The MBTS are mounted at $|z| = 3.56$ m, between the Inner Detector and the Liquid Argon calorimeter, covering the pseudorapidity range $2.09 < |\eta| < 3.84$ [71]. The MBTS system is segmented into 16, 2-cm polystyrene-based scintillator counters, with two regions of equal pseudorapidity ($2.09 < |\eta| < 2.82$ and $2.82 < |\eta| < 3.84$) and eight units in azimuth.

The MBTS is a relatively simple and robust detector system that is sensitive to a minimum of detector activity. Signals from the MBTS are read out through the electronics of the hadronic calorimeter, providing a fast Level-1 signal. The electronics also broaden the fast scintillator signals by roughly a factor of 50 [68]. A second trigger path has been installed to take advantage of the excellent time resolution of the scintillators, giving the possibility of distinguishing pp collisions from beam-induced background events [68].

MBTS event selection is performed at Level-1 by requiring energy deposit in one or more counters above a voltage threshold, relative to the bunch-crossing signal. Various MBTS trigger configurations and thresholds have been studied in [3, 69, 71], including requiring a hit coincidence in the system or a total hit multiplicity. Two MBTS trigger strategies are discussed here: `MBTS_1_1` and `MBTS_2`. `MBTS_1_1` is defined as at least one MBTS counter above threshold on each of the forward and backward sides. `MBTS_2` is defined as two or more MBTS counters above threshold anywhere in the system [3].

The Level-1 MBTS trigger efficiency is shown in Figure 3.3 as a function of counter threshold. Curves have been drawn for each of the inelastic physics processes (single-diffractive, double-diffractive and non-diffractive) as well as for empty-event and beam-gas backgrounds. A threshold of 40 mV has been chosen from commissioning with cosmic-ray data [3]. At this threshold setting, empty (noise) events are highly suppressed, while non-diffractive events are efficiently retained, with an expected signal amplitude of around 100 mV [68].

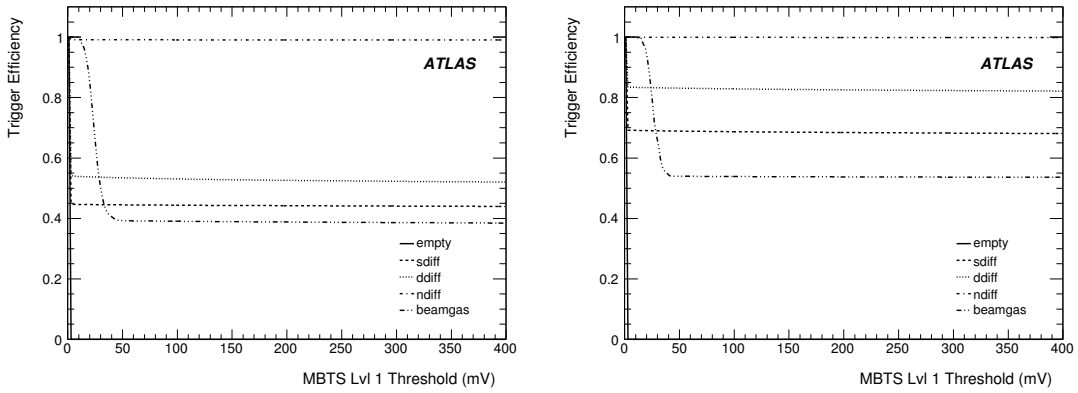

(a) (b)

Figure 3.3: MBTS trigger efficiency at Level-1 versus counter voltage threshold for the `MBTS_1_1` (a) and `MBTS_2` (b) triggers for various physics processes simulated at $\sqrt{s} = 14$ TeV. Taken from [3].

The two plots in Figure 3.3 show a visible difference in the two MBTS configurations for forward-directed events. The `MBTS_2` configuration passes about 30% more of the diffractive events and about 15% more of the beam-gas events [68]. A summary of the MBTS trigger efficiencies can be found in Section 3.6.

The MBTS will play a key role during the commissioning of ATLAS. Major radiation damage is expected after three to four months of running at a luminosity of 10^{33} cm^{-2}s^{-1} [3].

3.4 Other Minimum Bias Triggers

In addition to the trigger strategies presented above, ATLAS has several forward detectors that expand the pseudorapidity coverage and can also be used to trigger minimum bias events. Although full software implementation was not ready at the time of writing, they will be integrated into the minimum bias trigger in the near future. They are mentioned here briefly for completeness.

3.4.1 LUCID

LUCID (LUminosity Cherenkov Integrating Detector) [72,73] is an array of 40 gaseous Cherenkov detectors, primarily dedicated to online luminosity monitoring. The main purpose of the detector is to measure and monitor the relative luminosity delivered to ATLAS by the LHC for each bunch crossing, as well as the integrated luminosity in a certain time period [73]. Due to its intrinsically fast response, it can additionally provide a minimum bias trigger during the low-luminosity phase. Currently there are two modules (2×20 Cherenkov tubes) installed in each end-cap region of ATLAS, at a distance of ±17 m from the interaction point [6]. The radial distance from the beamline is about 10 cm, covering the pseudorapidity range $5.61 < |\eta| < 5.93$.

3.4.2 Zero Degree Calorimeter (ZDC)

The Zero Degree Calorimeter (ZDC) [74] is a set of compact calorimeters located at approximately zero degrees to the incident beams ($|\eta| > 8.3$) and ±140 m from the interaction point. It is primarily meant to determine the centrality of heavy-ion collisions by detecting forward neutrons. The ZDC will also provide an additional minimum bias trigger for ATLAS during the LHC start-up phase. Beam-gas and beam-halo backgrounds can be significantly reduced by requiring a tight coincidence from the two arms of the ZDC. The time resolution of the ZDC is roughly 100 ps, which is sufficient to locate the interaction point to about 3 cm in z [74].

3.4.3 Beam Conditions Monitor (BCM)

The Beam Conditions Monitor (BCM) [75] is designed to distinguish *pp* collisions from other background by making time-of-flight measurements. The BCM can improve the understanding of beam-gas and beam-halo rates. It will be used as an input to Level-1 since it provides a better and cleaner signal than using a random trigger.

3.5 Minimum Bias Trigger Slice

A *trigger slice* is a dedicated portion of the total trigger menu. The current implementation of the minimum bias trigger slice in ATLAS consists of the random trigger, the random-based track trigger (Section 3.2) and the MBTS trigger (Section 3.3) [3]. A schematic view of the minimum bias trigger slice is shown in Figure 3.4. It is also possible to use the MBTS at Level-1 in conjunction with the track trigger in the Event Filter [3], but this is not discussed here.

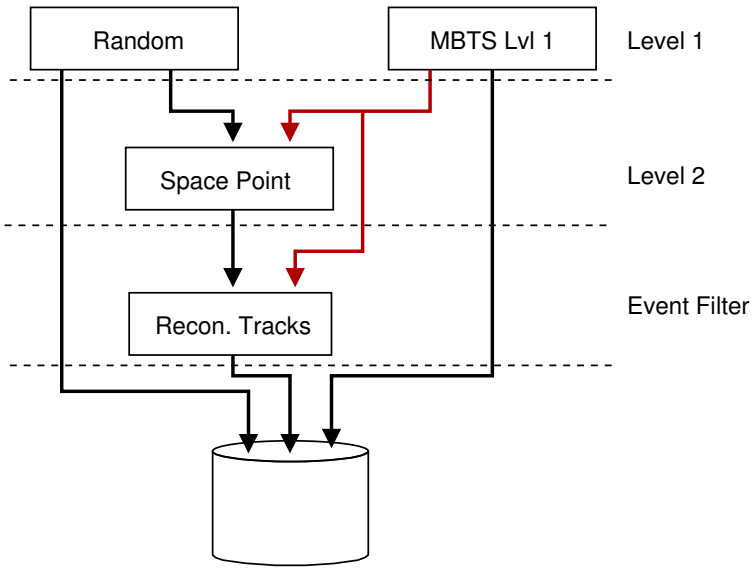

Figure 3.4: ATLAS minimum bias trigger slice, composed of a random trigger (see Section 3.1), a random-based track trigger (Section 3.2) and the MBTS trigger (Section 3.3). Taken from [3].

The three different strategies in the trigger slice have been designed and implemented to cover various phases of LHC running and are therefore optimized for different LHC luminosities. At very low luminosity, the MBTS trigger will be the most useful since it simultaneously rejects empty events, while requiring minimal activity in the detector. Minimal bias on the inelastic event sample is imposed by the use of this trigger. However, the MBTS system is not expected to survive the radiation damage of moderate-luminosity running. The random-based track trigger can also be used at very low luminosity. It does an excellent job of rejecting empty events, but requires somewhat more activity in the detector than the MBTS trigger.

A ratio of 1 : 50 : 50 (random : random-based track : MBTS) has been proposed in [3] for early LHC running. As the beam is focused and the LHC luminosity increases from 10^{31} cm^{-2}s^{-1} to 10^{32} cm^{-2}s^{-1} and higher, the mean number of interactions per bunch crossing will approach 1. The rate of the random trigger relative to the other two trigger strategies can then be increased. When the average number of interactions in a bunch crossing is sufficiently high, the random trigger will be used to record interactions for each crossing without requiring any other triggers in the HLT. The random trigger will efficiently accept a zero-bias inelastic sample for ATLAS.

3.6 Trigger Efficiency and Acceptance

A summary of the trigger efficiencies for the random-based track trigger and the MBTS trigger is given in Table 3.1. Trigger efficiencies are shown for the various inelastic physics processes. Both triggers are highly efficient at selecting non-diffractive events. The diffractive events, however, have much lower trigger efficiencies since these events typically have a lower track multiplicity than non-diffractive events, especially in the central tracking region. The triggers are therefore only sensitive to a fraction of the diffractive cross section [3].

The trigger *acceptance* is defined as the efficiency weighted by the fraction of the inelastic cross section. The acceptances of the two minimum bias triggers are shown in Table 3.2. The acceptance

	MBTS_1_1	MBTS_2	SP	SP & Track
Non-diffractive	99%	100%	100%	100%
Single-diffractive	45%	69%	57%	57%
Double-diffractive	54%	83%	66%	65%
Beam-gas	40%	54%	47%	40%

Table 3.1: Efficiency of two MBTS trigger strategies and the random-based spacepoint (SP) and spacepoint plus track trigger, for various physics processes simulated at $\sqrt{s} = 14$ TeV. Taken from [3].

of diffractive events is significantly suppressed due to the lower trigger efficiencies and the smaller cross sections [3]. The acceptance of the proposed minimum bias triggers is between 84% and 92%, consisting of about 80% non-diffractive events and roughly equal numbers of single and double diffractive events [3].

	MBTS_1_1	MBTS_2	SP	SP & Track
Non-diffractive	69%	70%	70%	70%
Single-diffractive	8%	12%	10%	10%
Double-diffractive	7%	10%	8%	8%

Table 3.2: Acceptance of two MBTS trigger strategies and the random-based spacepoint (SP) and spacepoint plus track trigger, for various physics processes simulated at $\sqrt{s} = 14$ TeV. Taken from [3].

Since the acceptance of the single-diffractive and double-diffractive samples are similar, the ATLAS minimum bias triggers do not select a purely non-single-diffractive (NSD) sample, as experiments in the past have done (see Section 2.4) [3]. Model-dependent corrections are therefore needed to compare measured distributions to results from previous experiments [3].

The MBTS_2 trigger has been chosen for the minimum bias analysis due to its high acceptance of inelastic events and sensitivity to activity in the forward pseudorapidity region.

3.7 Trigger Bias

The trigger *bias* is defined as the fraction of primary charged particles in events passing a given trigger over the number of primary charged particles in all events. In the case of minimum bias, it is a measure of how much a particular trigger distorts the shape of the inelastic event sample.

Figure 3.5 shows the bias of the `MBTS_2` trigger as a function of pseudorapidity (η) and transverse momentum (p_T), for a sample of 14,650 simulated inelastic pp events. Generation and simulation of the inelastic event sample are described in Appendix A. The bias in η is uniform and close to unity (zero bias) over the acceptance of the Inner Detector ($|\eta| < 2.5$). This is partly because the coverage of the MBTS extends up to $|\eta| < 3.8$. The bias in p_T also approaches unity over most of the p_T range of interest. The small (0.02%) bias observed at low p_T is due to the lower acceptance of single and double diffractive events which have on average lower transverse momentum.

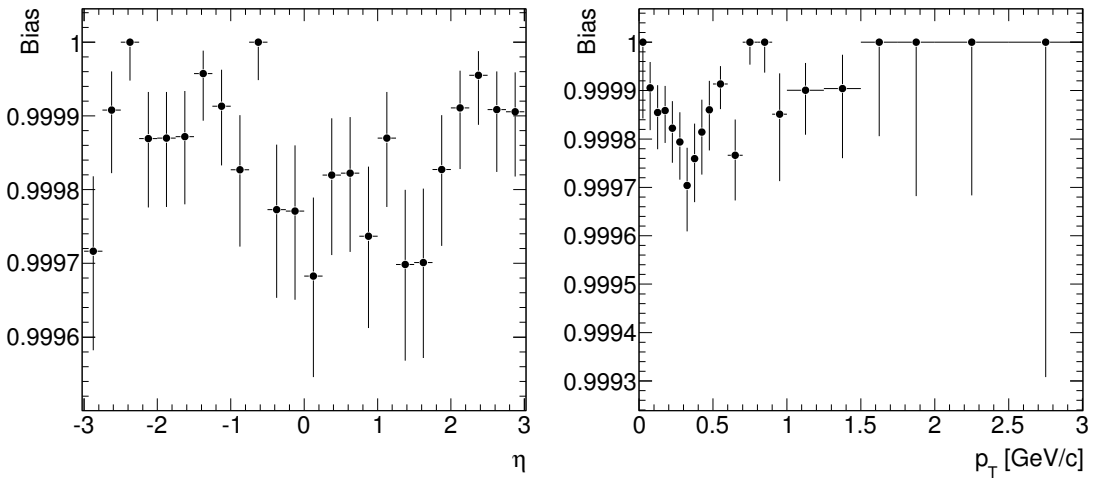

(a) (b)

Figure 3.5: Bias of the `MBTS_2` trigger as a function of η (a) and p_T (b) for the simulated inelastic event sample described in Appendix A. The η plot is integrated over $p_T > 0.15$ GeV/c and the p_T plot is integrated over $|\eta| < 2.5$.

3.8 Event Selection

The analysis presented in Chapter 6 uses a set of events that have been selected from a sample of simulated inelastic events according to the following criteria:

- the event must be triggered by the `MBTS_2` minimum bias trigger, as defined in Section 3.3; and
- the event must contain one reconstructed primary vertex, with at least 2 associated tracks and a reconstructed z position v_z satisfying $|v_z| < 200$ mm.

The requirement of a primary vertex is necessary for track selection, as will be discussed in Section 5.6. Primary vertex reconstruction is discussed in Section 4.7.1. It is important to be confident that each event contains a single primary vertex. An additional criterion should be added to exclude events with multiple collisions once the software for tagging these *pile-up* events has been developed. However, this can safely be ignored during early, low-luminosity running of the LHC (see Section 7.4). All events studied here have been simulated with only one interaction per bunch crossing.

The sample of events studied in the following chapters does not contain any beam-gas or beam-halo events. An estimate of the systematic error associated with contamination from beam-gas and pile-up events is given in Section 7.4.

Chapter 4

Inner Detector Tracking

The reconstruction of charged particle tracks is an essential part of every physics analysis at the LHC. There are two independent tracking devices in ATLAS: the Inner Detector (see Section 1.5) and the Muon Spectrometer (see Section 1.7). Reconstruction in the Inner Detector must deal with a high track density and a large number of combinatorial track candidates. Reconstruction in the Muon Spectrometer must cope with a huge amount of inert material, a highly inhomogeneous magnetic field, and high levels of background in the experimental cavern[1].

Reconstruction in the Inner Detector is discussed in detail in this chapter. Muon Spectrometer reconstruction is not used in the minimum bias analysis and will therefore not be discussed here.

4.1 New Tracking

The track reconstruction software in ATLAS is called New Tracking (NewT) [76]. It has a flexible, modular design that covers the requirements of both Inner Detector and Muon Spectrometer reconstruction. Reconstruction tools common to both, such as track extrapolation, track fitting (including material corrections) and vertex fitting, have been standardized to use a single event

[1] The intense beams and large cross sections at the LHC give rise to a high flux of low-energy neutrons and photons in the cavern.

data model [77] and detector description [78]. These tools will be explained in various parts of the chapter.

The sequence of track reconstruction in the Inner Detector is sub-divided into three steps [6]: pre-processing, track-finding and post-processing. In the pre-processing stage, raw data from the pixel and SCT detectors are converted into clusters and spacepoints and the TRT raw timing information is translated into calibrated drift circles. In the second stage, several track-finding strategies optimized for different applications are implemented. Pattern recognition and track fitting are both incorporated into this single step. In the post-processing stage, dedicated algorithms are used to reconstruct primary and secondary vertices. Association to truth information is also handled during this last stage.

Each of the steps are described in more detail in the following sections. Definitions of the ATLAS track parameters are given first.

4.2 Track Parameterization

The track parameterization defined in the ATLAS Event Data Model (EDM) [77] is slightly different from the helix-based parameterization commonly used in other high energy physics experiments. This is because the EDM parameterization is used by both the Inner Detector and the Muon Spectrometer, which have somewhat perpendicular magnetic field setups. Therefore, a parameterization has been chosen that is closely bound to the constants of motion in both tracking devices [79].

The perigee representation in the Inner Detector is used to express the closest approach to the nominal interaction point. The *perigee* is the point of closest approach to the z-axis. This representation is described by the parameterization [79]:

$$\tau_i \quad = \quad (d_0,\ z_0,\ \phi,\ \theta,\ q/p). \tag{4.1}$$

Figure 4.1 shows the track parameters in Equation 4.1 at the perigee. ϕ_0 is the angle in the x-y plane at this point, and θ is the angle with the z-axis. d_0 is the signed distance to the z-axis, defined to be positive when the direction of the track is clockwise with respect to the origin. z_0 is the z coordinate of the perigee. The fifth parameter q/p is related to the curvature and is calculated as the charge of the particle divided by the momentum.

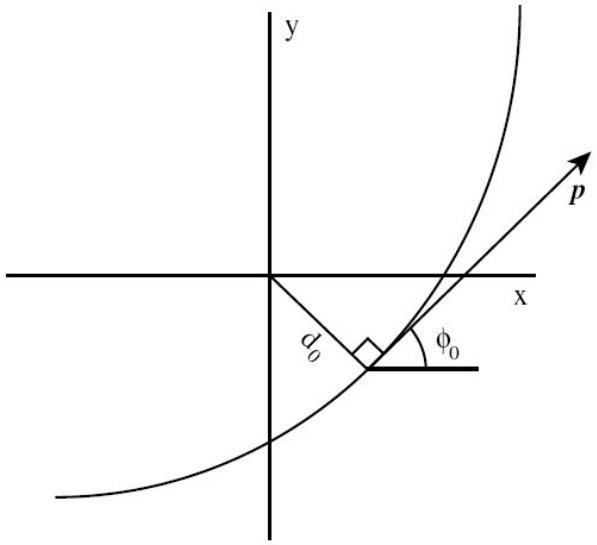

Figure 4.1: Track parameter definitions at the perigee. Taken from [15].

A purely helix-based track parameterization can be chosen for convenience when studying only Inner Detector tracks [79]:

$$\tau_i \quad = \quad (d_0,\ z_0,\ \phi,\ \cot\theta,\ q/p_T). \tag{4.2}$$

The track parameters are often divided into the strongly correlated transverse parameters (d_0, ϕ, q/p_T) and their longitudinal counterparts (z_0, $\cot\theta$). The longitudinal impact parameter should be transformed from the global frame to the helical frame at the point of closest approach. Taking this into account, the longitudinal component of the impact parameter in three dimensions is given as $z_0 \sin\theta$ [79].

4.3 Pre-processing

In the pre-processing stage of the ID track reconstruction, raw data from the silicon and TRT detectors are translated into positions in space using the detector geometry and other calibrations.

4.3.1 Spacepoint formation

Measurements from the silicon detectors are converted into three-dimensional representations, called *spacepoints*. This is relatively trivial for the pixel detector since the modules provide a local, two-dimensional measurement. A spacepoint can easily be made by taking the center of a cluster of pixels and using the module position to apply a simple local-to-global transformation [76].

In the SCT however, single clusters cannot be directly transformed into spacepoints since the precision measurement is only given orthogonally to the silicon strip direction [76]. Instead, the SCT sandwich module structure (see Section 1.5.2) is exploited and a spacepoint is constructed by finding the intersection of the strips on the front and back sides of a module. Because this intersection depends on the angle between the track and the module, there is an inherent uncertainty in the reconstructed spacepoint (apart from the measurement resolution of the individual strip planes) [15]. For this reason, the spacepoints are only used in the pattern recognition, whereas the track-fitting uses the individual pixels and strip clusters.

In contrast to the pixel detector where each cluster directly leads to a spacepoint, the formation of spacepoints in the SCT features an intrinsic noise suppression since one spacepoint requires two different modules with separate readout [76].

4.3.2 Drift circle formation

The raw drift time measurement from the TRT is converted into a drift radius using a calibrated model extracted from simulated and real data. The calibration includes a channel-dependent offset, useful for grouping channels with the same front-end electronics.

4.4 Track Finding

Several track-finding strategies are implemented in NewT. The second stage of track reconstruction currently covers three sequences. The primary method, called *inside-out* tracking, starts in the silicon detectors and then extrapolates to the TRT to collect any matching hits. A second iteration of the inside-out pattern recognition is then run to find low-p_T tracks with large curvature in the ID and kinked objects due to bremsstrahlung. Finally, a complementary track-finding strategy, called *back-tracking* or *outside-in* tracking, searches for unused track segments in the TRT and extends these segments into the silicon detectors. The back-tracking improves the tracking efficiency for secondary tracks from conversions and decays of long-lived particles. A minimum transverse momentum $p_T \geq 0.5$ GeV/c is required for the inside-out and back-tracking sequences. Tracks with $p_T \geq 0.5$ GeV/c fully traverse the Inner Detector, ensuring high reconstruction quality (see Figure 4.2 on page 68).

4.4.1 Inside-out track reconstruction

Inside-out tracking is the default strategy in NewT. It exploits the high granularity of the pixel and SCT detectors to find charged particle tracks originating from the interaction region, known as *prompt* tracks [6].

The inside-out strategy starts by looping over combinations of spacepoints and forming *track seeds*. The seed search marks the global part of the pattern recognition. It can be performed with or without a z-vertex constraint. In the constrained seed search, pairs of spacepoints are found using only the pixel detector and z vertices are built from those pairs [76]. A fast primary vertex search is performed and the primary vertex is used to further constrain the seeds with three or more space points. The unconstrained search forms seeds using the three pixel layers and the first SCT layer [6]. This leads to a significantly higher number of initial track seeds and increased processing

time, but is more efficient for finding tracks in events with loosely constrained primary vertices [76]. Unconstrained seeding is the default in the current version of the ATLAS software (15.3.0.2).

The track seeds provide sufficient directional information to build *roads* of detector elements [76]. A narrow road is built along each seed and the silicon clusters that fall within this road are collected into a *track candidate*. This spacepoint-seeded track finding marks the beginning of the local part of the pattern recognition. A Kalman fitter-smoother formalism is used to simultaneously follow the trajectory and include successive hits in the track candidate fit [76]. This formalism progressively updates the track information (including the covariances) at each measurement and can therefore precisely predict the track representation at the next measurement. Only about 10% of seeds are successfully extended to a track candidate [76].

Many of the resulting track candidates share hits, are incomplete or describe *fake tracks*, i.e. tracks for which the majority of associated measurements do not originate from one single particle [76]. The track candidates are therefore resolved by an *ambiguity processor* before continuing. Tracks are first refit using a detailed material description. Afterwards they are classified according to a *track scoring* strategy [80], which forms an overall score based on the fit quality (χ^2), the number of hits and the number of holes, i.e. silicon sensors crossed by a track without generating any associated cluster[2]. Quality cuts are incorporated into the track scoring by penalizing tracks which, for example, have holes in the first two layers of the pixel detector.

The ambiguity processor is also responsible for handling tracks with hits that are shared between tracks. Shared hits are typically assigned to the track with higher score. The track with the lower score is refit without the shared hit, re-scored and re-entered into the remaining list of tracks to be evaluated. The tracks with the highest scores are selected in an iterative procedure [76]. Hit sharing is only allowed in cases where the track fulfills certain quality criteria. This is to account for ambiguities between hits from ganged pixels (see Section 1.5.1).

[2]Note that a hole is not counted if no hit is expected due to e.g. a known defective channel or module failure.

Refit silicon tracks passing the ambiguity processor are then extended into the TRT. A road is formed along the extrapolated track and the TRT measurements falling within this road are collected. Left/right ambiguities for the TRT drift circles are also solved [76]. The extended tracks are then refit with the full information from all three sub-detectors. The quality of the refit track is evaluated with respect to the original silicon-only track. Any hits on the track extensions resulting in a bad fit are labeled as *outliers*, i.e. they are kept as part of the track, but are not included in the fit [6]. Silicon hits can also be flagged as outlier measurements during the refitting. Using a similar scoring procedure as in the ambiguity processor, the scores of the extended track and the silicon-only track are compared and the track with the highest score is kept.

4.4.2 Low-p_T tracking

The primary inside-out sequence is aimed at finding tracks with $p_T \geq 0.5$ GeV/c. The peak of the p_T spectrum in minimum bias events, however, is about 0.25 GeV/c (see Section 2.5.2). Reconstruction of these low-p_T tracks is difficult due to their large curvature in the magnetic field of the Inner Detector and high degree of multiple scattering. Tracks with p_T below 0.5 GeV/c may also fail to reach the outer layers of the ID, leaving a reduced number of hits in the detector. Figure 4.2 shows the curvature and reach of low-p_T tracks in the Inner Detector.

To overcome these difficulties without disturbing the primary reconstruction sequence, an additional strategy dedicated to finding low-p_T tracks is employed by NEWT. The low-p_T tracking runs a second iteration of the inside-out pattern recognition using a specialized set of track-finding packages. To aid the reconstruction, the event is first cleaned by discarding any silicon hits that were used during the first iteration. The pattern recognition is then re-run with a set of parameters tuned for finding low-p_T tracks. For example, the spacepoint track seeding is modified to use looser internal cuts. Also, the cut on the number of precision hits is reduced to at least five hits. The default minimum p_T cut for the low-p_T tracking is 0.1 GeV/c. A maximum p_T cut of 0.8 GeV/c is applied to allow for some overlap with the primary reconstruction sequence. In some cases, ineffi-

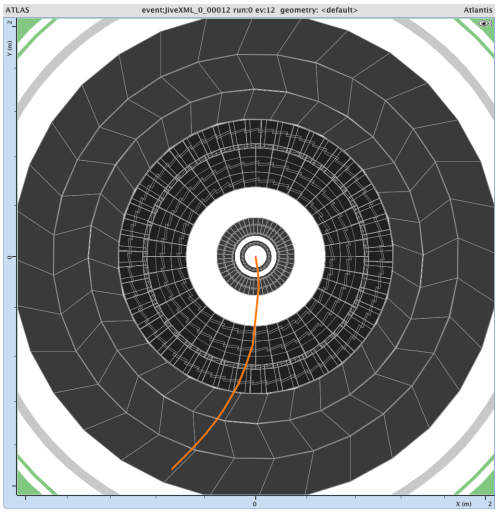

(a) $p_T = 0.5$ GeV/c

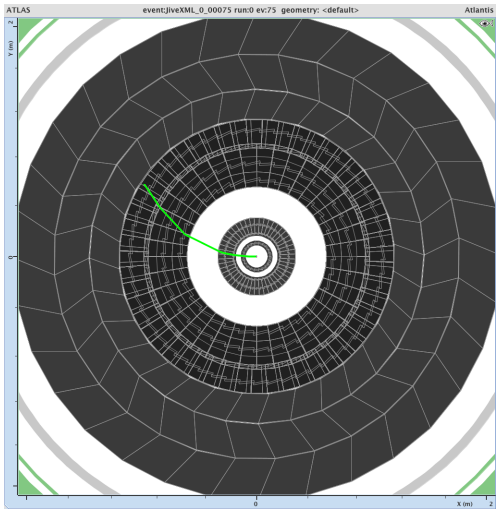

(b) $p_T = 0.25$ GeV/c

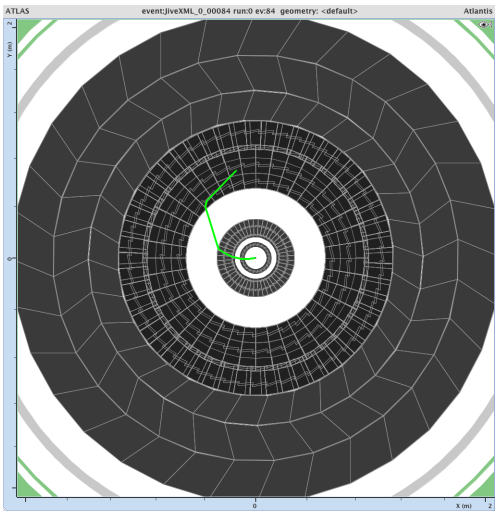

(c) $p_T = 0.1$ GeV/c

Figure 4.2: Curvature and reach of low-p_T tracks in the Inner Detector. A track with $p_T = 0.5$ GeV/c (a) reaches the end of the TRT. A track with $p_T = 0.25$ GeV/c (b) reaches the end of the SCT. A track with $p_T = 0.1$ GeV/c (c) reaches only the middle of the SCT.

ciencies for $0.5 \leq p_T < 0.8$ GeV/c are also recovered. A discussion of tracking efficiency and fake rate is deferred to Chapter 5.

The modified software packages used by the low-p_T tracking have been fully integrated into the standard Inner Detector reconstruction framework for software versions 14.0.0 and later. Although not turned on by default, the low-p_T tracking can be enabled by simply setting `InDetFlags.doLowPt = TRUE`. Table 4.1 lists the set of modified packages, along with the initial tags integrated into the standard `InnerDetector` and `Tracking` software.

The changes in the `InDetRecTools` packages mainly concern the algorithms of the spacepoint-seeded track finder, especially the road builder used during local track reconstruction. The modified packages use a looser set of constraints to allow for tracks with greater curvature. The direction of the tracks is also allowed to change sign in cases where the track does not reach all detector elements in the Inner Detector.

Package	**Version**	**Software release**
`InDetExample/InDetRecExample`	01-08-24	14.0.0
`InDetRecTools/InDetTrackSummaryHelperTool`	01-03-06	13.0.X nightly
`InDetRecTools/SiSpacePointsSeedTool_xk`	00-00-45	13.0.30
`InDetRecTools/SiDetElementsRoadTool_xk`	00-00-38	13.0.30
`InDetRecTools/SiCombinatorialTrackFinderTool_xk`	00-00-09	13.0.30
`InDetRecTools/SiTrackMakerTool_xk`	00-00-55	13.0.30
`TrkFitter/TrkKalmanFitter`	01-11-01	13.0.X nightly
`TrkFitter/TrkGlobalChi2Fitter`	00-01-30-05	13.0.X nightly
`TrkFitter/TrkFitterUtils`	02-03-08	13.0.X nightly
`TrkFitter/TrkDynamicNoiseAdjustor`	00-00-11	13.0.X nightly
`TrkVertexFitter/TrkVertexSeedFinderTools`	00-02-02	13.0.X nightly
`TrkExtrapolation/TrkExRungeKuttaPropagator`	01-01-26	13.0.30

Table 4.1: `InnerDetector` (*top*) and `Tracking` (*bottom*) software packages modified for low-p_T reconstruction, with the initial tags integrated into the ATLAS software.

The changes in the `Tracking` packages are primarily responsible for modifying the logic used to properly sort hits coming from curved low-p_T tracks. The packages also prevent the reconstruction from crashing when the default minimum p_T cut is lowered. None of the packages listed in Table 4.1

change the standard inside-out pattern recognition. In this sense, the low-p_T reconstruction can be considered an extension of the primary inside-out track-finding sequence.

The packages listed in Table 4.1 have been continuously updated since they were introduced into the ATLAS software.

4.4.3 Outside-in track reconstruction

The final track-finding sequence in NEWT uses an outside-in approach, starting with segments in the TRT and then performing a successive *back-tracking* of the segments into the silicon detector. In order to reduce processing time and minimize double counting, the outside-in sequence excludes any TRT hits or silicon spacepoints that have already been assigned to inside-out tracks [3].

The outside-in approach is meant to complement the primary inside-out strategy by covering cases where the initial silicon track seeds may not be found. For example, tracks coming from secondary vertices further inside the Inner Detector volume (e.g. K_s decays) or from photon conversions may have an insufficient number of silicon hits to be found by the inside-out sequence. Ambiguous hits may also prevent a silicon-seeded track from surviving the ambiguity processor [76]. Finally, substantial energy loss (mostly of electrons) at the outer edge of the silicon track may incorrectly guide the track into the TRT, causing the pattern recognition to miss the associated TRT hits [76].

The algorithm responsible for finding segments in the TRT is based on the XKALMAN program [81]. It starts with a global pattern search, followed by local pattern recognition with intrinsic track segment building [76]. The global pattern recognition is done in projective planes since the TRT drift tube measurements do not provide any information about the coordinate along the straw direction. The R-ϕ (barrel) and R-z (end-cap) planes have been chosen as the most adequate for the geometry of the TRT. In these projections, tracks with $p_T > 0.5$ GeV/c coming (roughly) from the primary interaction region, appear as (almost) straight lines [76].

The Hough transform [82] is used to find the hit pattern by transforming the appropriate projection plane into the parameter space of the straight line. Thus, the global search for track

segments is reduced to finding local maxima in a two-dimensional histogram. This histogramming is done for several η slices in order to reduce the number of overlaying track segments. The track segment candidates provided by the histogram method are then used to build track segments using a Kalman filter-smoothing formalism (as was used in the inside-out tracking). While the global Hough transform uses the center straw position to find compatible sets of hits, the local pattern recognition process also uses the drift time information [76].

In the second step of the outside-in strategy, extensions from the silicon sub-detectors are added to the reconstructed TRT segments. A search for spacepoint seeds in narrow R-ϕ wedges of the silicon tracker is performed using directional information given by the TRT segment. The search is confined to the last three SCT layers, with a minimum of two spacepoints [3]. Using the first hit in the initial TRT segment as a third measurement point, a cut on the curvature is applied to reduce the number of spacepoint combinations [3].

The initial fit of the TRT segment can be significantly improved using these spacepoint seeds. The combinatorial Kalman fitter-smoother technique is then applied to produce complete silicon track extension candidates [3]. Ambiguity resolving and track refitting follow afterwards. The final set of *resolved tracks* is stored in a dedicated track collection. Any TRT segments that have not been assigned a silicon track extension are transformed into TRT *stand-alone tracks* and stored in a distinct track collection.

4.4.4 Track collection merging

Following the track-finding, but before any post-processing, the track collections produced by the different strategies of NewT are merged. One last ambiguity resolving is performed in order to select unique tracks from all four collections. However, this is mostly for consistency since the TRT hits and silicon spacepoints associated with the inside-out tracks and low-p_T tracks were already excluded before the outside-in track reconstruction. The merged track collection is considered the final track collection for NewT.

4.5 Track Fitting

The track fitter is responsible for computing the best possible estimate of the track parameters given a collection of hits from the pattern recognition. Track fitting in NEWT can be performed on a set of non-calibrated hits or calibrated measurements, or as a re-fit of a given track or track segment [76]. Only a few additional parameters are needed to specify the fitting procedure: a hypothesis of the particle type (for correctly integrating material effects) and a possible steering of the outlier logic [76].

There are currently six different fitting techniques implemented in NEWT. The track fitter used for the reconstruction can be chosen during configuration.

- The **Global χ^2 Fitter** [15] uses a global χ^2 minimization algorithm to perform robust track fitting. It was recently chosen as the default fitter in NEWT and is described in more detail in the following section.

- The **Kalman Fitter** [83] is a straightforward implementation of the Kalman filter technique, adapted for track fitting. It combines forward filtering, backward smoothing and outlier rejection, while using an extrapolator tool [84], along with the detector geometry, to predict filter steps [76].

- The **Distributed Kalman Fitter** is a modified version of the Kalman filter that estimates the track parameters only for the perigee representation, leading to a significant reduction in computation time. It is mainly used by the Inner Detector Level-2 Trigger and Event Filter.

- The **Alignment Kalman Fitter** [85] is an extended version of the Kalman Filter that integrates the update of the detector surface orientation and position into the intrinsic measurement update of a Kalman filter step [76]. This approach is useful for track-based alignment procedures.

- The **Gaussian Sum Filter** [86] is a special multi-Gaussian extension of the standard Kalman fitter, aimed at the reconstruction of electrons. In this approach, the probability density function of the electron energy loss is modeled by a mixture of several Gaussian functions.

- The **Deterministic Annealing Filter** [87] extends the Kalman Filter by adding a probabilistic description of the measurement assignment to a track. This allows for proper handling of noise and ambiguities during the track fit, for example in the TRT[3]. Details about the actual implementation of the DAF concept in NewT can be found in [88].

4.6 Global χ^2 Fitter

Global χ^2 minimization [89] is a commonly-used technique for track fitting in modern high-energy physics experiments [90]. The χ^2 function is calculated from the hit *residuals*, i.e. the difference between the measurement position (hit) and the position predicted by the track, at every measurement surface. It is defined as [15]

$$\chi^2 = \sum_{i=1}^{N} \frac{r_i^2}{\sigma_i^2}, \tag{4.3}$$

where r_i are the residuals and σ_i are their errors. According to the Gauss-Markov theorem, minimization of Equation 4.3 will lead to the best estimate of the track parameters if the residuals have Gaussian distributions [15].

To calculate the residuals, the fitter uses an extrapolator tool [84] to propagate the track parameters from one measurement surface to another. The residual is then the difference between the measurement and the propagated track. All hits are treated as one-dimensional measurements, with the exception of pixel hits, which are split into two one-dimensional measurements. Expressions for the derivatives of the residuals with respect to the track parameters and the track error at each hit can be found in [15].

[3]The TRT shows a left/right ambiguity for each measurement which must be solved during pattern recognition and track fitting.

Given the residuals and their derivatives, the χ^2 function can be linearized for small changes in the track parameters, i.e. assuming the residuals depend linearly on the track parameters [15]. The best track parameters are then calculated by solving the resulting set of linear equations via a matrix inversion. The number of global parameters in the χ^2 function must therefore be kept low to minimize CPU time.

A major advantage of the global χ^2 fitter is that it only needs an initial estimate of the track parameters and not of their errors. The initialization of the covariance matrix can be a delicate point in the Kalman fitter [15]. The global χ^2 fitter can also solve left/right ambiguities in the TRT in the event that the pattern recognition initially guesses the wrong solution. Another advantage is that the global χ^2 fitter can use hits from any tracking detector, making it independent of detector technology.

Material corrections

The global χ^2 fitter can correct for material interactions such as multiple scattering and energy loss (both Bethe-Bloch and Bethe-Heitler). These material effects enter the χ^2 function as additional fitting parameters. The fitter uses the extrapolation package in combination with the ATLAS detector description [78], which provides a detailed description of the active and passive material in the detector in terms of scattering planes [76]. The scattering planes are themselves described in terms of radiation lengths and are used to estimate and fit the multiple scattering and energy loss at each of the planes. Multiple scattering is treated by allowing the track to change its direction at each scattering plane.

For the purpose of calculating the material corrections, only three types of particles are considered: muons, electrons and pions. No distinction between different hadrons is done since particle identification is carried out at a later stage in the event reconstruction. More details on calculating material corrections due to multiple scattering and energy loss can be found in [15].

4.7 Post-processing

In the last stage of track reconstruction, a set of algorithms is executed dedicated to reconstructing primary and secondary vertices and to associating reconstructed data with Monte Carlo truth information.

4.7.1 Primary vertex reconstruction

Primary vertex reconstruction is an important component of the higher-level tracking algorithms. Reconstructed tracks must be associated to a particular vertex candidate (*vertex finding*) and the position and corresponding covariance matrix of the vertex must be reconstructed (*vertex fitting*). Both the 'finding-through-fitting' and 'fitting-after-finding' approaches are implemented in the ATLAS software [91].

The **Adaptive Multi Vertex Fitter** is the current, default primary vertex-finding strategy in ATLAS. It is an example of the 'finding-through-fitting' approach. The algorithm starts by selecting tracks likely to originate from the interaction region. A single primary vertex candidate is then formed using all selected tracks. Any tracks considered to be outliers are used to create a new vertex seed. A simultaneous fit of the two vertices is then performed. The procedure is iterated, causing the number of vertex candidates to grow, but allowing these candidates to compete with each other in order to gain more tracks. The annealing procedure prevents the finding procedure from falling into local minima [91].

The `InDetPriVxFinder` algorithm is an example of the 'fitting-after-finding' approach in ATLAS. In this strategy, tracks coming from the interaction region are preselected and primary vertex candidates are formed by searching for clusters of tracks in the longitudinal projection. One vertex fitter is used to iteratively fit these clusters, with the possibility of rejecting outliers at every iteration. The maximum number of reconstructed vertices is thus fully determined at the seeding stage. Once a track is rejected from a vertex candidate, it is never used for any other cluster [91].

Previous studies have shown that the Adaptive Multi Vertex Fitter provides a more robust approach in comparison to other finders, since the number of vertex candidates can be changed during the algorithm [91]. It also efficiently deals with outlier tracks. The resolution on the transverse positions (v_x, v_y) of reconstructed primary vertices are similar in both fitters: about 10 μm to 12 μm, depending on the approach and the kinematics of the channel [91]. The calculated errors on the resolution values are typically smaller than 1 μm [91]. The resolution on the longitudinal position (v_z) is typically on the order of 35 μm to 55 μm [91].

A discussion of primary vertex reconstruction efficiency is postponed until Section 6.5. More details on primary vertex finding in ATLAS can be found in [91].

4.7.2 Truth association

The association of reconstructed data with Monte Carlo truth information is referred to as *truth association*. Truth association is done on two different levels: hit-truth level and track-truth level. A third level of truth association is also performed while converting to different data formats, but this is not discussed here.

The hit-truth association relates the silicon clusters and TRT drift circles to the simulated hits and (through 'back-navigation' of the Monte Carlo record) to the generated Monte Carlo particle. Since it is possible for one cluster (or drift circle) to be constructed from several simulated hits caused by different generated particles, the hit-truth association is implemented using assignment probabilities that allow this multiple relationship [76].

The track-truth association relates the reconstructed tracks with the generated Monte Carlo particles. This association can become complicated since many interaction processes in the GEANT [92] detector simulation change the identifier, or *barcode*, of the particle [76]. Thus, simulated tracks are represented not by a single generated particle, but by a chain of generated particles, called a *trajectory*, connected through mother-daughter relationships. In the tracking realm, however, the given chain of truth particles is still reconstructed as a whole. For this reason, a track can corre-

spond to one or many generated particles. The track-truth association is therefore implemented as a one-to-many relationship [76]. The truth trajectory with the highest amount of hit-truth association is chosen as the best match for a given track. This is discussed in more detail in Section 5.4.

In the next chapter, the hit-truth and track-truth association are used to study the performance of the Inner Detector tracking software.

Chapter 5

Tracking Performance

In this chapter, the performance of the ATLAS Inner Detector tracking software is evaluated using a sample of 13,500 simulated minimum bias events. Track selection criteria are defined and used to select a subset of reconstructed tracks best suited for the minimum bias analysis. The effectiveness of the track selection is also evaluated. The results in this chapter show the combined performance of the pattern recognition and track fitting algorithms. Details on the generation, simulation and reconstruction of the minimum bias event sample are given in Appendix A.

5.1 Track Parameter Resolutions

An important measure of the tracking performance is the *resolution* of the track parameters, defined as the standard deviation (sigma) of the residual distribution. Here, the residual refers to the difference between the reconstructed and the true track parameter. Track parameter resolutions can be calculated as a function of some variable X (typically η, p_T, or the track parameter itself) by first calculating the residual distribution as a function of X and then calculating the sigma for each slice in X. Note that the sigma used here is equivalent to the one obtained using a maximum likelihood fit to a Gaussian.

The resolution of a track parameter X can be expressed as a function of p_T as [3]:

$$\sigma_X(p_T) \quad = \quad \sigma_X(\infty) \left(1 \oplus \frac{p_X}{p_T}\right), \tag{5.1}$$

where $\sigma_X(\infty)$ is the asymptotic resolution expected at infinite momentum and p_X is a constant representing the p_T value for which the two terms in the equation are equal. The first term represents the intrinsic resolution of the tracker, which depends on the resolution of the position measurements and the strength of the magnetic field. The second term represents the degradation of the resolution due to multiple scattering. The two terms are summed in quadrature, denoted by the $\oplus$ symbol.

Equation 5.1 is approximate, working well at high p_T, where the resolution is dominated by the intrinsic detector resolution, and at low p_T, where the resolution is dominated by multiple scattering [3]. $\sigma_X(\infty)$ and p_X are implicitly functions of η, since particles have to traverse more material as the η increases due to the angle of incidence with the material layers. Values of $\sigma_X(\infty)$ and p_X for each track parameter in the barrel and end-cap regions can be found in [3].

Figures 5.1 and 5.2 show the resolutions of the five track parameters as a function of η and p_T, respectively, for the minimum bias event sample. The data points are taken as the standard deviation of the residual distributions for each η and p_T bin. To match the definition in [6], the resolution is calculated over a range which includes 99.7% of the data (corresponding to $\pm 3\sigma$). Mis-alignment of the Inner Detector is not considered here. A study of the impact of mis-alignment on the impact parameter resolutions can be found in Section 7.5.

The plots in Figures 5.1 and 5.2 contain a mixture of pions, kaons, muons and electrons. Muons typically yield the best track parameter resolutions since they leave the cleanest trace in the detector. The vast majority of tracks in minimum bias events, however, come from pions. Pions typically undergo nuclear interactions with the detector material that can degrade the resolution by effectively shortening the track length or adding an additional deflection to the Coulomb multiple scattering [79].

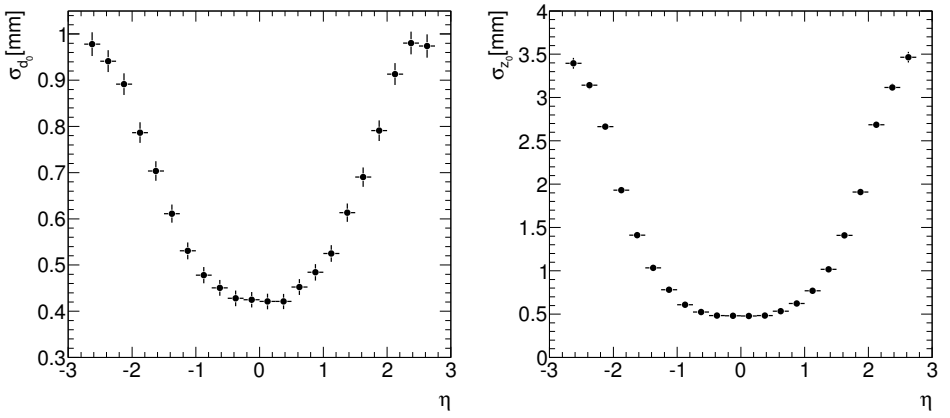

(a) d_0

(b) z_0

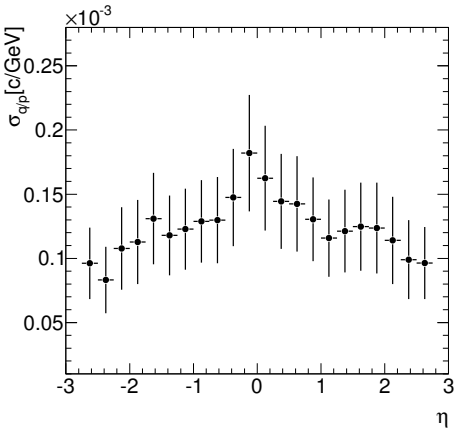

(c) q/p

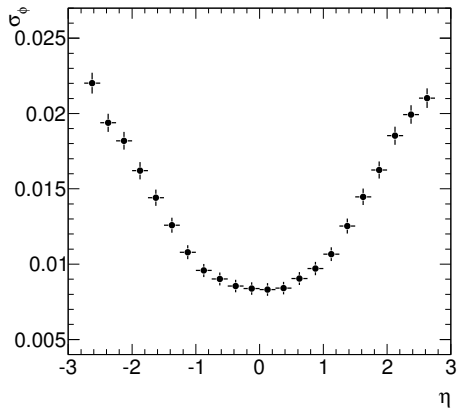

(d) ϕ

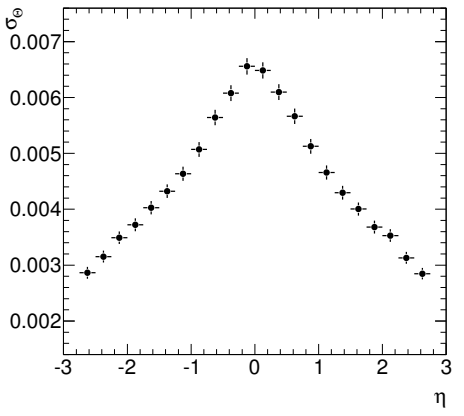

(e) θ

Figure 5.1: Resolutions of the track parameters versus η for the minimum bias event sample, integrated over $p_T > 0.15$ GeV/c. TRT stand-alone tracks have been excluded. Resolutions are calculated over a range which includes 99.7% of the data (corresponding to $\pm 3\sigma$).

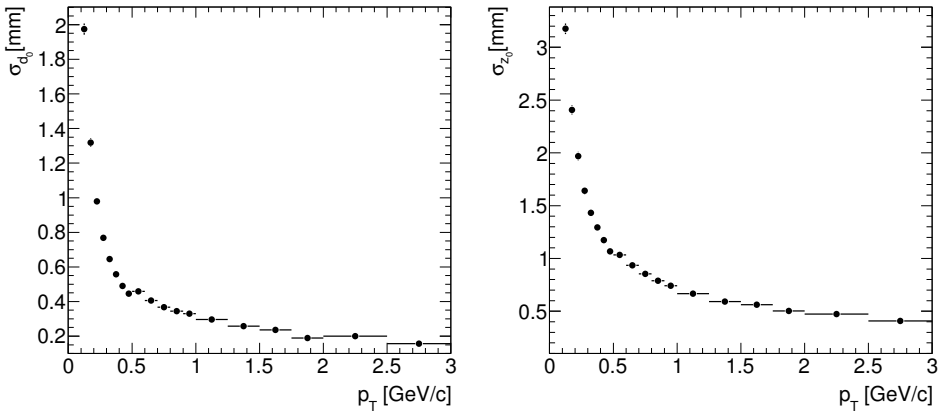

(a) d_0

(b) z_0

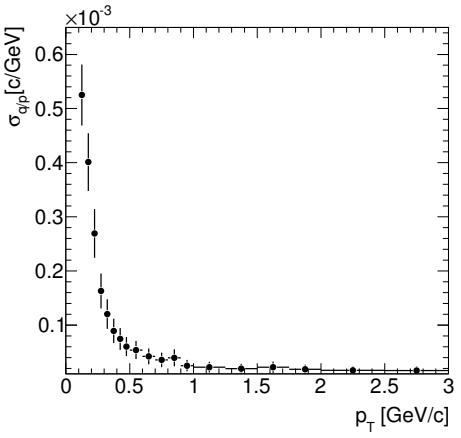

(c) q/p

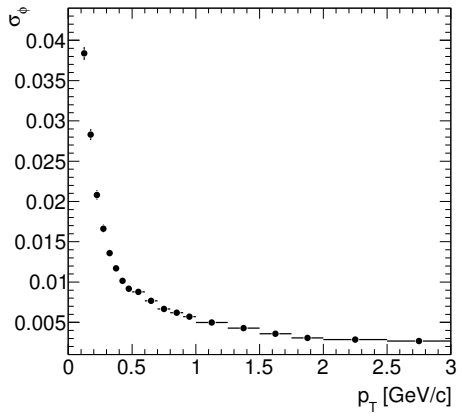

(d) ϕ

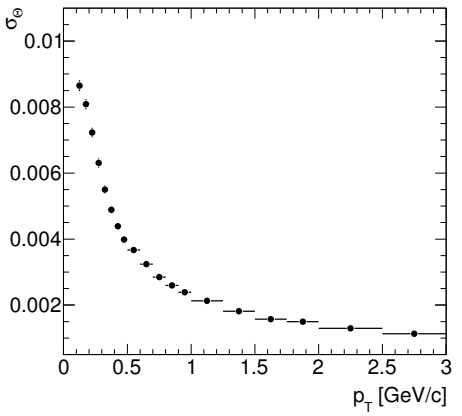

(e) θ

Figure 5.2: Resolutions of the track parameters versus p_T for the minimum bias event sample, integrated over $|\eta| < 2.5$. TRT stand-alone tracks have been excluded. Resolutions are calculated over a range which includes 99.7% of the data (corresponding to $\pm 3\sigma$).

5.1.1 Impact parameter resolutions

The transverse (d_0) and longitudinal (z_0) impact parameter resolutions are important requisites for vertexing and track selection. Hadronic interactions with the detector material add significant tails to the impact parameter resolutions, especially the z_0 resolution. This effect is more pronounced at higher $|\eta|$ values, since it is enhanced by the back propagation to the nominal vertex position [79]. The strong spread at higher $|\eta|$ is also coincident with the end-cap structures and services of the silicon detectors.

5.1.2 Angular and momentum resolutions

The angular (ϕ and θ) resolutions are important for vertex reconstruction and mass measurements. There is a strong correlation between these resolutions and the impact parameter resolutions for helical trajectories in a solenoidal field [79]. Thus the two sets of resolutions have very similar behaviors. The momentum (q/p) resolution is important for any kinematic analysis.

5.2 Track Parameter Pulls

Another way to measure the reliability of the track fit is to study the *pull* distributions of the track parameters. The pull is defined as the difference between the reconstructed and the true track parameter, divided by the estimated error on the reconstructed parameter:

$$\text{pull}(\tau) \quad = \quad \frac{\tau^{\text{rec}} - \tau^{\text{true}}}{\sigma_\tau} \tag{5.2}$$

for a track parameter τ. The pull distributions measure not only the accuracy of the track parameter estimation, but also the track parameter errors, taken from the diagonal elements in the track covariance matrix. If σ_τ is estimated correctly, then the pull values should give a Gaussian distribution with zero mean and width approximately equal to one. Thus, the pulls are an important quality and consistency check of the reconstruction.

Figure 5.3 shows the pull distributions of the five track parameters at the origin for the minimum bias event sample. With the exception of q/p, all track parameters have Gaussian pull distributions with a width close to one, indicating that the errors are correctly estimated. The long tails in the distributions are mostly due to low-p_T tracks, since the reconstruction is not tuned perfectly for these tracks.

The width of the q/p pull distribution shows a considerable deviation from the value of one. This effect is less pronounced in silicon-only tracks, indicating that this is related either to cluster error assignments in the TRT, or caused by different propagation precision in simulation and reconstruction [79]. The pulls of q/p and d_0 are slightly offset from zero. This could also be explained by a difference in the track extrapolation in simulation versus reconstruction, or by systematic shifts of the hit positions in the reconstruction [79].

Despite these deviations, the pull distributions in Figure 5.3 show that NewT incorporates a good error description for the track parameters in the perigee representation. They also show that the material in the detector geometry appears to be understood to within a few percent in the track fit.

5.3 Primary and Secondary Tracks

The complete set of reconstructed tracks contains tracks coming from *primary particles* produced in the *pp* collision, as well as *secondary particles* produced in secondary electromagnetic or hadronic interactions in the detector material. Primary particles include products of strong and electromagnetic decays, but exclude products from strange weak decays.

In the simulation, the primary particles are the final state particles created by the Pythia and Phojet event generators. These primary particles are then propagated and decayed by the Geant detector simulation, which produces the secondary particles. In Pythia, any particles with $c\tau > 10$ mm are not decayed but passed on to the detector simulation.

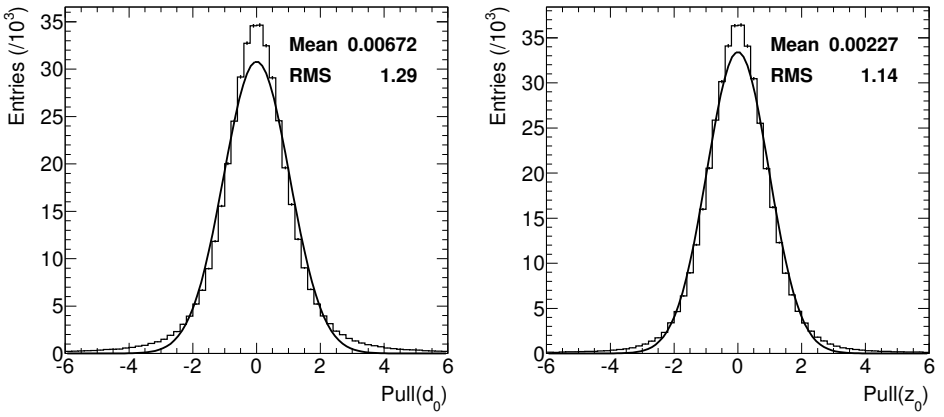

(a) d_0 (b) z_0

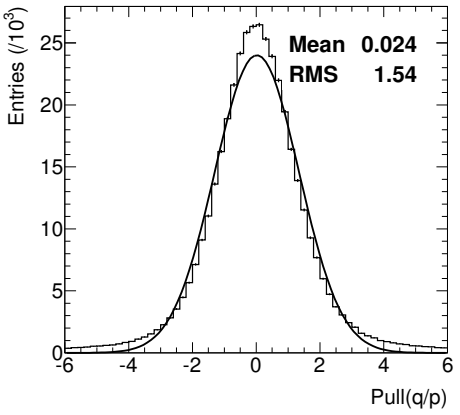

(c) q/p

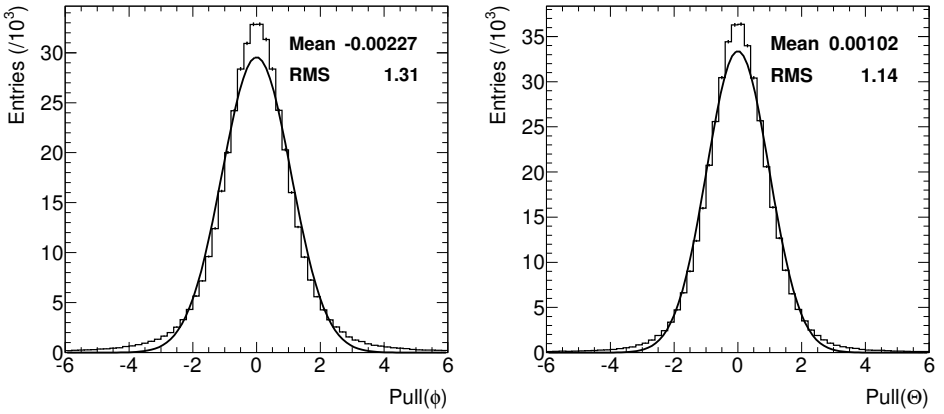

(d) ϕ (e) θ

Figure 5.3: Pull distributions of the track parameters at the origin for reconstructed tracks with $|\eta| < 2.5$ and $p_T > 0.15$ GeV/c in the minimum bias event sample. TRT stand-alone tracks have been excluded. Distributions have been fit with a single Gaussian.

The distinction between primary and secondary particles is important since the goal of the analysis is to reconstruct the $\mathrm{d}N_{\mathrm{ch}}/\mathrm{d}\eta$ and $\mathrm{d}N_{\mathrm{ch}}/\mathrm{d}p_T$ distributions of primary particles only. Tracks associated with secondary particles are, therefore, a background to the measurement. These tracks are partially removed using a set of track selection criteria defined in Section 5.6.

5.4 Truth Probability

During the track-truth association (see Section 4.7.2), a many-to-one map is created relating a reconstructed track to all possible matching truth trajectories with at least one common hit. This mapping contains data about the number of common hits between a track and a truth trajectory in any of the tracking detectors. A best match is then selected according to a quality of the match characteristic, called the *truth probability*, defined as

$$\text{truth probability} \quad = \quad \frac{\sum_i w_i C_i}{\sum_i w_i T_i}, \tag{5.3}$$

where C_i is the number of hits common between a track and a truth trajectory, T_i is the number of hits on track and w_i is the weight assigned to a sub-detector i. The sum is evaluated over all sub-detectors $i = \{ \text{PIX}, \text{SCT}, \text{TRT} \}$. The weights w_i are intended to compensate for the fewer number of precision hits in the silicon detectors. The default values used in the reconstruction are $w_{\mathrm{PIX}} = 5$, $w_{\mathrm{SCT}} = 3$ and $w_{\mathrm{TRT}} = 1$, but can be customized. More details on truth matching can be found in [93].

Figure 5.4 shows the truth probability for the set of all reconstructed tracks, sub-divided into tracks associated with primary particles and tracks associated with secondary particles. The truth probability can also be used to separate well-matched tracks from poorly-matched ones. In this chapter, a track is considered well-matched to a truth trajectory if its truth probability is $\geq 50\%$, i.e. if at least 50% of the hits contributing to the track fit (omitting outliers) correspond to one particle trajectory. Furthermore, the complete set of reconstructed tracks can be sub-divided into three groups:

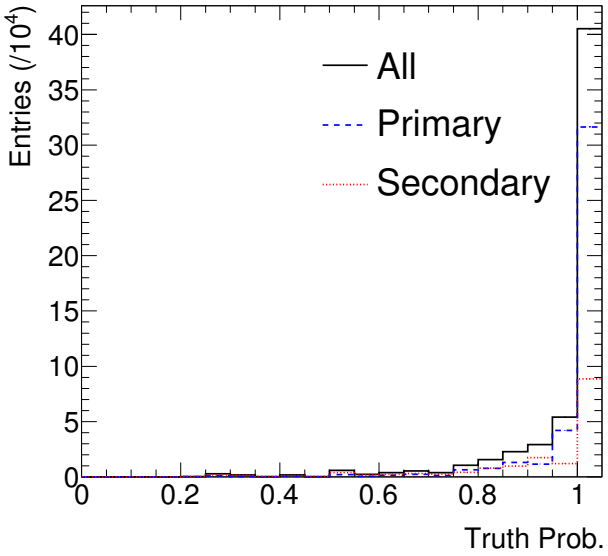

Figure 5.4: Truth probability (Equation 5.3) of reconstructed tracks in the minimum bias event sample. Tracks associated to primary particles (blue dashed line) and secondary particles (red dotted line) are shown separately.

A: tracks well matched to primary particles (truth probability $\geq 50\%$);

B: tracks well matched to secondary particles (truth probability $\geq 50\%$); and

C: tracks poorly matched to primary or secondary particles (truth probability $< 50\%$).

Since the cuts on the truth probability are inclusive, each reconstructed track must belong to one and only one of these groups. Tracks belonging to group A are labeled *primary tracks*, while tracks in group B are labled *secondary tracks*. Tracks in group C (either primary or secondary) are labeled *fake tracks* (see Section 5.7.2).

The value of 50% has been chosen for simplicity and should be varied to understand the effect on the number of tracks in each group. Figure 5.4, however, shows that the number of tracks with truth probability around 50% is extremely small. The associated systematic uncertainty is discussed in Section 7.8.

5.5 Reconstruction Efficiency

The definition of reconstruction efficiency is often a controversial subject since it relies not only on the definition of the signal of interest, but also on what is regarded as successfully reconstructed [79]. In addition, it is not always possible to separate detector effects from the pure software performance. Therefore, the definition of reconstruction efficiency is likely to vary among different physics analyses and performance studies.

The signal cuts defined here have been specifically designed for the minimum bias analysis. Reconstructed tracks have been matched to generated particles not by identifiers, but by the (highest) hit-matching truth probability (see Section 5.4). The efficiency defined here should be thought of as a *physics* reconstruction efficiency, since it incorporates inefficiencies due to both the tracking algorithms and particle interactions in the detector material. An attempt to identify the various effects contributing to the overall track reconstruction efficiency is made in Section 6.4 and 7.1.

5.5.1 Generator-level cuts

A simple set of cuts is applied to generated particles in order to define a clean signal sample characterized by primary charged particles within the geometrical acceptance of the Inner Detector [79]. These generator-level cuts are listed in Table 5.1. The cuts define the set of generated particles which should have been recorded by the detector and reconstructed by the tracking algorithms for the purpose of this analysis. An identifier number, or *barcode*, is used to restrict the signal to primary particles. Particles generated by PYTHIA have barcodes less than 100000, while particles produced by the GEANT simulation have barcodes greater than 100000.

Selection	**Cut**
Charged tracks	$\|q\| > 0$
Inner Detector acceptance	$\|\eta\| < 2.5$
Primary ('prompt') tracks	barcode < 100000

Table 5.1: Generator-level cuts used in the analysis. The cuts are intended to select primary charged particles within the geometrical acceptance of the Inner Detector.

5.5.2 Efficiency definition

A generated particle is considered *found*, or successfully reconstructed, if its truth probability (see Equation 5.3) is $\geq 50\%$. The primary track reconstruction efficiency ϵ can then be defined as

$$\epsilon \quad = \quad \frac{N^{\text{gen}}_{\text{found}}}{N^{\text{gen}}}, \tag{5.4}$$

where N^{gen} is the number of generated particles within the generator cuts and $N^{\text{gen}}_{\text{found}}$ is the number of found generated particles within the generator cuts. Since the same truth probability range was used to define well-matched tracks (see Section 5.4), $N^{\text{gen}}_{\text{found}}$ can also be thought of as the number of reconstructed tracks whose dominant source of hits come from a single truth trajectory within the generator cuts.

Figure 5.5 shows the reconstruction efficiency ϵ for NewT as a function of η and p_T. The overall track reconstruction efficiency is quite uniform along the central pseudorapidity range and falls off near the limit of the TRT acceptance ($|\eta| = 2.1$). The small drop in efficiency around $|\eta| = 1$ is due to the gap at the barrel/end-cap transition of the TRT.

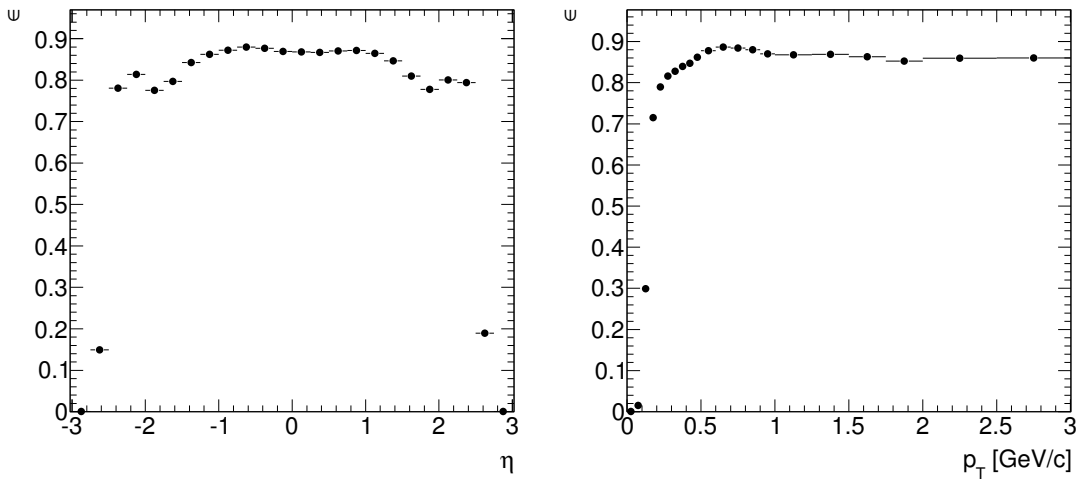

(a) (b)

Figure 5.5: Efficiency (ϵ) of reconstructing primary charged tracks in the minimum bias event sample, as a function of η (a) and p_T (b). The η plot is integrated over $p_T > 0.15$ GeV/c and the p_T plot is integrated over $|\eta| < 2.5$.

It is important to reiterate that ϵ is a *physics* reconstruction efficiency since it includes inefficiencies due to interactions in the detector material that reduce the findability of the generated particles. This definition is strongly dependent on the particle type, since each type interacts differently with the detector material. Muons and other minimum ionizing particles typically yield the highest reconstruction efficiencies, close to 100% over the entire acceptance region of the ID [79]. Pions and other hadronic particles are degraded by nuclear interactions with the detector material and show lower reconstruction efficiencies. Electrons suffer strongly from radiation loss and lead to the lowest reconstruction probability for a large part of the momentum range [79].

5.5.3 Migration

Errors in the measurement of η and p_T can cause reconstructed tracks to move, or 'migrate', into neighboring bins. To keep track of this, the migration M is defined as

$$M = \frac{N_{\text{pri}}^{\text{rec}}}{N_{\text{found}}^{\text{gen}}}, \tag{5.5}$$

where $N_{\text{found}}^{\text{gen}}$ is the number of found generated particles within the generator cuts (as above) and $N_{\text{pri}}^{\text{rec}}$ is the number of reconstructed tracks well-matched to a generated particle within the generator cuts. Figure 5.6 shows the migration M for NEWT as a function of η and p_T.

A value of $M \neq 1$ means that a fraction of tracks have been reconstructed such that their measured η (p_T) and their true η (p_T) belong to different η (p_T) bins. As the η and p_T measurement errors go to zero, the migration M will approach unity. The migration is also a function of the binning used in the analysis. For larger bin sizes, the absolute value of the migration in each bin will decrease. The migration is thus a good way of determining if the η and p_T binning is too small, given the resolution. Histogram binning is discussed in more detail in Section 6.3.

It is important to note that the definition of M depends on both reconstructed tracks (in the numerator) and generated particles (in the denominator). A proper definition of the migration should therefore not contain any track cuts (i.e. quality cuts) that could cause a discrepancy between

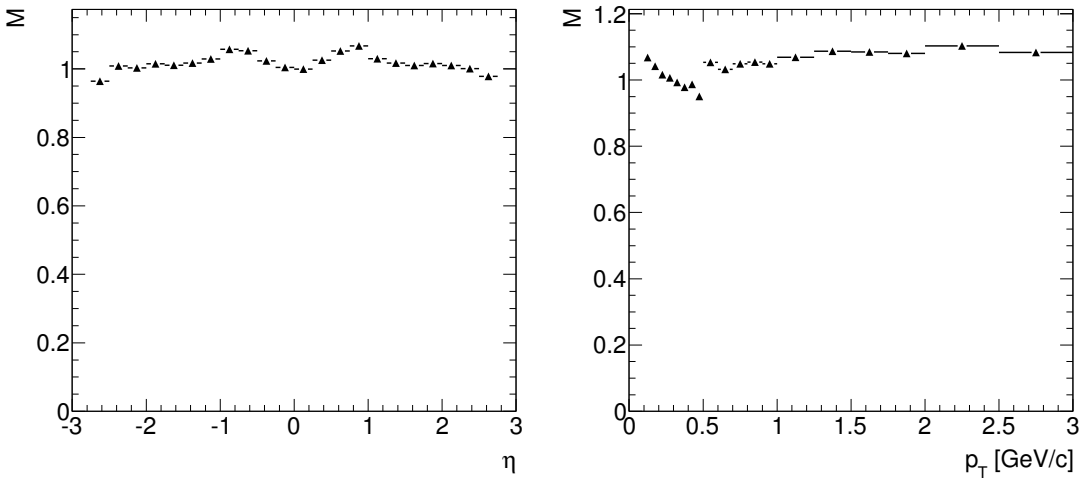

(a) (b)

Figure 5.6: Migration (M) of reconstructed primary tracks in the minimum bias event sample as a function of η (a) and p_T (b). The η plot is integrated over $p_T > 0.15$ GeV/c and the p_T plot is integrated over $|\eta| < 2.5$.

the number of tracks and the number of particles. As a consistency check, the numerator and denominator of the migration should be equal when integrated over all η or p_T bins.

5.6 Track Selection

A set of cuts is applied on reconstructed tracks in order to reduce the set of all tracks as close as possible to the set of primary generated particles mentioned above. The track-level cuts are listed in Table 5.2. Note that only measured track parameters are used for the track selection.

η, p_T acceptance	$\|\eta\| < 2.5$ $p_T > 0.15$ GeV/c
Quality cuts	No. of b-layer hits ≥ 1 No. of Si hits ≥ 5
Track-to-vertex cut	$\rho < 4.0$

Table 5.2: Track-level cuts used in the analysis. The cuts are intended to select reconstructed tracks associated to primary generated particles within the geometrical acceptance of the Inner Detector.

5.6.1 Quality cuts

The requirement of a b-layer hit removes a considerable portion of fake tracks, as well as tracks associated to secondary particles, since neither frequently leave a hit in the b layer of the pixel detector. The cut on the number of silicon hits is intended to remove TRT stand-alone tracks, which originate in the back-tracking but are not linked to silicon tracks (see Section 4.4.3). The minimum silicon-hit requirement is a default track scoring cut applied to all silicon tracks during reconstruction. While it is true that all tracks with a b-layer hit will therefore have at least five silicon hits, the cuts are intended to reinforce one another in case of any holes in the as-built detector.

Typically, the most widely-used information about the fit quality of tracks is the χ^2 value, together with the number of degrees of freedom n_{dof}. Although the χ^2/n_{dof} is a good parameter for a quick separation of good and bad tracks, it does not help in identifying fake tracks, solving hit ambiguities or evaluating track extensions [76]. It is typically only used during various stages of the track reconstruction. A cut on the probability of the track fit $P(\chi^2; n_{\mathrm{dof}})$ cannot be used with NewT since the probability function returns values less than 0.1 for 27% of the reconstructed tracks.

5.6.2 Track-to-vertex cut

The track-to-vertex cut is the selection that most effectively removes tracks associated to secondary particles while accepting tracks associated to primary particles. It is made by first extrapolating the track perigee to the global position of the reconstructed primary event vertex and calculating the transverse and longitudinal impact parameters with respect to the vertex. The normalized track-to-vertex distance ρ is then calculated as:

$$\rho = \sqrt{\left(\frac{d_0^{\mathrm{PV}}}{\sigma_{d_0^{\mathrm{PV}}}}\right)^2 + \left(\frac{z_0^{\mathrm{PV}}}{\sigma_{z_0^{\mathrm{PV}}}}\right)^2}, \tag{5.6}$$

where d_0^{PV} and z_0^{PV} are the transverse and longitudinal impact parameters calculated with respect to the primary vertex and $\sigma_{d_0^{\mathrm{PV}}}$ and $\sigma_{z_0^{\mathrm{PV}}}$ are the corresponding errors. The transverse and longitudinal

distances are normalized by their errors to avoid p_T dependence in the track selection. This has been verified in the simulation by comparing the ρ distributions for tracks in different p_T ranges.

Figure 5.7 shows the normalized track-to-vertex distances in the transverse versus the longitudinal direction, for the minimum bias event sample. Figure 5.8 shows the normalized track-to-vertex distance ρ for tracks originating from primary and secondary particles. Note that at $\rho = 4.0$, the number of tracks originating from primary particles is approximately equal to the number of tracks from secondary particles. The cut has been placed here as a balance between purity and efficiency, while minimizing systematic uncertainties coming from a mis-estimate of the track-to-vertex resolution (see Section 7.6).

5.6.3 Influence of track-level cuts

Figure 5.9 shows the influence of the track-level cuts on the minimum bias event sample. The first and last bins indicate the total number of tracks and the number of tracks that did not pass the track selection. The remaining bins show the number of tracks that did not pass each of the specified cuts. The 'Quality' bin indicates the number of tracks that failed either of the quality cuts in Table 5.2. Note that a single track can fail several cuts and therefore give counts in multiple bins.

Table 5.3 summarizes the effect of each of the track-level cuts on primary and secondary tracks in the minimum bias event sample. The strongest and most effective cut is the track-to-vertex cut, which cuts away about 70% of the tracks coming from secondary particles, while preserving 94% of the tracks coming from primary particles. The last line in Table 5.3 ('Total') indicates the cumulative effect of combining all track-level cuts.

Simulated distributions of the parameters used for track selection should be compared to the corresponding distributions when analyzing real data (see Chapter 8). An incorrect estimate of resolutions or detector alignment could result in a distorted distribution of selection parameters and thus change the effect of the track selection. The systematic uncertainty associated to a mis-estimate of the track-to-vertex resolution is evaluated in Section 7.6.

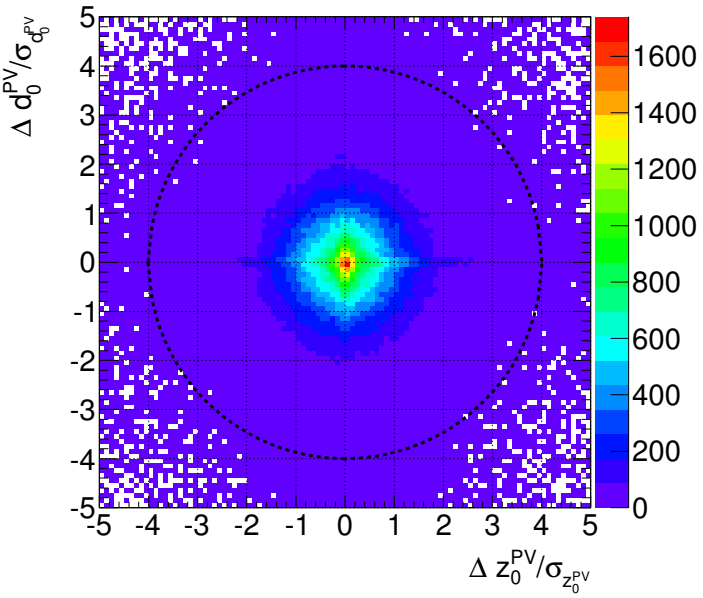

Figure 5.7: Normalized transverse ($d_0^{\mathrm{PV}}/\sigma_{d_0^{\mathrm{PV}}}$) and longitudinal ($z_0^{\mathrm{PV}}/\sigma_{z_0^{\mathrm{PV}}}$) impact parameters calculated with respect to the reconstructed primary event vertex, for the minimum bias event sample. The dotted circle indicates the boundary of the track-to-vertex cut.

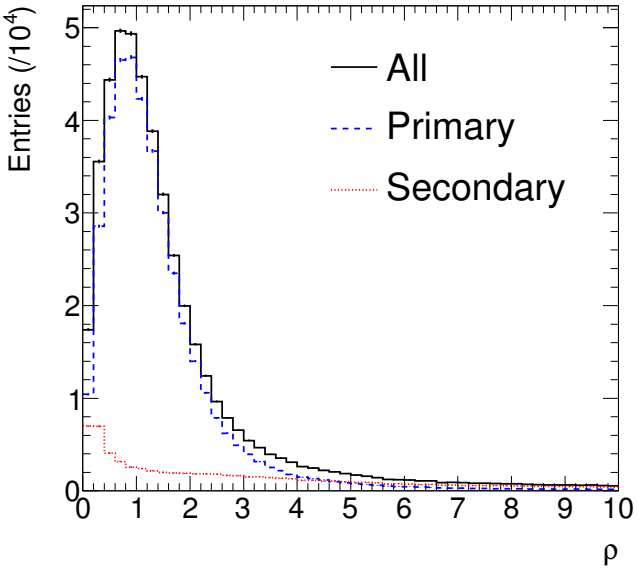

Figure 5.8: Normalized track-to-vertex distance (ρ) for tracks originating from primary and secondary particles. The track-to-vertex cut ($\rho < 4.0$) is placed where the number of primary and secondary tracks are approximately equal.

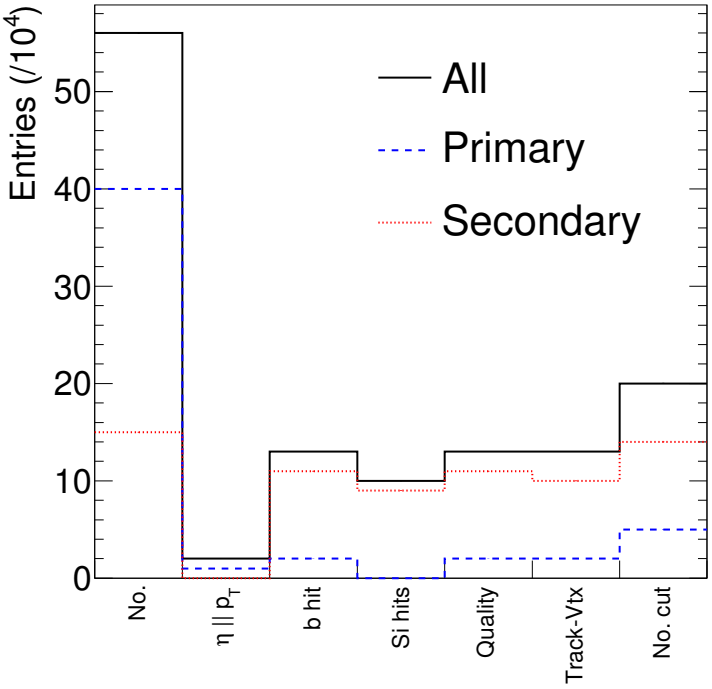

Figure 5.9: Influence of the different track-level cuts on the minimum bias event sample. The first and last bins indicate the total number of tracks and the number of tracks that did not pass the track selection. The remaining bins show the number of tracks that did not pass each of the specified cuts.

Selection	Cut Primaries (%)	Cut Secondaries (%)	Cut All (%)
η, p_T	4.6	3.4	4.3
b-layer hit	5.5	72.4	24.3
No. Si hits	2.2	59.0	18.1
Track-to-vertex	6.6	68.6	24.0
Total	**13.3**	**93.6**	**35.9**

Table 5.3: Influence of each of the track-level cuts on the minimum bias event sample. The 'Total' line indicates the cumulative effect of combining all track-level cuts.

5.7 Effectiveness of the Track Selection

The track-level cuts are designed to remove secondary and fake (poorly-matched) tracks, while simultaneously preserving well-matched primary tracks. These two objectives can be studied independently in order to evaluate the effectiveness of the track selection.

5.7.1 Acceptance of primary tracks

The acceptance A is defined as the fraction of well-matched primary tracks that survive the track selection:

$$A = \frac{N^{\mathrm{rec}}_{\mathrm{sel,pri}}}{N^{\mathrm{rec}}_{\mathrm{pri}}}, \tag{5.7}$$

where $N^{\mathrm{rec}}_{\mathrm{pri}}$ is the number of reconstructed tracks well-matched to a generated particle within the generator cuts (as above) and $N^{\mathrm{rec}}_{\mathrm{sel,pri}}$ is the number of reconstructed tracks selected by the track-level cuts and well-matched to a generated particle within the generator cuts. The acceptance is thus a measure of how well the track-level cuts retain the desired signal. By broadening (loosening) the selection cuts, higher values of the acceptance can be achieved. However, the risk of contaminating the selected track sample with secondary or fake tracks also increases.

Figure 5.10 shows the acceptance A of the track-level cuts as a function of η and p_T. The discontinuity at $p_T = 0.5$ GeV/c is an artifact of the reconstruction due to the turn-on of the TRT stand-alone tracking (see Section 4.4.3). Although a large fraction of these tracks are associated to secondary particles, the remaining portion can still be well-matched to primary particles. The TRT stand-alone tracks do not survive the silicon-hit requirement, causing the dip seen here.

5.7.2 Secondary and fake rates

Like the acceptance, the secondary and fake rates are defined for a given set of track selection criteria. The secondary rate s measures the fraction of selected tracks that are associated with

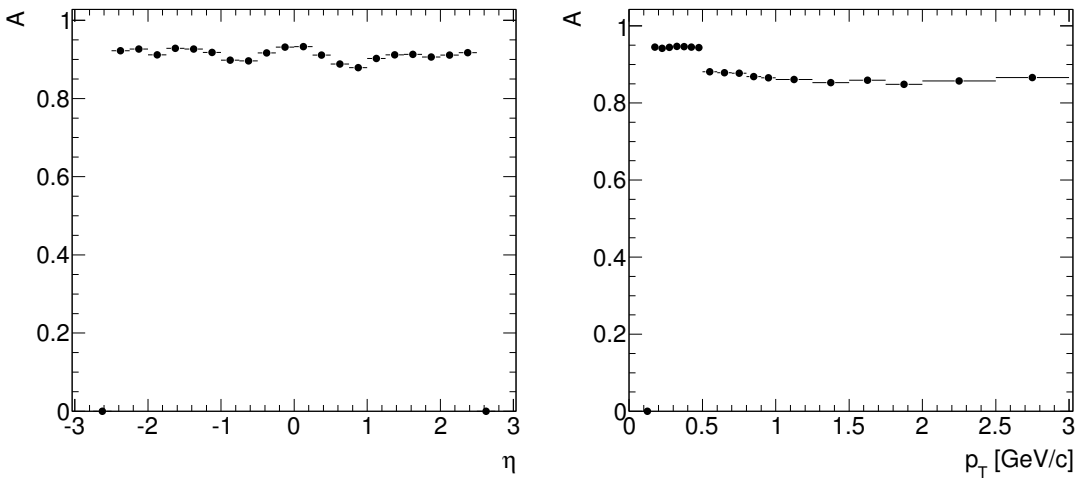

(a) (b)

Figure 5.10: Acceptance A of primary reconstructed tracks by the track selection in the minimum bias event sample, as a function of η (a) and p_T (b). The η plot is integrated over $p_T > 0.15$ GeV/c and the p_T plot is integrated over $|\eta| < 2.5$.

secondary particles, but that survive the track selection. It is defined as

$$s = \frac{N^{\mathrm{rec}}_{\mathrm{sel,sec}}}{N^{\mathrm{rec}}_{\mathrm{sel}}}, \tag{5.8}$$

where $N^{\mathrm{rec}}_{\mathrm{sel,sec}}$ is the number of reconstructed tracks selected by the track-level cuts and well-matched to a secondary particle and $N^{\mathrm{rec}}_{\mathrm{sel}}$ is the number of reconstructed tracks selected by the track-level cuts. The tracks in the numerator belong to group B, as defined in Section 5.4.

For the purpose of this analysis, any tracks that have passed the selection criteria, but are not well-matched to primary or secondary generated particles, are considered fake tracks. The majority of associated measurements in these tracks do not originate from one single particle. These tracks belong to group C, as defined in Section 5.4. The fake rate f is defined as

$$f = \frac{N^{\mathrm{rec}}_{\mathrm{sel,poor}}}{N^{\mathrm{rec}}_{\mathrm{sel}}}, \tag{5.9}$$

where $N^{\mathrm{rec}}_{\mathrm{sel,\ poor}}$ is the number of reconstructed tracks selected by the track-level cuts and poorly matched to any generated particle and $N^{\mathrm{rec}}_{\mathrm{sel}}$ is defined as above. Figure 5.11 shows the secondary rate s and fake rate f following the track selection as a function of η and p_T.

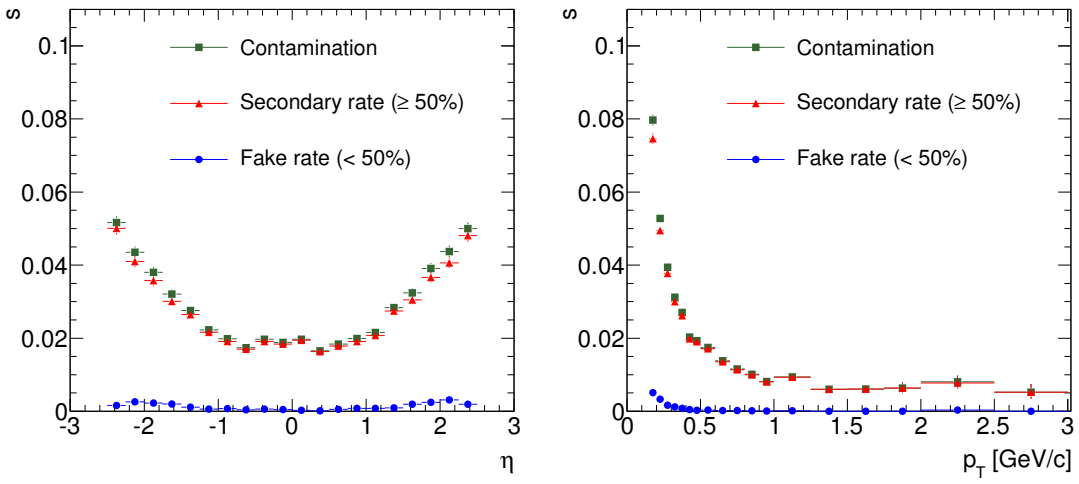

(a) (b)

Figure 5.11: Secondary rate (s) and fake rate (f) following the track selection in the minimum bias event sample, as a function of η (a) and p_T (b). The red triangles represent the fraction of selected tracks well-matched to secondary particles (truth probability $\geq 50\%$). The blue circles represent the fraction of selected tracks poorly matched to any generated particle (truth probability $< 50\%$). The contamination ζ is equal to the sum of the blue and red contributions, denoted here by green squares. The η plot is integrated over $p_T > 0.15$ GeV/c and the p_T plot is integrated over $|\eta| < 2.5$.

The contamination ζ of the selected track sample by secondary and fake tracks can be measured by summing Equations 5.8 and 5.9. ζ is thus the fraction of reconstructed tracks selected by the track-level cuts, but not well-matched to primary particles. Using the definitions from Section 5.4, ζ is the fraction of selected tracks in groups B and C. It can also be written in terms of the fraction of selected tracks in group A:

$$\zeta = s + f \tag{5.10}$$

$$= 1 - \frac{N^{\mathrm{rec}}_{\mathrm{sel,pri}}}{N^{\mathrm{rec}}_{\mathrm{sel}}}, \tag{5.11}$$

where $N^{\mathrm{rec}}_{\mathrm{sel,pri}}$ and $N^{\mathrm{rec}}_{\mathrm{sel}}$ are defined as above. Figure 5.11 also shows the contamination ζ of the track sample following the track selection as a function of η and p_T.

The analysis presented in the next chapter will use the generator-level and track-level cuts defined here.

Part III

Analysis

Chapter 6

Method

In this chapter, the minimum bias analysis is presented using the simulated inelastic event sample. The final $\mathrm{d}N_{\mathrm{ch}}/\mathrm{d}\eta$ and $\mathrm{d}N_{\mathrm{ch}}/\mathrm{d}p_T$ distributions are obtained by applying a set of corrections to the corresponding measured distributions. The set of corrections are determined by comparing Monte Carlo truth input to the output of the detector simulation and reconstruction. The analysis procedure is outlined in Section 6.1 and detailed in Section 6.7. The corrections are defined in Sections 6.4 and 6.5.

The analysis is then performed on the inelastic event sample by dividing the sample of 14,650 events in half. The first half, called the *correction sample*, is used to calculate the corrections. The second half, called the *analysis sample*, is used as input to the analysis. The final corrected distributions are presented in Section 6.8.

Details of the simulation and reconstruction of the inelastic event sample can be found in Appendix A. Events and tracks used in the analysis have been selected from the event sample according to the criteria given in Sections 3.8 and 5.6, respectively. The conceptual framework of the minimum bias analysis presented here has been inspired by [94].

6.1 General Procedure

The goal of the analysis is to measure the number of primary charged particles per unit of pseudorapidity (η) or per unit of transverse momentum (p_T) per inelastic interaction. Primary particles are defined as particles produced in the pp collision, including products of strong and electromagnetic decays, but excluding products from strange weak decays or particles produced in secondary electromagnetic or hadronic interactions in the detector material.

The $\mathrm{d}N_{\mathrm{ch}}/\mathrm{d}\eta$ and $\mathrm{d}N_{\mathrm{ch}}/\mathrm{d}p_T$ distributions are obtained by applying two corrections to the measured number of selected tracks in selected events. These corrections are:

- a track reconstruction correction; and
- a vertex reconstruction correction.

The first correction accounts for the difference between the number of selected tracks and the number of primary charged particles. The second correction accounts for the inefficiency of the vertex reconstruction and the bias imposed by the vertex requirements on the triggered event sample. The vertex cut is needed since track selection is undefined for events without a reconstructed primary vertex (see Section 5.6).

The track reconstruction correction is applied only at track level. The vertex reconstruction correction is applied at both track and event level. The track-level vertex correction is needed to compensate for any bias on the measured track distribution due to the vertex requirements. Both track-level corrections are determined as a function of η and p_T. The event-level vertex correction is determined as a function of the z-position of the reconstructed primary event vertex (abbreviated v_z henceforth) and the multiplicity (N), defined as the number of reconstructed tracks in the event.

Definitions of the track reconstruction and vertex reconstruction corrections are given in Sections 6.4 and 6.5. The detailed procedure for applying these corrections is given in Section 6.7.

6.2 Trigger Bias

A correction for the bias imposed by the minimum bias trigger used in the analysis is not applied since the correction would be entirely model-dependent. This is due to uncertainties in the predicted relative cross sections among the various inelastic components (non-diffractive, single-diffractive and double-diffractive), as well as uncertainties in the modeling of diffractive collisions (see Chapter 2). These factors lead to large uncertainties in the calculated trigger acceptances. Model dependency can thus be avoided by not correcting for the trigger bias.

The resulting corrected $\mathrm{d}N_{\mathrm{ch}}/\mathrm{d}\eta$ and $\mathrm{d}N_{\mathrm{ch}}/\mathrm{d}p_T$ distributions are therefore trigger-dependent. The bias on the track distributions due to the minimum bias trigger is shown in Figure 3.5 (page 59) as a function of η and p_T. The figure shows how the η and p_T distributions are distorted by the trigger. The bias on the event-level distributions (v_z, N) due to the trigger are not shown here, but can be found in [95]. It is important to remember that the acceptance of the trigger for the various inelastic physics processes influences the normalization of the corrected $\mathrm{d}N_{\mathrm{ch}}/\mathrm{d}\eta$ and $\mathrm{d}N_{\mathrm{ch}}/\mathrm{d}p_T$ distributions (see Section 2.6).

6.3 Histogram Binning

The corrections and reconstructed distributions are stored in histograms with variable bin sizes. The choice of bin size should take into account the resolution of the variable, as well as the obtained statistics, both in the simulation and in the analyzed data sample. The binning used in the analysis is as follows:

- the η bin width is 0.25 for all $|\eta| < 3.0$;
- the p_T bin width is 0.05 GeV/c for $p_T < 0.5$ GeV/c, where the corrections change rapidly, and increases steadily up to 0.5 GeV/c for $p_T > 2.0$ GeV/c, where statistics are low;
- the multiplicity bin width is 1 at low multiplicity ($N < 10$) and increases up to 50 for $N > 100$;

- the v_z bin width is 20 mm for $|z| < 100$ mm, 25 mm for $100 < |z| < 150$ mm and 50 mm for $|z| > 150$ mm.

This particular binning was chosen to properly resolve regions where the corrections change rapidly, while ensuring a statistical error of less than 2% in each bin.

6.4 Track Reconstruction Correction

As discussed in Chapter 5, the number of reconstructed tracks differs from the number of primary charged particles due to several effects: detector and reconstruction inefficiency (ϵ), migration of tracks into neighboring bins (M), acceptance of the track selection (A) and contamination from secondaries and fakes (ζ). The track reconstruction correction $C_{\rm trk}(\eta, p_T)$ takes all of these effects into account. It is calculated as

$$C_{\rm trk}(\eta, p_T) = \frac{(1-\zeta)}{A \cdot \epsilon \cdot M}, \tag{6.1}$$

where ϵ, M, A, and ζ are the efficiency, migration, acceptance and contamination, as previously defined in Equations 5.4, 5.5, 5.7 and 5.11, respectively. Figures 6.1 and 6.2 show the four components of the track reconstruction correction as a function of η and p_T, respectively. The individual components are discussed in more detail in Sections 5.5 and 5.7.

Substituting Equations 5.4, 5.5, 5.7 and 5.11 into Equation 6.1, the expression for $C_{\rm trk}(\eta, p_T)$ reduces to

$$C_{\rm trk}(\eta, p_T) = \frac{N^{\rm gen}}{N^{\rm rec}_{\rm sel}}, \tag{6.2}$$

where $N^{\rm gen}$ is the number of generated particles within the generator cuts given in Table 5.1 and $N^{\rm rec}_{\rm sel}$ is the number of reconstructed tracks selected by the track-level cuts given in Table 5.2. $N^{\rm gen}$ and $N^{\rm rec}_{\rm sel}$ have previously been defined in Sections 5.5.2 and 5.7.2, respectively.

Although Equations 6.1 and 6.2 give two equivalent expressions for $C_{\rm trk}(\eta, p_T)$, the correction is ultimately calculated using the latter. The numerator and denominator of Equation 6.2 are

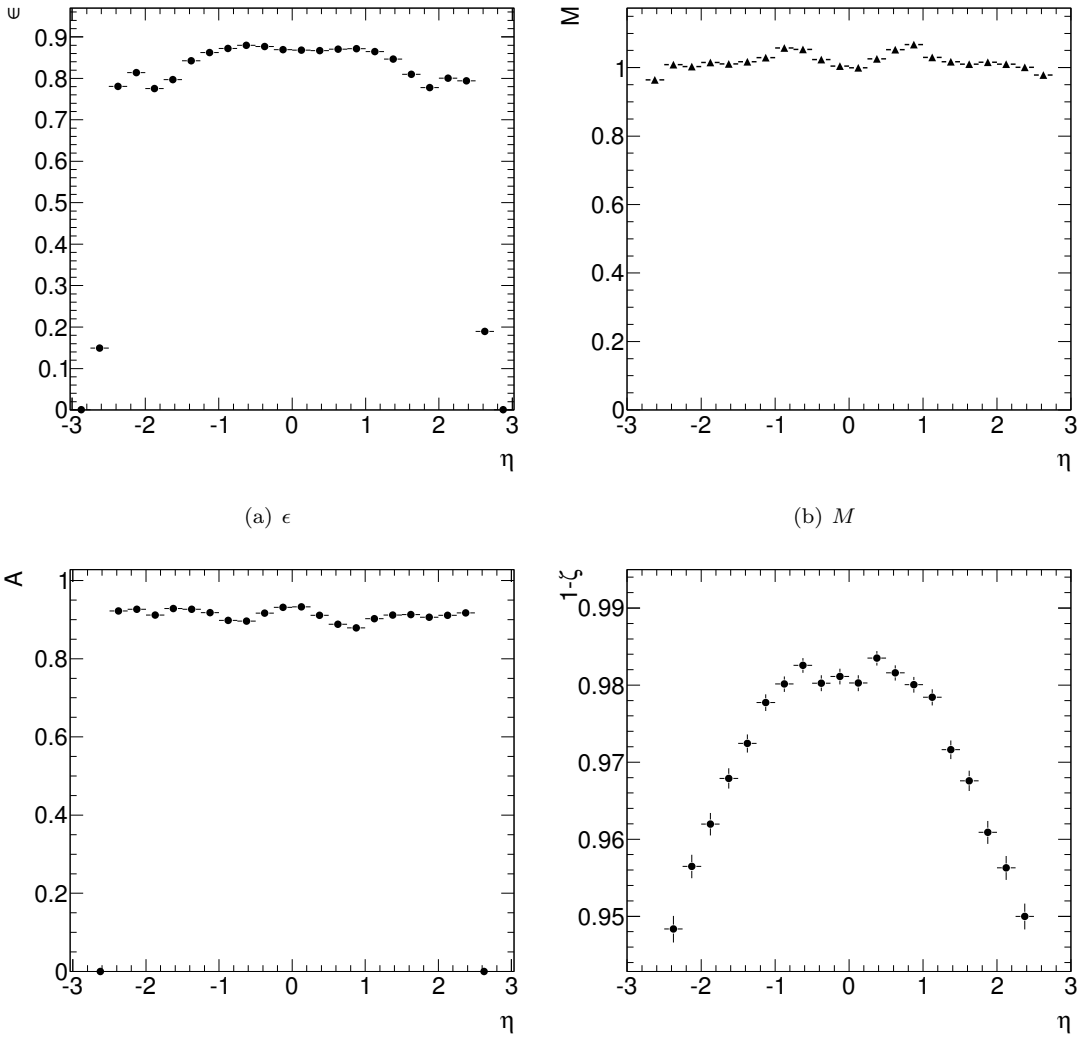

(a) ϵ

(b) M

(c) A

(d) $1-\zeta$

Figure 6.1: Components of the track reconstruction correction (ϵ, M, A and $1-\zeta$) for the minimum bias event sample as a function of η. Note that (d) is zero-suppressed. Plots are integrated over $p_T > 0.15$ GeV/c.

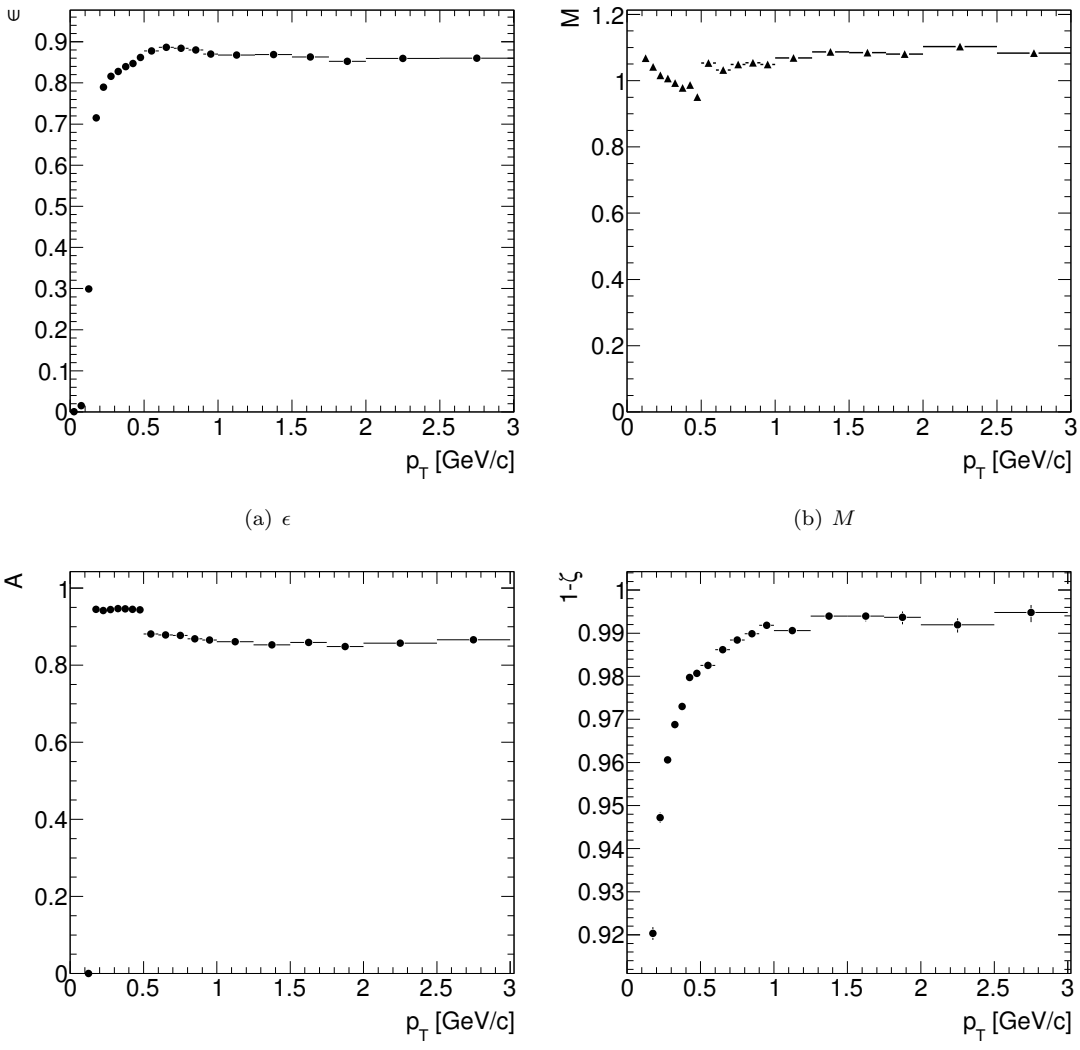

(a) ϵ

(b) M

(c) A

(d) $1-\zeta$

Figure 6.2: Components of the track reconstruction correction (ϵ, M, A and $1-\zeta$) for the minimum bias event sample as a function of p_T. Note that (d) is zero-suppressed. Plots are integrated over $|\eta| < 2.5$.

calculated for the same events taken through the full detector simulation and reconstruction. The event sample only includes those events that pass the event selection criteria listed in Section 3.8. Figure 6.3 shows the 2-dimensional track reconstruction correction $C_{\mathrm{trk}}(\eta, p_T)$ and its projections to the η and p_T axes. Note that the correction flattens out at high p_T, where material corrections and multiple scattering no longer play a significant role.

The track reconstruction correction depends on many variables: η, p_T, ϕ, particle species, charge (q), z-position of the reconstructed primary event vertex (v_z) and event multiplicity (N). In this analysis, the correction is determined as a function of η and p_T only and is integrated over the remaining variables. This integration can impose systematic errors if the simulation does not correspond to reality. In most cases, however, these effects are negligible.

Multiplicity dependence

Integration over multiplicity is justified since the occupancy of the detector in pp collisions is very low, even for high-multiplicity events, and saturation effects can be neglected. Note that this does not apply for heavy-ion measurements where saturation effects in the ID become significant. In this case, occupancy of the detector in the simulation should be checked with that found in data.

ϕ dependence

Integration over ϕ is reasonable since the collisions are on average axially symmetric. The as-built detector, however, may not be totally symmetric in ϕ. Figure 6.4 shows the track reconstruction correction as a function of ϕ. The correction is mostly uniform over the entire ϕ range, although there is some deviation for a few points at high $|\phi|$. This check should be repeated with the final detector description used for the measurement. If large asymmetries are observed, then the correction should additionally be calculated as a function of ϕ. However, more statistics are needed since the correction would then depend on three variables.

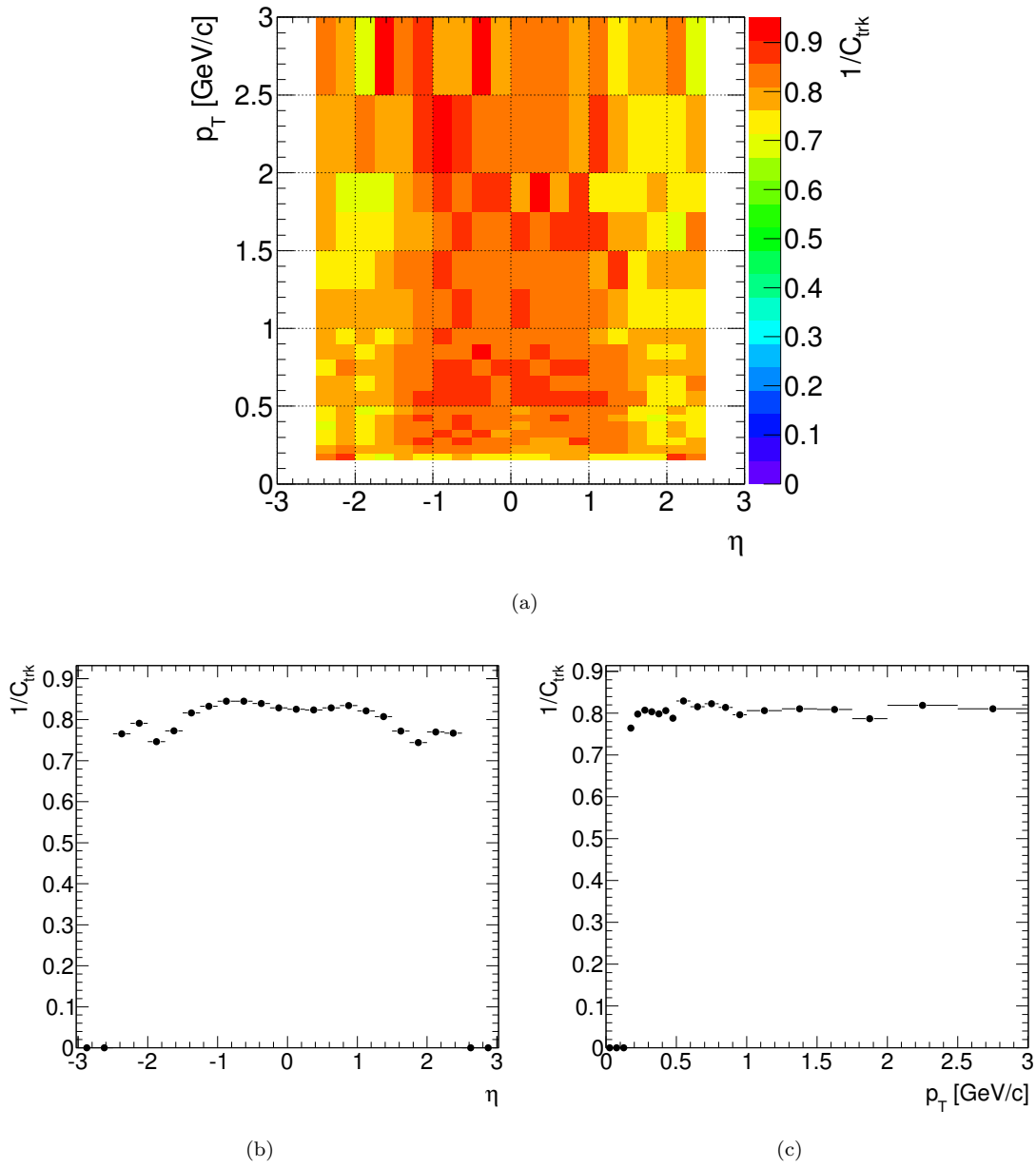

Figure 6.3: Track reconstruction correction (C_{trk}) as a function of η and p_T (a). Projections onto the η (b) and p_T (c) axes are also shown. The η plot is integrated over $p_T > 0.15$ GeV/c and the p_T plot is integrated over $|\eta| < 2.5$. Note that the correction is calculated and applied in two dimensions. Projections are shown here only for visibility.

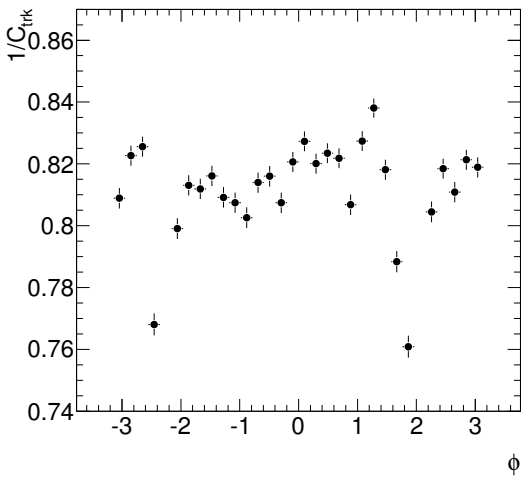

Figure 6.4: Track reconstruction correction (C_{trk}) as a function of ϕ. The correction is mostly uniform over the entire ϕ range. The plot is integrated over $p_T > 0.15$ GeV/c and $|\eta| < 2.5$.

Charge dependence

The integration over charge is reasonable since the corrections for negative and positive particles are identical over most of the corrected p_T range. Figure 6.5 shows the track reconstruction correction factor for positively and negatively charged particles, as a function of η and p_T. The corrections are identical over most of the corrected p_T range and differ only for $p_T < 0.2$ GeV/c.

Particle species dependence

Integration over particle species is not as easily justified since the track reconstruction correction differs significantly for each of the particle species at low p_T (see Section 5.5). Figure 6.6 shows the track reconstruction correction factor for different particle species, as a function of η and p_T. The figure shows that the correction for protons is significantly different for $p_T < 0.4$ GeV/c.

Making and applying independent corrections for each of the particle species, however, would require particle identification and is therefore not suitable for a (relatively) quick analysis using first data. Instead the default particle composition given by the event generator is used and the error associated to this uncertainty is taken as a systematic (see Section 7.1).

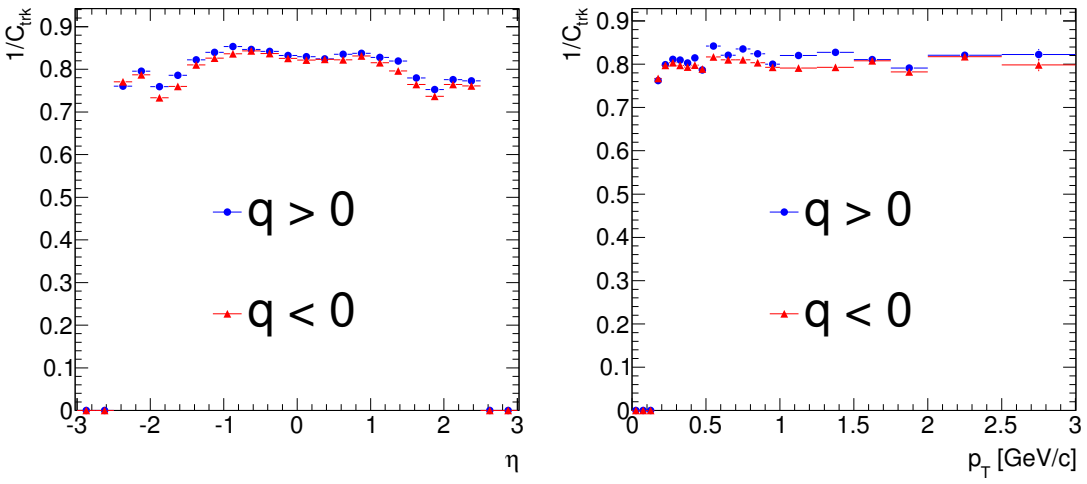

(a) (b)

Figure 6.5: Track reconstruction correction (C_{trk}) for positively charged ($q > 0$) and negatively charged ($q < 0$) particles, independently, as a function of η (a) and p_T (b). The corrections are identical over most of the corrected p_T range and differ only for $p_T < 0.2$ GeV/c. The η plot is integrated over $p_T > 0.15$ GeV/c and the p_T plot is integrated over $|\eta| < 2.5$.

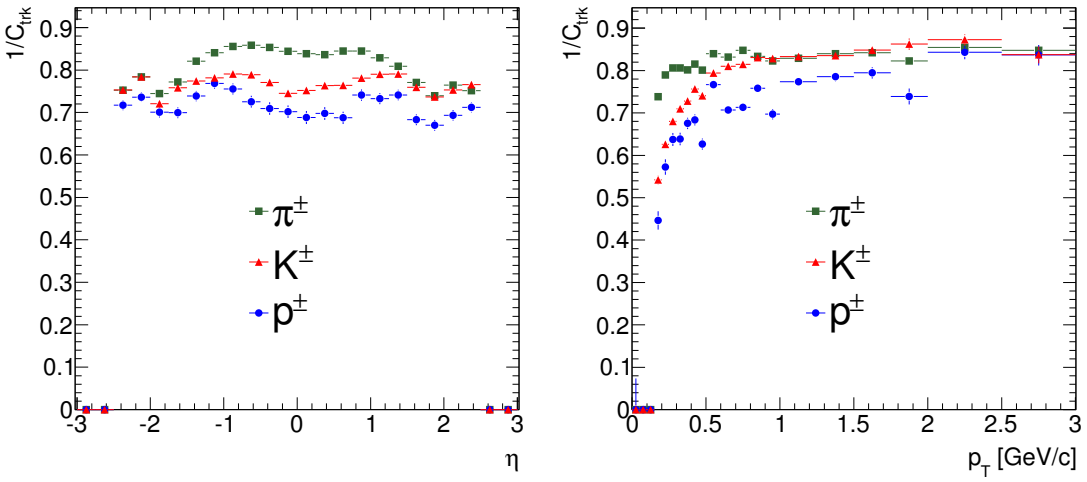

(a) (b)

Figure 6.6: Track reconstruction correction (C_{trk}) for pions ($\pi^{\pm}$), kaons ($K^{\pm}$) and protons ($p^{\pm}$), independently, as a function of η (a) and p_T (b). The correction for protons is significantly different for $p_T < 0.4$ GeV/c. The η plot is integrated over $p_T > 0.15$ GeV/c and the p_T plot is integrated over $|\eta| < 2.5$.

6.5 Vertex Reconstruction Correction

The vertex reconstruction correction takes into account the bias introduced by restricting the event sample to events with a single reconstructed primary vertex meeting the requirements defined in Section 3.8. Since the minimum bias event sample has been simulated with only one interaction per bunch crossing, this correction is essentially the inverse of the primary vertex reconstruction efficiency, after requiring the vertex to have at least two tracks associated to it.

The event-level correction $\tilde{C}_{\mathrm{vtx}}$ is calculated as a function of v_z and event multiplicity N:

$$\tilde{C}_{\mathrm{vtx}}(v_z, N) = \frac{\tilde{N}^{\mathrm{evt}}_{\mathrm{trig}}}{\tilde{N}^{\mathrm{evt}}_{\mathrm{trig,vtx}}}, \tag{6.3}$$

where $\tilde{N}^{\mathrm{evt}}_{\mathrm{trig}}$ is the number of triggered events and $\tilde{N}^{\mathrm{evt}}_{\mathrm{trig,vtx}}$ is the number of triggered events passing the vertex requirements given in Section 3.8. The event multiplicity N is defined as the total number of reconstructed tracks in the event. Alternatively, the number of clusters in the pixel detector could be used.

Figure 6.7 shows the event-level vertex reconstruction correction as a function of N and v_z. As the multiplicity increases, the correction approaches unity. For events with $N > 10$, a vertex is always found and the correction is not needed. Although Figure 6.7 only shows the region $0 < N < 25$, the correction is calculated up to $N = 200$.

A corresponding track-level correction is also needed to compensate for any bias on the measured track distribution due to the vertex requirements. The track-level vertex correction C_{vtx} is calculated as a function of η and p_T:

$$C_{\mathrm{vtx}}(\eta, p_T) = \frac{N^{\mathrm{rec}}_{\mathrm{trig}}}{N^{\mathrm{rec}}_{\mathrm{trig,vtx}}}, \tag{6.4}$$

where $N^{\mathrm{rec}}_{\mathrm{trig}}$ and $N^{\mathrm{rec}}_{\mathrm{trig,vtx}}$ are the total number of reconstructed tracks in $\tilde{N}^{\mathrm{evt}}_{\mathrm{trig}}$ and $\tilde{N}^{\mathrm{evt}}_{\mathrm{trig,vtx}}$, respectively. Note that the track-level cuts are not applied here since the track-to-vertex distance ρ (see Equation 5.6) is undefined for events with no reconstructed vertex. Instead, the total number of reconstructed tracks N in either of the event types is used to calculate C_{vtx}.

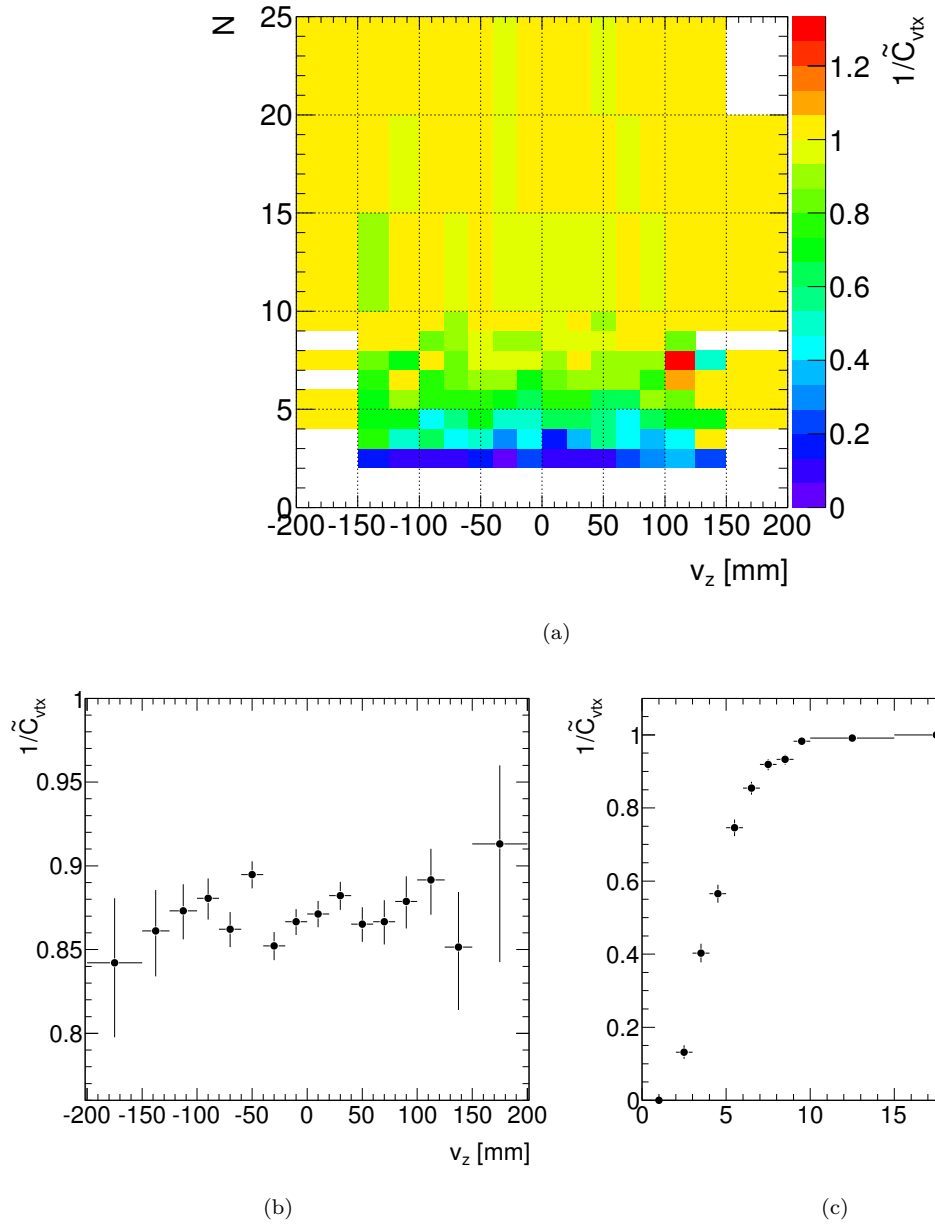

Figure 6.7: Event-level vertex correction ($\tilde{C}_{\text{vtx}}$) as a function of v_z and N (a). Projections onto the v_z (b) and N (c) axes are also shown. N is defined as the number of reconstructed tracks in the event. The v_z and N plots are integrated over all values of N and v_z, respectively. Note that the correction is calculated and applied in two dimensions. Projections are shown here only for visibility.

Figure 6.8 shows the track-level vertex reconstruction correction as a function of η and p_T. Although the correction is close to unity for all values of η and p_T, the figure shows that some non-zero bias against tracks with low p_T or high $|\eta|$ is introduced by the vertex requirements.

Although the vertex reconstruction correction is essentially a detector correction, some model dependence is present since only triggered events are taken into account when computing the correction. Using only triggered events, however, has the advantage that the correction can be calculated directly from data, without relying on simulation. Once data is available, the properties of triggered events outside of the vertex requirements can be compared to corresponding events in the simulation. This will help build confidence in the correction, while minimizing any systematic uncertainties.

6.6 p_T-cutoff Correction

The efficiency of reconstructing tracks with very low p_T is poor due to their large curvature in the magnetic field and significant degree of multiple scattering (see Sections 4.4.2 and 5.5). The p_T cut used in the analysis is therefore 0.15 GeV/c, corresponding to tracks that traverse the silicon detectors and allowing for sufficiently good reconstruction.

A measurement of $\mathrm{d}N_{\mathrm{ch}}/\mathrm{d}\eta$, however, requires integrating over all p_T, including the low-p_T region that is missing. A 'p_T-cutoff' correction can be calculated by either:

(a) using the event generator to estimate the number of primary particles below the p_T cutoff as a function of η; or

(b) fitting the corrected p_T spectrum down to the p_T cutoff and using the fit to extrapolate down to $p_T = 0$.

Method (a) is severely dependent on the model used by the Monte Carlo event generator and would introduce large systematic errors due to uncertainties of the generator in the low-p_T domain. Method (b) is also flawed since any parameterization of the p_T spectrum would be *ad hoc* and not theoretically guided. Past experiments [51, 96] have used empirical fits to do such an extrapolation.

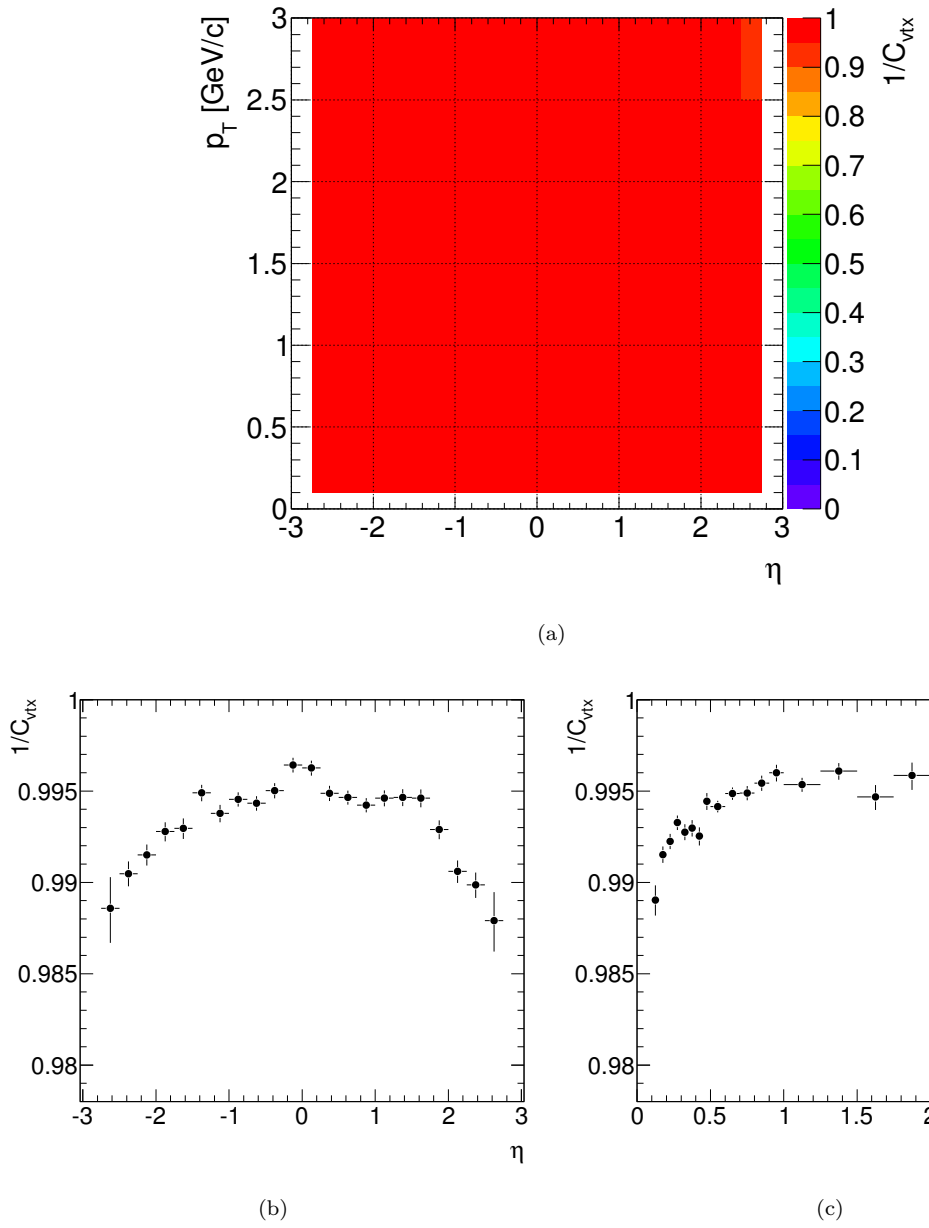

(a)

(b)

(c)

Figure 6.8: Track-level vertex correction (C_{vtx}) as a function of η and p_T (a). Projections onto the η (b) and p_T (c) axes are also shown. The η plot is integrated over $p_T > 0.15$ GeV/c and the p_T plot is integrated over $|\eta| < 2.5$. Note that the correction is calculated and applied in two dimensions. Projections are shown here only for visibility.

Although method (b) would allow comparing LHC data to results from past experiments, it is more experimentally sound to quote the $\mathrm{d}N_{\mathrm{ch}}/\mathrm{d}\eta$ measurement down to the p_T cutoff. Afterwards the event generator can be tuned to agree with this measurement and used to extrapolate back to $p_T = 0$.

6.7 Applying the Corrections

In this section, the procedure used to obtain the final $\mathrm{d}N_{\mathrm{ch}}/\mathrm{d}\eta$ and $\mathrm{d}N_{\mathrm{ch}}/\mathrm{d}p_T$ distributions from the measured data is given in detail. An η-p_T (2-D) histogram is filled with the selected tracks (in selected events), weighted by the values of the track reconstruction correction and the track-level vertex reconstruction correction defined in Sections 6.4 and 6.5, respectively. A v_z-N (2-D) histogram is filled with the selected events, weighted by the value of the event-level vertex reconstruction correction defined in Section 6.5. The event-level histogram is needed to provide the proper normalization factor for the analysis.

After filling the histograms, a vertex range is chosen and the v_z variable is integrated out. In the case of $\mathrm{d}N_{\mathrm{ch}}/\mathrm{d}\eta$, the p_T variable is integrated over $p_T > 0.15$ GeV/c. In the case of $\mathrm{d}N_{\mathrm{ch}}/\mathrm{d}p_T$, the η variable is integrated over $|\eta| < 2.5$. The total number of events N_{ev} is calculated by integrating the weighted event-level histogram over all values of N and v_z. Each η-bin or p_T-bin is then divided by N_{ev} and the bin width.

This procedure can be expressed mathematically in the following way. For a given η-p_T bin, corresponding to a certain region of phase space, let P represent the number of particles and I represent the number of interactions. Then:

$$P(\eta, p_T) = \sum_{\text{events}} \sum_{\text{tracks}} [C_{\mathrm{trk}}(\eta, p_T) \cdot C_{\mathrm{vtx}}(\eta, p_T)] \tag{6.5}$$

$$I(v_z, N) = \sum_{\text{events}} \tilde{C}_{\mathrm{vtx}}(v_z, N) \tag{6.6}$$

The sums are over all selected events and selected tracks. Selected tracks are weighted by the track reconstruction correction (C_{trk}) and by the track-level vertex correction (C_{vtx}). Selected events are

weighted by the event-level vertex correction ($\tilde{C}_{\rm vtx}$). $\mathrm{d}N_{\rm ch}/\mathrm{d}\eta$ and $\mathrm{d}N_{\rm ch}/\mathrm{d}p_T$ are then calculated for a given vertex range $[V_1, V_2]$ as:

$$\left.\frac{\mathrm{d}N_{\rm ch}}{\mathrm{d}\eta}\right|_{\eta=\eta'} = \frac{\int P(\eta', p_T)\mathrm{d}p_T}{\int_{V_1}^{V_2}\int I(v_z, N)\mathrm{d}N\mathrm{d}v_z} \tag{6.7}$$

$$\left.\frac{\mathrm{d}N_{\rm ch}}{\mathrm{d}p_T}\right|_{p_T=p_T'} = \frac{\int P(\eta, p_T')\mathrm{d}\eta}{\int_{V_1}^{V_2}\int I(v_z, N)\mathrm{d}N\mathrm{d}v_z} \tag{6.8}$$

Note that the effect of the p_T cutoff is not corrected in the analysis (see Section 6.6).

6.8 Corrected Distributions

The procedure described in the previous section was performed on a mock 'data' sample to exercise and validate the analysis. The minimum bias event sample was divided into two parts: a *correction sample* and an *analysis sample*. The first was used to calculate the corrections and the latter as input 'data' for the analysis. The analysis was performed using the `MBTS_2` trigger defined in Section 3.3. A random trigger can alternatively be used in the analysis to obtain $\mathrm{d}N_{\rm ch}/\mathrm{d}\eta$ and $\mathrm{d}N_{\rm ch}/\mathrm{d}p_T$ distributions for the inelastic (INEL) event sample.

Figures 6.9 and 6.10 show the corrected pseudorapidity distribution and the corrected transverse momentum spectrum for the minimum bias event sample, respectively. The $\mathrm{d}N_{\rm ch}/\mathrm{d}\eta$ distribution is integrated over $p_T > 0.15$ GeV/c and the $\mathrm{d}N_{\rm ch}/\mathrm{d}p_T$ distribution is integrated over $|\eta| < 2.5$. Statistical errors on the corrected distributions are shown. The aim has been to achieve statistical errors on the corrections of less than 2% per bin. The errors are mostly negligible since sufficient statistics were used to determine the correction factor. Data in regions where small statistical errors could not be achieved (i.e. near the edges of the acceptance) are not included in the analysis due to systematic effects.

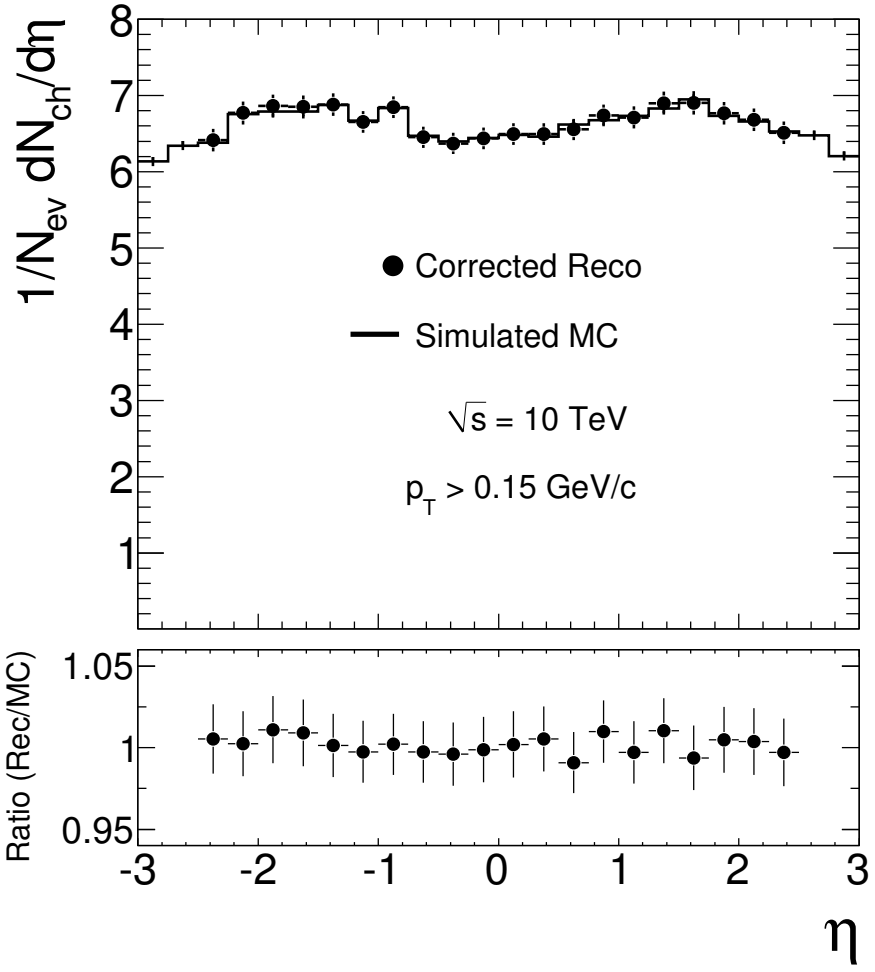

Figure 6.9: Corrected pseudorapidity density ($\mathrm{d}N_{\mathrm{ch}}/\mathrm{d}\eta$) for the minimum bias event sample, together with the Monte Carlo input to the simulation, integrated over $p_T > 0.15$ GeV/c. The distribution is normalized by the number of triggered events N_{ev}. In the lower part, the ratio of the analysis result over the Monte Carlo prediction is shown. Statistical errors are shown.

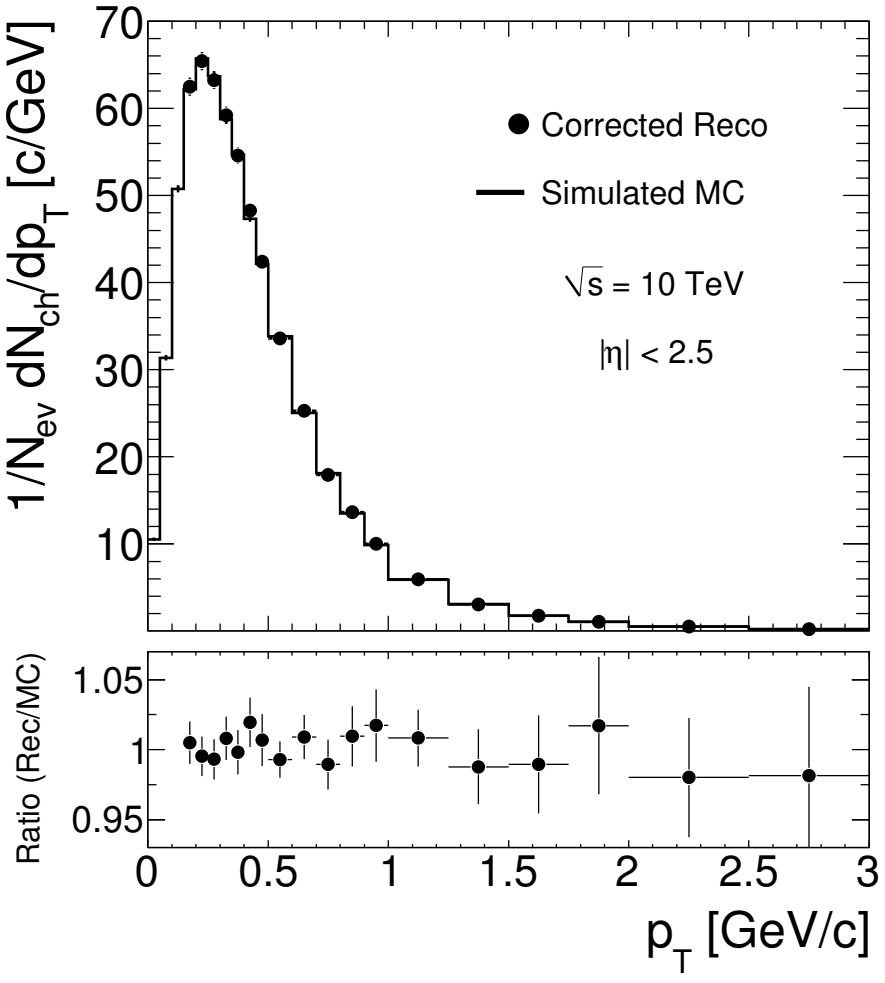

Figure 6.10: Corrected transverse momentum spectrum ($\mathrm{d}N_{\mathrm{ch}}/\mathrm{d}p_T$) for the minimum bias event sample, together with the Monte Carlo input to the simulation, integrated over $|\eta| < 2.5$. The distribution is normalized by the number of triggered events N_{ev}. In the lower part, the ratio of the analysis result over the Monte Carlo prediction is shown. Statistical errors are shown.

6.9 Invariant Yield

The invariant yield of charged particles $E\mathrm{d}^3N_{\mathrm{ch}}/\mathrm{d}^3p$ can be extracted from the same analysis presented here. The invariant yield can be written in terms of η and p_T as

$$E\frac{\mathrm{d}^3N_{\mathrm{ch}}}{\mathrm{d}^3p} = \frac{E}{p}\frac{\mathrm{d}^3\sigma}{p_T\mathrm{d}p_T\mathrm{d}\phi\mathrm{d}\eta}, \tag{6.9}$$

where

$$\frac{E}{p} = \sqrt{1+\left(\frac{m}{p_T\cosh\eta}\right)^2}. \tag{6.10}$$

A derivation of these expressions is given in Appendix B. The cross section σ has been replaced by the number of charged particles N_{ch}. Averaging Equation 6.9 over ϕ, we then get that

$$E\frac{\mathrm{d}^3N_{\mathrm{ch}}}{\mathrm{d}^3p} \implies \frac{1}{2\pi p_T}\frac{E}{p}\frac{\mathrm{d}^2N_{\mathrm{ch}}}{\mathrm{d}\eta\mathrm{d}p_T}. \tag{6.11}$$

The invariant yield of the minimum bias event sample is calculated by repeating the analysis and weighting each entry in the 2-D η-p_T histogram with the coefficient $E/(2\pi p_T p)$. The mass of the pion is assumed for all particles ($m = m_\pi$). Figure 6.11 shows the p_T-dependence of the corrected invariant yield for the minimum bias event sample. The distribution is integrated over $|y| < 2.0$, corresponding to pions with $p_T \gtrsim 0.1$ GeV/c and $|\eta| \lesssim 2.5$.

The corrected invariant yield spectrum has been fit with the Tsallis distribution [97]:

$$E\frac{\mathrm{d}^3N}{\mathrm{d}^3p} = A\ p_T\left[1+\frac{E_T(p_T)}{nT}\right]^{-n}, \tag{6.12}$$

where $E_T = \sqrt{m^2+p_T^2}-m$ and A, T, n are parameters of the fit. The term in brackets approximates a power law E_T^{-n} at high p_T ($E_T \gg nT$) and an exponential $e^{-E_T/T}$ at low p_T ($E_T \ll nT$). By combining the two behaviors, Equation 6.12 gives a reasonable description of distinct hard and soft parton physics [98]. The low-energy slope T is the same temperature parameter as in classical

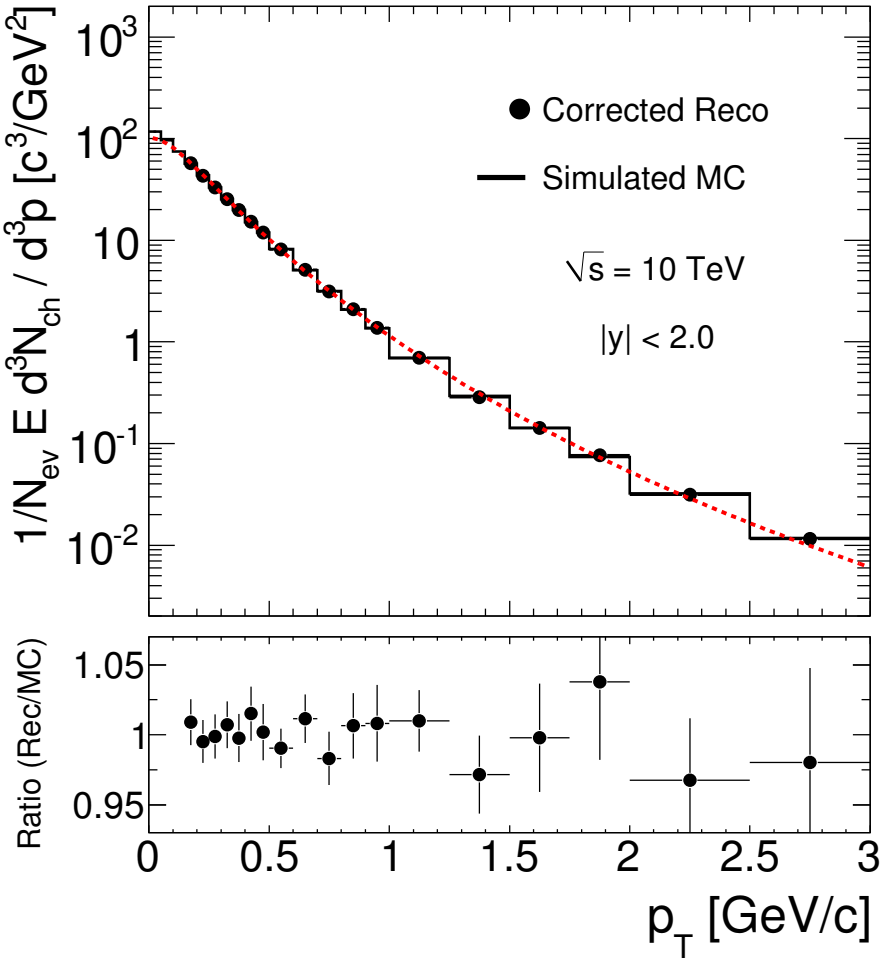

Figure 6.11: Corrected invariant yield ($E\mathrm{d}^3N_{\mathrm{ch}}/\mathrm{d}^3p$) for the minimum bias event sample, together with the Monte Carlo input to the simulation, integrated over $|y| < 2.0$. The mass of the pion is assumed for all particles. The distribution is averaged over ϕ and normalized by the number of triggered events N_{ev}. In the lower part, the ratio of the analysis result over the Monte Carlo prediction is shown. The red dashed line represents the best fit to the corrected data using the functional form given in Equation 6.12. Statistical errors are shown.

Brownian motion, while the exponent n describes the high-p_T power-law tail [98]. The average transverse momentum is given by [99]:

$$\langle p_T \rangle = \frac{2n}{(n-3)} T. \tag{6.13}$$

The parameters of the Tsallis fit shown in Figure 6.10 are $T = 0.1402 \pm 0.0018$ GeV and $n = 7.285 \pm 0.165$, with $\chi^2 = 23.4$ and $n_{\mathrm{dof}} = 15$. Using Equation 6.13, the average transverse momentum is $\langle p_T \rangle = 0.477 \pm 0.010$ GeV/c.

Chapter 7

Systematic Uncertainties

In this chapter, several sources of systematic uncertainty on the $\mathrm{d}N_{\mathrm{ch}}/\mathrm{d}\eta$ and $\mathrm{d}N_{\mathrm{ch}}/\mathrm{d}p_T$ measurements are discussed and estimated. The different effects studied here are considered independent in order to evaluate the total systematic uncertainty in a multi-dimensional parameter space. In general, however, many of the systematic uncertainties are not independent since the various detector and analysis corrections do not factorize completely.

The procedure for evaluating a given systematic effect is as follows. The input sample is divided into a correction sample and an analysis sample. The analysis is performed in the standard way described in Section 6.8. The systematic effect is then applied either on (a) the correction sample or (b) the analysis sample. In most cases, it is applied on the correction sample and the corrections are subsequently re-evaluated. In cases where the systematic uncertainty comes from an imperfect modeling of the detector in the simulation (e.g. in Sections 7.5 and 7.6), the systematic effect is instead applied on the analysis sample. The analysis is performed again using either (a) the modified corrections and the original analysis sample or (b) the original corrections and the modified analysis sample. The resulting modified $\mathrm{d}N_{\mathrm{ch}}/\mathrm{d}\eta$ and $\mathrm{d}N_{\mathrm{ch}}/\mathrm{d}p_T$ distributions are divided by the standard distributions and the calculated ratio is used as an estimate of the systematic effect.

In cases where the systematic uncertainty is introduced only at the analysis level, a simpler approach has been taken. The procedure is described in the relevant sections of this chapter. A summary of the total estimated systematic uncertainty is given at the end of the chapter. Note that the error estimates given in this chapter are likely to change with future versions of the simulation, reconstruction and analysis software.

7.1 Particle Composition

The track reconstruction correction $C_{\mathrm{trk}}(\eta, p_T)$ is calculated using events generated by PYTHIA with a standard ATLAS tune for pp events. Although pions, kaons and protons (and anti-protons) compose over 98% of all particles in these events, the reconstruction efficiency, and hence the track reconstruction correction, for each of these is considerably different for $p_T < 0.5$ GeV/c (see Figure 6.6). This model-dependency introduces a systematic uncertainty on the measurement since the relative abundances suggested by PYTHIA could differ in the data. The magnitude of the systematic error can be studied by artificially changing the particle abundances of the event generator. Note that this systematic error is highly dependent on the p_T cut chosen for the analysis. The results given here are for a p_T cut of 0.15 GeV/c.

To estimate the systematic effect, individual corrections are first calculated for each of the particle species π, ¸and p. A reconstructed track is considered to belong to a given particle species if it is associated to a Monte Carlo truth particle of that species (see Sections 4.7.2 and 5.4). The individual corrections are then re-combined after enhancing or reducing the weight of the single particle species corrections. Combining the corrections with a weight of unity for all species should result in exactly the same correction as the one obtained by the standard method.

Several modified corrections have been calculated by enhancing or reducing the number of kaons and/or protons by $\pm 50\%$. The largest effect is observed when both the number of kaons and protons are simultaneously enhanced (or reduced). Figure 7.1 shows the results of performing the

analysis with these modified corrections, as compared to using the standard composition correction. The plots show that despite a large uncertainty of ±50% in the number of kaons and protons, the associated systematic error is only about ±1%.

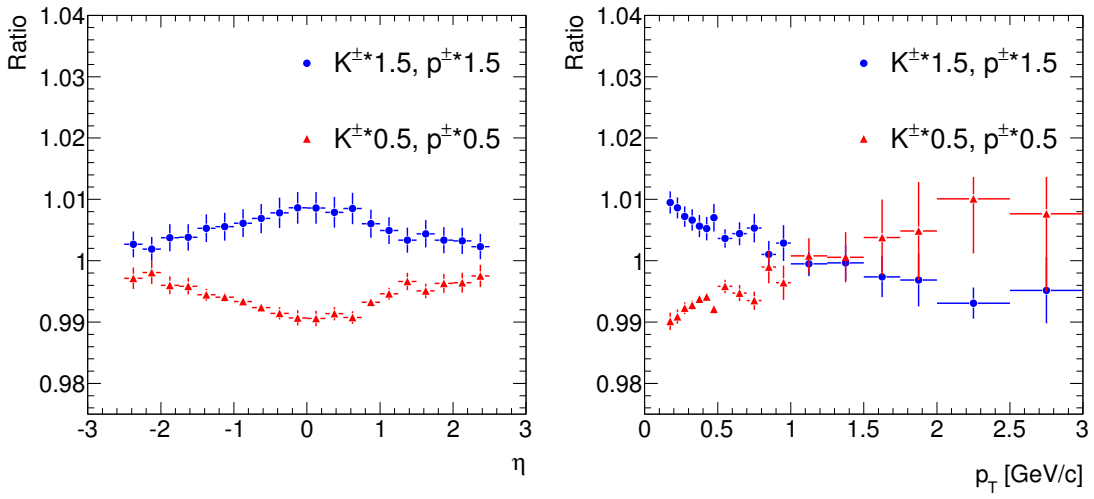

(a) (b)

Figure 7.1: Effect of artificially changing the particle species composition when calculating the track reconstruction correction. The plotted curves show the ratio of the $\mathrm{d}N_{\mathrm{ch}}/\mathrm{d}\eta$ (a) and $\mathrm{d}N_{\mathrm{ch}}/\mathrm{d}p_T$ (b) distributions obtained using a particle composition where the number of kaons and protons is changed by ±50% to the corresponding distributions obtained using the standard Pythia composition. The η plot is integrated over $p_T > 0.15$ GeV/c and the p_T plot is integrated over $|\eta| < 2.5$. The plots indicate a systematic uncertainty of about ±1%.

7.2 Diffractive Cross Sections

The vertex reconstruction correction is calculated from a sample of inelastic events with relative diffractive cross sections as predicted by Pythia. Since each of the inelastic physics processes (non-diffractive, single diffractive and double diffractive) have different average particle multiplicities and the vertex reconstruction efficiency, in turn, depends on the average particle multiplicity of the sample, the vertex reconstruction correction therefore depends on the relative cross sections among the different physics processes.

The cross sections predicted by the version and tuning of PYTHIA used in the simulation are: $\sigma_{\rm nd} = 51.6$ mb, $\sigma_{\rm sd} = 14.0$ mb and $\sigma_{\rm dd} = 9.8$ mb at $\sqrt{s} = 10$ TeV. In order to study the systematic error associated with the uncertainty in these relative cross sections, the corrections have been re-calculated after artificially changing the diffractive cross sections by $\pm 75\%$: $\sigma_{\rm sd} = 24.5$ mb, $\sigma_{\rm dd} = 17.2$ mb and $\sigma_{\rm sd} = 3.5$ mb, $\sigma_{\rm dd} = 2.5$ mb. This is sufficient to cover the difference in the predicted relative cross sections between PYTHIA and PHOJET (see Table 2.1).

Figure 7.2 shows the effect of changing the relative diffractive cross sections on the final $\mathrm{d}N_{\rm ch}/\mathrm{d}\eta$ and $\mathrm{d}N_{\rm ch}/\mathrm{d}p_T$ distributions, as compared to using the standard relative cross sections given by PYTHIA. The plots show that changing the diffractive cross sections by $\pm 75\%$ changes the result of the analysis by only about $\pm 0.2\%$. This is because no trigger bias correction is applied (see Section 6.2) and the vertex reconstruction correction is not greatly affected. Note that for the inelastic sample using a random trigger, this systematic uncertainty drops to 0%.

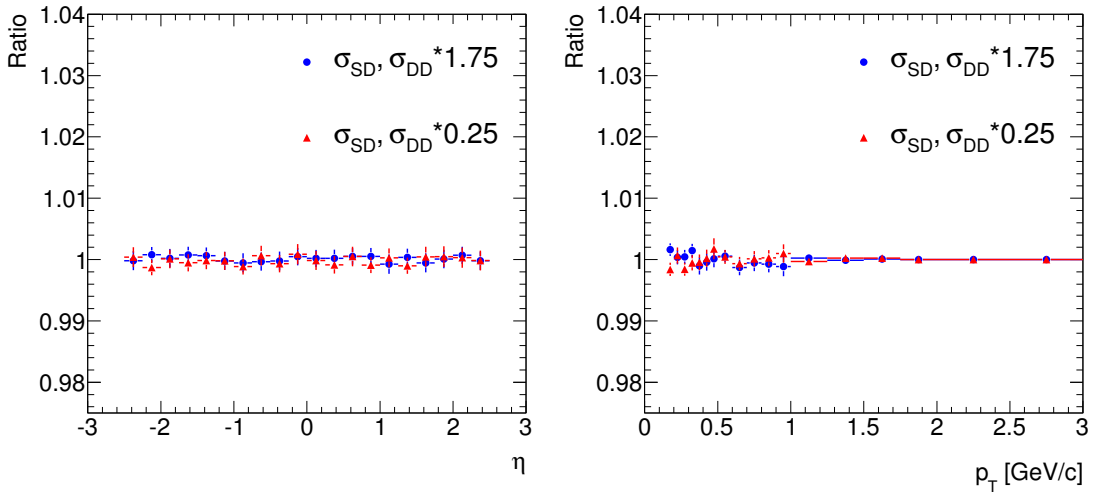

(a) (b)

Figure 7.2: Effect of artificially changing the relative diffractive cross sections when calculating the corrections. The plotted curves show the ratio of the $\mathrm{d}N_{\rm ch}/\mathrm{d}\eta$ (a) and $\mathrm{d}N_{\rm ch}/\mathrm{d}p_T$ (b) distributions obtained after changing the diffractive cross sections by $\pm 75\%$ to the corresponding distributions obtained using the standard diffractive cross sections predicted by PYTHIA. The η plot is integrated over $p_T > 0.15$ GeV/c and the p_T plot is integrated over $|\eta| < 2.5$. The plots indicate a systematic uncertainty of about $\pm 0.2\%$.

7.3 Vertex Reconstruction Bias

Since the z-position of the reconstructed vertex (v_z) is integrated out during the analysis (see Section 6.7), a v_z-dependent bias in the vertex reconstruction could introduce an additional systematic effect on the $\mathrm{d}N_{\mathrm{ch}}/\mathrm{d}\eta$ and $\mathrm{d}N_{\mathrm{ch}}/\mathrm{d}p_T$ measurement. To check for any such bias in the reconstructed event sample, the v_z residual and resolution were calculated in the same way as for the track parameters (see Section 5.1).

Figure 7.3 shows the mean residual $\langle \Delta v_z \rangle$ and resolution σ_{v_z} as a function of generated v_z. The resolution is calculated over a range which includes 99.7% of the data (corresponding to $\pm 3\sigma$) [6]. The plots illustrate that the error on the v_z measurement is on average not dependent on v_z and that the shape of the error is roughly symmetric around $v_z = 0$. This indicates that there is no v_z-dependent bias caused by the vertex reconstruction. This result can be confirmed by calculating the systematic uncertainty on the measurement when using the generated v_z, rather than the reconstructed v_z, to calculate the vertex reconstruction correction, for various ranges of v_z. All show negligible deviations below $\pm 0.1\%$ [95].

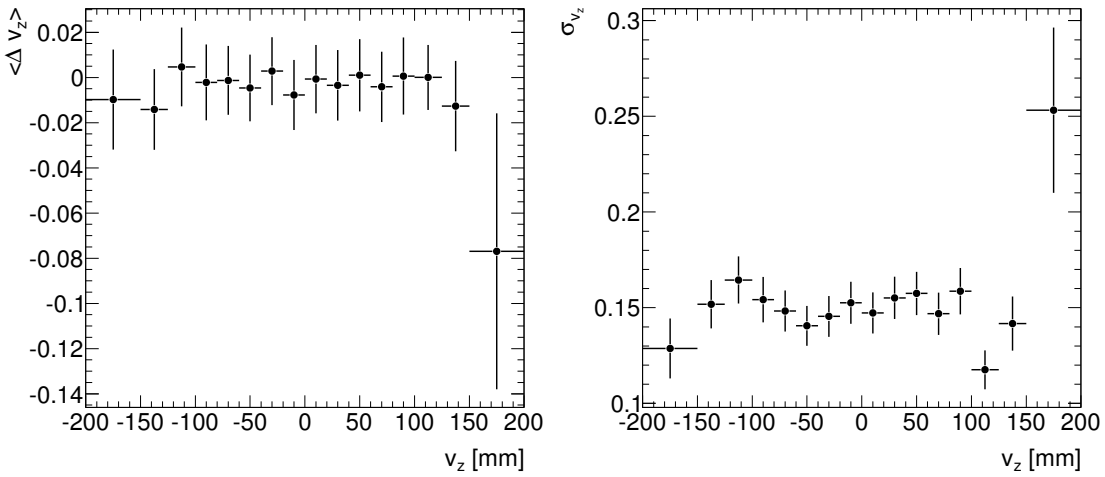

(a) (b)

Figure 7.3: Mean residual $\langle \Delta v_z \rangle$ (a) and resolution σ_{v_z} (b) of v_z as a function of generated v_z for the minimum bias event sample. The plots indicate that there is no v_z-dependent bias introduced by the vertex reconstruction.

7.4 Pile-Up and Beam Gas

Beam-gas and pile-up backgrounds can contaminate the minimum bias event sample, reducing the average particle multiplicity and introducing an additional systematic uncertainty on the $\mathrm{d}N_{\mathrm{ch}}/\mathrm{d}\eta$ and $\mathrm{d}N_{\mathrm{ch}}/\mathrm{d}p_T$ measurements.

The rate of beam-gas interactions is highly dependent on the particular beam conditions during the start-up phase of the LHC. The LHC group has studied the effect of several factors, including the number of protons per bunch, beam current, amount of debris in the beam pipe, etc. [100]. The total beam-gas interaction rate along the length of ATLAS is estimated to be about 100 Hz during machine start-up. This rate should be taken as speculative since particular factors, such as the quality of the vacuum in the beam pipe or the presence of debris, could easily be mis-estimated. Assuming a luminosity of 10^{31} cm^{-2}s^{-1} and a bunch spacing of 75 ns, the rate of inelastic pp events is 792 kHz, or 1 beam-gas event per 7920 pp events [3].

The efficiency of triggering on beam-gas interactions with the `MBTS_2` trigger is 83% (see Section 3.6). Since the trigger efficiency for all inelastic pp events is about 92%, the contamination from beam-gas interactions in the triggered event sample is estimated to be about 0.012%. Preliminary studies show that only 0.6% of the simulated beam-gas events pass the vertex reconstruction requirements given in Section 3.8 [95]. The contamination from beam-gas interactions in the sample of triggered events meeting the vertex requirements is therefore estimated to be 0.6 events per million. Thus the effect of beam-gas interactions is expected to be very small during LHC start-up. Taking a conservative approach, the assigned systematic uncertainty is $\pm 1\%$.

Background from pile-up events is not expected to introduce any significant systematic uncertainties during LHC start-up due to the low luminosity. At a luminosity of 10^{31} cm^{-2}s^{-1} and a bunch spacing of 75 ns, there will be a mean number of events per bunch crossing of 0.06 [3, 101]. At this luminosity and collision rate, the probability of a second interaction occurring in an event

with at least one interaction can be calculated using Poisson statistics:

$$\frac{P(N \geq 2; \mu)}{P(N \geq 1; \mu)} = \frac{1 - P(N = 0; \mu) - P(N = 1; \mu)}{1 - P(N = 0; \mu)}, \tag{7.1}$$

where $P(N; \mu)$ is the Poisson distribution

$$P(N; \mu) = \frac{\mu^N e^{-\mu}}{N!} \tag{7.2}$$

for a mean number of occurrences μ. Using $\mu = 0.06$, the probability of a second interaction in a triggered event is then about 3%. The majority of these events will have multiple reconstructed primary vertices and can therefore be identified and rejected by the analysis. The uncertainty only enters for events with two interactions within the v_z resolution of the vertex reconstruction. Using an upper limit on the resolution σ_{v_z} of 0.3 mm (see Figure 7.3) and an expected variance of the beam at $\sqrt{s} = 10$ TeV of 3–4 cm [102], the percentage of overlapping collisions in the Inner Detector is less than 1%. This must then be multiplied by the second-interaction probability calculated above. Thus multiple collisions can easily be resolved in the ID and systematic errors from pile-up can be neglected.

Studies of beam-halo events at the LHC using the FLUKA event generator [103,104] are currently ongoing. A systematic uncertainty due to contamination from beam-halo background is therefore not given here.

7.5 Mis-alignment

The ATLAS detector description (`ATLAS-GEO-08-00-00` geometry tag) used to simulate and reconstruct the minimum bias event sample (see Appendix A) corresponds to the ideal, perfectly-aligned detector. In reality, this ideal geometry is changed by several uncertainties: global positioning of the sub-detectors with respect to each other, local positioning of the detector modules within a sub-detector, deformation by weight from other components, distortions in the magnetic field, imperfect production and dead channels, etc.

7.5.1 'Day-1' mis-alignment

The alignment of the ATLAS detector will be a challenging task that is of particular interest at the start-up phase of the experiment. Initial alignments have been performed following cosmic ray data-taking with ATLAS in 2008 [105]. Using these data, the ID Alignment group has provided a set of alignment constants representing the expected performance on 'Day 1' of LHC data-taking [106]. To determine the set of constants, a random mis-alignment is introduced at the module level (known as a 'Level-3' mis-alignment) with a Gaussian distribution centered around zero and a width suggested by the residual distributions from cosmic data.

The tags for the predicted 'Day-1' mis-alignment are `InDetSi_Day1-04` and `InDetTRT_Day1-04`. The positions of the modules have only been smeared in the local X and Y directions. No ϕ dependence was introduced and no systematic 'weak mode' mis-alignments, such as curl or twist, were simulated for these tags [107]. The width of the smearing has been determined by quadratically subtracting the width of the residual distribution observed in cosmic data from the width in simulated cosmic events using ideal alignment. Table 7.1 lists the Gaussian widths used for each of the ID sub-detectors in the 'Day-1' mis-alignment tags [107]. The widths in the end-cap region have been increased to reflect lower track statistics and a degradation in the performance of the alignment. The 'Day-1' scenario has been shown to be a good approximation of the current alignment that was derived with cosmics [108].

Sub-detector	Barrel	End-cap
Pixel	20 μm	50 μm
SCT	20 μm	50 μm
TRT	100 μm	100 μm

Table 7.1: Expected level of Inner Detector mis-alignments on 'Day-1' of LHC collision data. Alignment constants are generated by introducing random mis-alignments at the module-level (local X and Y coordinates), with Gaussian distributions centered around zero and widths as shown here. A different level of mis-alignment is expected in the barrel and end-cap of each of the sub-detectors due to limited cosmic ray data taken with the end-caps. The mis-alignment scenario described here corresponds to the tags `InDetSi_Day1-04` and `InDetTRT_Day1-04`. Taken from [107].

7.5.2 Impact of 'Day-1' mis-alignment

The minimum bias event sample described in Appendix A was reconstructed with the ideal detector (`ATLAS-GEO-08-00-00` geometry tag) and the `InDetSi_Day1-04` and `InDetTRT_Day1-04` mis-alignment tags. Measurement errors in the ID were scaled to account for differences between the errors provided by the cluster formation and those seen by the tracking due to mis-alignments. This *error scaling* helps guarantee proper tracking in terms of track scoring, outlier flagging, tracking efficiency and parameter resolution by correcting the measurement errors [107].

The resulting mis-aligned sample can be directly compared to the ideal sample since they are both based on the same set of generated events. An important measure for understanding the impact of the mis-alignment is to compare the track parameter resolutions (see Section 5.1) with the ideal sample. In particular, a change in the transverse and longitudinal impact parameter resolutions can affect the number of tracks accepted or rejected by the track-to-vertex cut. This will be discussed further in the following section.

Figure 7.4 shows the d_0 and z_0 track parameter resolutions for the 'Day-1' mis-aligned sample, compared to the ideal sample, as a function of η. Essentially no change in the z_0 resolution is observed, which is as expected since the positions of the modules have not been smeared in the z direction. A degradation in the d_0 resolution of about 5 μm at $\eta = 0$ and 20 μm at $|\eta| = 2.0$ is observed, consistent with the Gaussian widths for the barrel and end-cap regions given in Table 7.1[1].

To estimate the effect of the 'Day-1' mis-alignment on the $\mathrm{d}N_{\mathrm{ch}}/\mathrm{d}\eta$ and $\mathrm{d}N_{\mathrm{ch}}/\mathrm{d}p_T$ measurements, the corrections were derived using events simulated with the ideal geometry and then applied to the same events simulated with the mis-aligned geometry. The result is compared to the standard distributions using only the ideal geometry. Figure 7.5 shows the effect of the 'Day-1' mis-alignment scenario on the final $\mathrm{d}N_{\mathrm{ch}}/\mathrm{d}\eta$ and $\mathrm{d}N_{\mathrm{ch}}/\mathrm{d}p_T$ distributions. The estimated systematic effect for this level of mis-alignment is about $\pm$(1–1.5)%.

[1]The smearing of 20 μm (50 μm) in the barrel (end-cap) region is added in quadrature to the 'Ideal' resolution of several hundred microns (see Section 5.1).

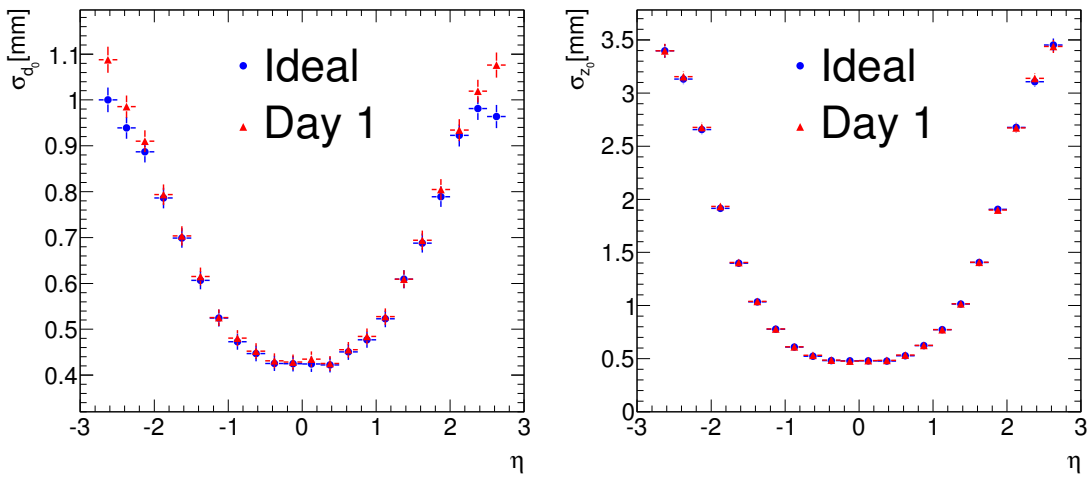

(a) d_0 (b) z_0

Figure 7.4: Resolutions of the d_0 (a) and z_0 (b) impact parameters versus η for the minimum bias event sample simulated with the 'Day-1' mis-alignment scenario (red triangles), compared to the standard ideal geometry (blue triangles). Both plots are integrated over $p_T > 0.15$ GeV/c. TRT stand-alone tracks have been excluded.

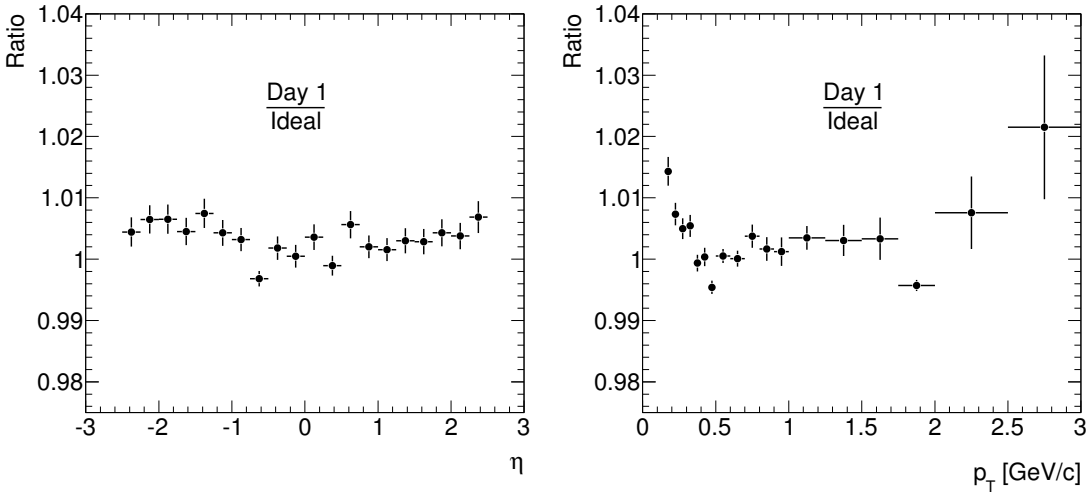

(a) (b)

Figure 7.5: Effect of the 'Day-1' mis-alignment scenario on the final $\mathrm{d}N_{\mathrm{ch}}/\mathrm{d}\eta$ (a) and $\mathrm{d}N_{\mathrm{ch}}/\mathrm{d}p_T$ (b) distributions. Corrections were derived using events simulated with the ideal geometry (`ATLAS-GEO-08-00-00`) and applied to the same sample of events simulated with the mis-aligned geometry (`ATLAS-GEO-08-00-00` plus `InDetSi_Day1-04` and `InDetTRT_Day1-04` tags). The plotted curves show the ratio of the final mis-aligned result to the standard result using only the ideal geometry. The η plot is integrated over $p_T > 0.15$ GeV/c and the p_T plot is integrated over $|\eta| < 2.5$. The plots indicate a systematic uncertainty of about $\pm$(1–1.5)%.

7.6 Track-to-Vertex Resolution

Most of the tracks coming from secondary particles are removed by the track-to-vertex cut, which requires that tracks originate from the primary vertex of the interaction (see Section 5.6). This cut removes all tracks that have a normalized distance $\rho \geq 4.0$ from the reconstructed primary vertex. ρ is a function of the transverse and longitudinal impact parameters (d_0, z_0) and their corresponding track errors (σ_{d0}, σ_{z0}), as well as the position (v_x,v_y,v_z) of the reconstructed primary vertex (see Equation 5.6). If any of these parameters are not measured correctly, e.g. due to errors in the track or vertex fit, or detector mis-alignments or mis-calibrations, the number of selected tracks will change and an associated systematic uncertainty will result.

This systematic uncertainty can be estimated by smearing the d_0^{PV} and z_0^{PV} resolutions and comparing the corrected distributions to the standard ones. Directly smearing d_0^{PV} and z_0^{PV} allows errors in both the track and vertex fitting to be combined into one systematic uncertainty. Figure 7.6 shows the effect of smearing the transverse and longitudinal track-to-vertex distances by 10% and 15% on the final $\mathrm{d}N_{\mathrm{ch}}/\mathrm{d}\eta$ and $\mathrm{d}N_{\mathrm{ch}}/\mathrm{d}p_T$ distributions. The standard corrections were applied to a sample with smeared resolutions and the result was then compared to the standard distributions with no smearing. The smearing values of 10% and 15% were motivated by the smearing observed in the 'Day-1' mis-alignment scenario (see Section 7.5). However, a more conservative 'worst-case' approach has been taken. Figure 7.6 shows that a 15% mis-estimate of the track-to-vertex resolution leads to a systematic effect of about +(2–3)%.

7.7 Secondary Track Contamination

The ζ component (see Equation 5.11) of the track reconstruction correction measures the contamination from secondary and fake tracks entering the track sample to be analyzed. The contribution from 'fake' tracks can be ignored since less than 0.2% of selected tracks are poorly matched to generated particles (see Figure 5.11 on page 97). The contribution from secondary tracks, however,

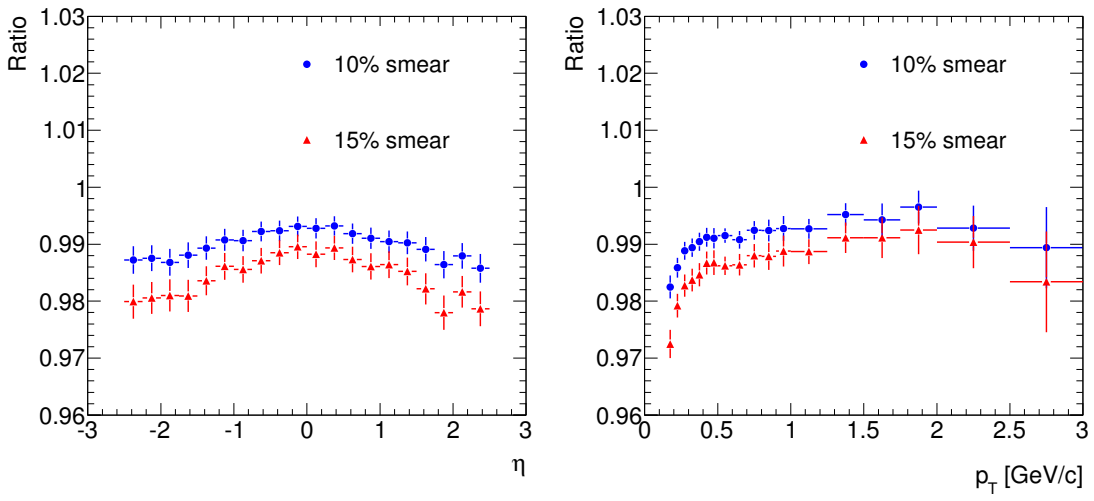

(a) (b)

Figure 7.6: Effect of smearing the d_0^{PV} and z_0^{PV} track-to-vertex resolutions by 15% when calculating the track reconstruction correction. The plotted curves show the ratio of the $\mathrm{d}N_{\mathrm{ch}}/\mathrm{d}\eta$ (a) and $\mathrm{d}N_{\mathrm{ch}}/\mathrm{d}p_T$ (b) distributions obtained after smearing the track-to-vertex distances to the corresponding standard distributions with no smearing. The η plot is integrated over $p_T > 0.15$ GeV/c and the p_T plot is integrated over $|\eta| < 2.5$. The plots indicate a systematic uncertainty of about $-(3\text{–}4)\%$.

is about 3%. The secondary rate measured in the simulation depends on the amount of secondary hadronic and electromagnetic interactions in the detector material (predicted by GEANT) and on the efficiency of reconstructing secondary particles. Since both of these could differ in the data, there is an uncertainty on the secondary track contamination and on the $\mathrm{d}N_{\mathrm{ch}}/\mathrm{d}\eta$ and $\mathrm{d}N_{\mathrm{ch}}/\mathrm{d}p_T$ measurements. Note that tracks from background sources, such as cosmic rays and beam-gas interactions, can be neglected since they have an extremely small probability of pointing back to the reconstructed primary event vertex and are therefore rejected by the track-to-vertex cut.

Figure 7.7 shows the ratio of secondary tracks to primary tracks after the track selection as a function of η and p_T. Before cuts are applied, the number of tracks originating from secondary particles is 39.1% of the number of tracks originating from primary particles. After the track selection, the number of accepted secondary tracks is 2.9% of the number of accepted primary tracks. The secondary rate is highest in the low-p_T region and vanishes only above $p_T > 5$ GeV/c. If the number of secondaries were to be mis-estimated by $\pm 50\%$, the total number of accepted tracks

would change by ±1.5%. Due to the effectiveness of the track selection, the number of secondaries should not be mis-estimated by more than 50%. The systematic uncertainty is therefore estimated to be ±1.5%.

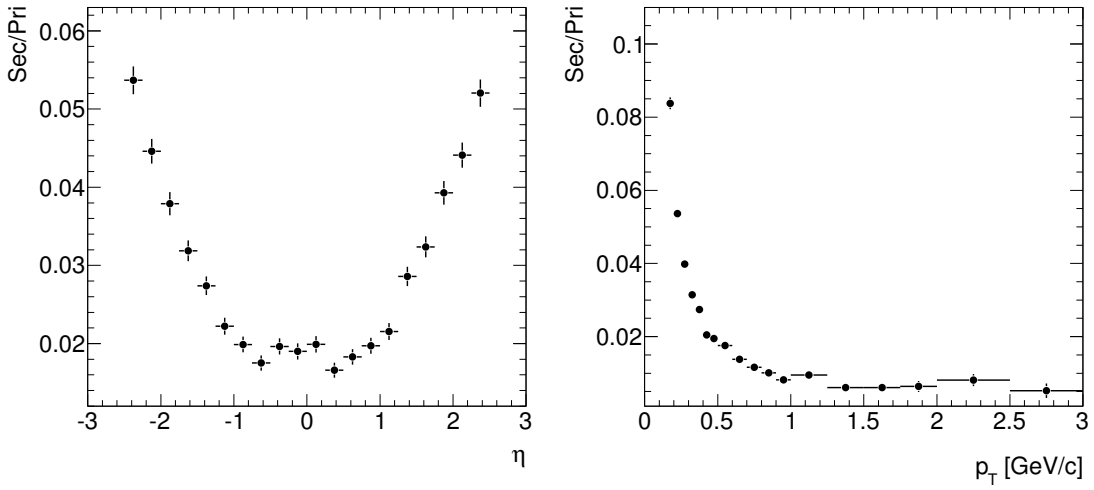

(a) (b)

Figure 7.7: Ratio of secondary to primary tracks after track selection cuts are applied as a function of η (a) and p_T (b) for the minimum bias event sample. The η plot is integrated over $p_T > 0.15$ GeV/c and the p_T plot is integrated over $|\eta| < 2.5$. The average ratio before and after cuts is 39.1% and 2.9%, respectively. A mis-estimate of the number of secondaries by ±50% leads to a ±1.5% uncertainty on the number of accepted tracks.

7.8 Truth Probability

In Section 5.4, a cut of 50% on the truth probability (see Equation 5.3) was used to distinguish between well-matched and poorly-matched truth association. The same cut was also used to define 'found' generated particles and 'fake' reconstructed tracks in Sections 5.5.1 and 5.7.2. This somewhat arbitrary cut value introduces an uncertainty on the individual components of the track reconstruction correction (see Equation 6.1), particularly the efficiency and the contamination. However the truth probability cut is not used to calculate the total track reconstruction correction itself. Therefore, the associated systematic uncertainty on $\mathrm{d}N_{\mathrm{ch}}/\mathrm{d}\eta$ and $\mathrm{d}N_{\mathrm{ch}}/\mathrm{d}p_T$ is zero.

7.9 Total Systematic Uncertainty

The systematic uncertainties on the $\mathrm{d}N_{\mathrm{ch}}/\mathrm{d}\eta$ and $\mathrm{d}N_{\mathrm{ch}}/\mathrm{d}p_T$ measurements discussed in this chapter are summarized in Tables 7.2 and 7.3, respectively. The uncertainty on $\mathrm{d}N_{\mathrm{ch}}/\mathrm{d}\eta$ is given for two p_T ranges: $p_T > 0.15$ GeV/c and $p_T > 0.4$ GeV/c. The uncertainty on $\mathrm{d}N_{\mathrm{ch}}/\mathrm{d}p_T$ is given for two η ranges: $|\eta| < 2.5$ and $|\eta| < 1.0$. The total systematic uncertainty is calculated by assuming each of the individual uncertainties are independent and summing them in quadrature. Positive and negative uncertainties are summed separately. Note that the total systematic uncertainties for $|\eta| < 1.0$ and $p_T > 0.4$ GeV/c are significantly smaller than for $|\eta| < 2.5$ and $p_T > 0.15$ GeV/c since there is less detector material in the barrel region and better reconstruction performance at higher p_T.

Uncertainty ($\mathrm{d}N_{\mathrm{ch}}/\mathrm{d}\eta$)	$p_T > 0.15$ GeV/c	$p_T > 0.4$ GeV/c
Particle composition	± 1.0 %	± 1.0 %
Diffractive cross sections	± 0.2 %	± 0.2 %
Vertex reconstruction bias	± 0.1 %	± 0.1 %
Beam-gas and pile-up	± 1 %	± 1 %
Mis-alignment	± 1.0 %	± 0.5 %
Track-to-vertex resolution	$+2.0$ %	$+2.0$ %
Secondary track contamination	± 1.5 %	± 1.0 %
Total	$+\mathbf{3.0}$ % $-\mathbf{2.3}$ %	$+\mathbf{2.9}$ % $-\mathbf{2.1}$ %

Table 7.2: Summary of the various systematic uncertainties on $\mathrm{d}N_{\mathrm{ch}}/\mathrm{d}\eta$ discussed in this chapter. Estimates are given for two p_T ranges: $p_T > 0.15$ GeV/c and $p_T > 0.4$ GeV/c. The total systematic error is calculated by assuming each of the individual uncertainties are independent and summing them in quadrature.

It is important to distinguish uncertainties which are introduced at the generator level from those that are introduced at the reconstruction or analysis level. Uncertainties coming from event generator predictions at the LHC energy scale, such as particle composition and relative diffractive cross sections, are to a large degree unavoidable in the first analysis with data. On the other hand, uncertainties that are introduced during reconstruction or analysis, such as mis-alignment

Uncertainty ($\mathrm{d}N_{\mathrm{ch}}/\mathrm{d}p_T$)	$\lvert\eta\rvert < 2.5$	$\lvert\eta\rvert < 1.0$
Particle composition	± 1.0 %	± 1.0 %
Diffractive cross sections	± 0.2 %	± 0.2 %
Vertex reconstruction bias	± 0.1 %	± 0.1 %
Beam-gas and pile-up	± 1 %	± 1 %
Mis-alignment	± 1.5 %	± 1.0 %
Track-to-vertex resolution	$+3.0$ %	$+2.0$ %
Secondary track contamination	± 1.5 %	± 1.0 %
Total	$+\mathbf{3.9}$ % $-\mathbf{2.6}$ %	$+\mathbf{2.8}$ % $-\mathbf{2.0}$ %

Table 7.3: Summary of the various systematic uncertainties on $\mathrm{d}N_{\mathrm{ch}}/\mathrm{d}p_T$ discussed in this chapter. Estimates are given for two η ranges: $|\eta| < 2.5$ and $|\eta| < 1.0$. The total systematic error is calculated by assuming each of the individual uncertainties are independent and summing them in quadrature.

and contamination from secondary tracks, can possibly be improved with better understanding of the detector or an upgraded version of the analysis.

Chapter 8

Analysis with Data

The minimum bias analysis presented in Chapter 6 uses a sample of simulated events as 'data' input to the analysis. This simulation is a modest attempt to recreate the analysis chain that will be performed on actual data from the LHC. In reality, the story is considerably more complicated since the simulation may not accurately reflect what is seen in the measured data. In addition, there is no longer any reliable connection to the MC truth information, as there was in the simulation.

Instead, a series of cross-checks should be made before applying the corrections described in Chapter 6 on the measured data. A proposed method for making these cross-checks is outlined in this chapter. The underlying principle is to compare several distributions of measured and simulated data in order to verify that the simulation is correctly reproducing the experimental conditions. Any discrepancies should be understood before performing the analysis on data. In some cases, the simulation may need to be adapted and the corrections subsequently re-evaluated. The cross-checks described here also serve as a way to better understand and minimize the systematic uncertainties discussed in Chapter 7.

8.1 Event and Vertex Quality

The event composition of the minimum bias data sample will include non-diffractive, single-diffractive and double-diffractive interactions, as well as background events coming from beam-gas and beam-halo. Background coming from empty (noise) events should be negligible, assuming that the trigger has been commissioned and validated to be working properly.

To assess the contamination of beam-gas and beam-halo interactions in the minimum bias data sample, events should be recorded with the minimum bias trigger during single-beam running of the LHC (e.g. during the commissioning phase). The trigger rate for such events should correspond to the expected rate discussed in Section 7.4. The expected rate depends on various LHC running conditions (e.g. luminosity, beam intensity and the quality of the vacuum in the beam pipe), several of which may not be precisely known at the start of data-taking. However, a reasonable estimate of the expected rate should be possible [100]. If the measured beam-gas and beam-halo trigger rates differ greatly from this value, the most probable cause is a different trigger sensitivity to these events than was seen in the simulation.

After LHC collision data has been taken, properties of the triggered event sample should be compared to the corresponding events in the simulation. For example, the event-level and track-level vertex reconstruction corrections can be calculated directly from the triggered data (see Section 6.5) and compared to the simulation. A large discrepancy in the event-level correction signifies a difference in the vertex reconstruction efficiency, which could be caused by an excess of low-multiplicity events or events at high $|v_z|$. The first suspect in both of these cases is beam-gas or beam-halo events. N and v_z distributions of the events should be studied to investigate the cause of the discrepancy. Event criteria can also be tightened (e.g. $|v_z|$ range) until the measured and simulated data agree with each other, then gradually loosened back to their original values.

Comparing the track-level corrections can help determine if the vertex reconstruction correction is reasonable or if it is causing some bias in the measured track distribution. For example, a

comparison of the v_z distribution of reconstructed primary vertices will indicate if there is a v_z-dependent bias on the track-level corrections or distributions. If a bias is observed, the track-level corrections should additionally be calculated as a function of v_z. Then the results will not depend on the v_z distribution assumed in the simulation. An alternative strategy is to run the analysis for various v_z ranges. Any discrepancies between the final $\mathrm{d}N_{\mathrm{ch}}/\mathrm{d}\eta$ and $\mathrm{d}N_{\mathrm{ch}}/\mathrm{d}p_T$ distributions for the different v_z ranges should be investigated.

Finally, the v_z resolution σ_{v_z} can be measured in data by dividing the number of tracks in each event in half and fitting separate vertices to each group of tracks. The difference in the v_z measured for each vertex gives a residual distribution whose resolution can be calculated. Assuming that σ_{v_z} is equal for both vertices, the single-vertex resolution can be determined. This strategy will work reasonably well for high-multiplicity events, but may not work down at low N. However, plotting the resolution as a function of N and extrapolating a fitted curve to the low-N part can at least give some estimate of the resolution for low-multiplicity events.

8.2 Track Quality

Similar methods should be used to gain confidence in the quality of the selected track sample. Validation of the track reconstruction is an important prerequisite to a minimum bias analysis with LHC data. In turn, minimum bias data can be used to study the performance of the tracking by making comparisons to the simulated data. The low-p_T tracking (see Section 4.4.2) will especially need to be studied early on.

Several track parameter distributions should be compared between measured and simulated data. The most important are the η and p_T resolutions and the parameters used to select tracks: the b-layer hit efficiency and the track-to-vertex resolutions $\sigma_{d_0^{\mathrm{PV}}}$ and $\sigma_{z_0^{\mathrm{PV}}}$. These cuts have the largest influence on the track sample (see Table 5.3). If the b-layer hit efficiency measured in the data does not match the simulation, the simulation should be adjusted appropriately. This study,

together with a study of the track-to-vertex resolutions, will give some idea of how well primary and secondary tracks can be separated in the data. The largest uncertainty in the impact parameter resolutions is discussed in Section 8.3.

A useful strategy for comparing the track parameters between data and simulation is to group the reconstructed tracks in different η or p_T ranges. High-p_T tracks at low $|\eta|$ will be relatively easy to understand in early data. Lower p_T tracks can be added gradually while making any necessary changes in the simulation, such as a scaling of the track errors. For this reason, any measured track parameters that have been normalized by the track error are especially good for comparing data and simulation.

As an illustrative example, Figure 8.1 shows the normalized track-to-vertex distance ρ (see Equation 5.6) for various p_T ranges: 'PtHigh' ($p_T \geq 0.8$ GeV/c), 'PtMed' ($0.4 \leq p_T < 0.8$ GeV/c) and 'PtLow' ($p_T < 0.4$ GeV/c). If the track errors have been estimated correctly, the peak of the distribution will be at $\rho = 1$ for all p_T ranges. If, for example, a discrepancy in the low-p_T range is observed, then the track errors might need to be scaled appropriately or the material might not be mapped correctly (see Section 8.3). The ρ distribution is of special importance because the track-to-vertex cut has the largest influence on the rejection of secondary tracks.

The strategy described here should also be used to study the effect of the various track-level cuts on the different η and p_T ranges. Comparing the influence of the cuts in data and in simulation will indicate if any of the cuts are biasing the measured distributions differently than was seen in the simulation.

8.3 Material Mapping

Although impossible to know *a priori*, the largest uncertainty between the simulation and early measured data will most likely be the material description of the detector used in the simulation, which may not accurately reflect the as-built detector. Many of the track parameter quantities

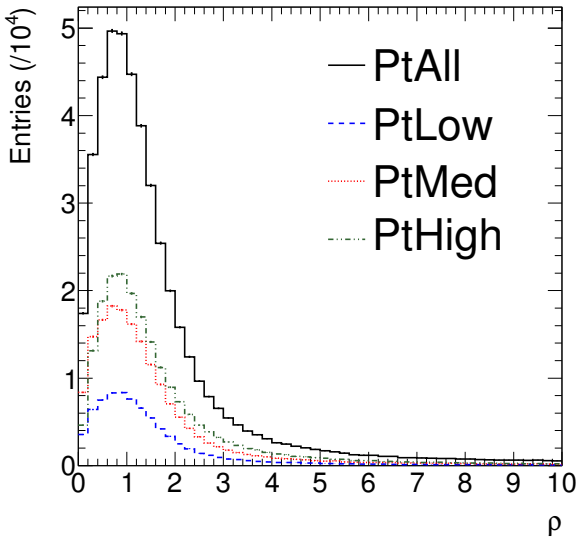

Figure 8.1: Normalized track-to-vertex distance (ρ) for various p_T ranges. The groups labeled 'PtHigh', 'PtMed' and 'PtLow' correspond to tracks with $p_T \geq 0.8$ GeV/c, $0.4 < p_T < 0.8$ GeV/c and $p_T \leq 0.4$ GeV/c, respectively.

critical for the minimum bias analysis, such as the d_0 resolution, are extremely dependent on the amount of material in the detector. The number of secondary particles in the detector also depends significantly on the amount of detector material.

The d_0 resolution essentially has two components: a Gaussian part coming from multiple scattering with the material and a non-Gaussian tail coming from mistakes by the pattern recognition due to material interactions. The Gaussian part is relatively easy to model in the data. Also, since the cut on the track-to-vertex distance ρ is placed at more than a 3σ-equivalent of the distribution, a 10% uncertainty on the d_0 resolution does not make a huge difference (see Section 7.6). The non-Gaussian part, however, does matter. The minimum bias analysis is particularly sensitive because the tracking sometimes links parts of a primary segment with parts of other outgoing segments.

The weight of the material in the detector is well-known to within $\pm 5\%$ since each component of the detector has been weighed before installation. The composition of the material, however, is not as well-known. Thus validating the ATLAS material description will be a critical part of the

minimum bias analysis with data. One strategy will be to map the detector material using photon conversions. This technique requires significant statistics and there will be a compromise between taking the time to better understand the material and accepting some uncertainty due to material budget for an earlier measurement.

If new material is determined from the study with photon conversions, the reconstructed tracks should be refit with the new material map and the simulated data should be regenerated to obtain an improved estimate of the impact parameter resolution and the number of secondaries.

8.4 Data-Driven Corrections

In Chapter 6, the track reconstruction correction was derived from a sample of simulated inelastic events. The simulation could, of course, differ from reality for many of the reasons described here and in Chapter 7. This is especially true of the particle abundances and the relative cross sections among the various non-diffractive and diffractive inelastic physics processes. These uncertainties have an impact on the track reconstruction correction, as shown in Sections 7.1 and 7.2. Before applying these corrections to the data, an attempt should be made to calculate the components of the correction directly from the data. This will allow an unbiased comparison between the data and the simulation.

For example, the primary track reconstruction efficiency ϵ (see Equation 5.4) can be calculated by embedding simulated tracks into a sample of real minimum bias events. A comparison with the standard correction will reveal if any effects have not been foreseen in the simulation. The migration M and acceptance A can also be determined using this method. Another way to cross-check the efficiency calculated in the simulation is to rerun the reconstruction with either of the silicon detectors disabled. Track segments from the pixel detector or the SCT can then be played against each other to measure the tracking efficiency. There is an intrinsic p_T limit to this strategy of about 0.15–0.2 GeV/c due to tracks not reaching the end of the SCT. If any disagreements between

data and simulation are observed, further investigation is needed before performing the analysis on measured data. This study will immensely help in minimizing the systematic uncertainty on the efficiency component of the correction.

The remaining component of the track reconstruction correction is the contamination ζ of fake tracks and tracks coming from secondary particles. As discussed in the previous section and in Section 7.7, there are many uncertainties on the secondary rate derived from the simulation. A data-driven method for calculating this correction is therefore needed. One possibility is to extrapolate the tails of the transverse or longitudinal track-to-vertex distance distributions to get a handle on the number of secondaries surviving the track selection criteria. The extrapolated background can then be subtracted from the measured distributions. Because this should be done for every bin in η-p_T, this strategy requires more statistics than the number of events used here. If the data disagree with the tails in the simulation, this could point to an excess or deficiency of material in the detector description.

It is important to understand any differences between the components of the track reconstruction correction for measured and simulated data. It may be necessary to adapt the simulation to correctly reproduce what is observed in the actual data.

8.5 Additional Cross-checks

Once the distributions discussed here are well understood, an additional set of cross-checks should be performed in order to better understand and possibly minimize any systematic uncertainties. The $\mathrm{d}N_{\mathrm{ch}}/\mathrm{d}\eta$ and $\mathrm{d}N_{\mathrm{ch}}/\mathrm{d}p_T$ distributions should be obtained using different sets of correction maps. For example, corrections derived from a simulation using PYTHIA should be compared to one using PHOJET. Specifics of the analysis can also be changed, such as cutting on the track-to-vertex distance in mm, instead of the normalized distance ρ. Another example is to define the multiplicity as the number of silicon clusters instead of the number of reconstructed tracks. Different v_z ranges

and different minimum bias triggers should also be used to verify that the corrected measurement is the same after the corrections are re-evaluated. In all cases, the extracted distributions for the event sample should be robust against these changes.

Conclusion

Minimum bias events constitute the majority of the total cross section at the LHC. They are dominated by soft interactions with low transverse momentum and low particle multiplicity. At the LHC, minimum bias events will be studied with very early data (1–10 pb^{-1}), ideally during low-luminosity running, when the number of pp collisions per bunch crossing is less than or equal to 1. One of the first physics results from ATLAS will be the measurement of the central pseudorapidity density $\frac{\mathrm{d}N_{\mathrm{ch}}}{\mathrm{d}\eta}$ and transverse momentum spectrum $\frac{\mathrm{d}N_{\mathrm{ch}}}{\mathrm{d}p_T}$ of primary charged particles in minimum bias events at the LHC. These measurements, together with the invariant yield $E\frac{\mathrm{d}^3N_{\mathrm{ch}}}{\mathrm{d}^3p}$ of charged particles, have been the main topic of this dissertation.

Two trigger strategies for selecting inelastic collisions with as little bias as possible have been discussed: a random-based track trigger and a trigger using the Minimum Bias Trigger Scintillators. Both triggers are highly efficient at selecting the non-diffractive component of the inelastic cross section, but highly suppress the acceptance of the single-diffractive and double-diffractive components. This means that model-dependent corrections are required to compare ATLAS measurements to results from previous experiments.

A track-based method for reconstructing the charged particle distributions has been developed. The analysis uses the standard ATLAS simulation and reconstruction software and corrects for detector and reconstruction inefficiencies. The method has been exercised and validated using simulated data from the `mc09` validation. Results have been presented for an inelastic sample of 14,650

events, corresponding to an integrated luminosity of $\int \mathcal{L} \cdot \mathrm{d}t = 2 \times 10^{-7}$ pb^{-1}, or about 23 minutes of data-taking with a 10 Hz minimum bias trigger.

An extensive description of the systematic uncertainties associated with the measurements has also been given. Errors stemming from uncertainties on the characteristics of pp collisions at LHC energies, as well as on the detector efficiency and response, have been estimated. The largest of these uncertainties comes from the resolution of the track-to-vertex distance in the Inner Detector. The total systematic uncertainty on $\mathrm{d}N_{\mathrm{ch}}/\mathrm{d}\eta$ for the minimum bias event sample is estimated to be $^{+3.0}_{-2.3}$ % for $p_T > 0.15$ GeV/c. The total systematic uncertainty on $\mathrm{d}N_{\mathrm{ch}}/\mathrm{d}p_T$ for the same sample is estimated to be $^{+3.9}_{-2.6}$ % for $|\eta| < 2.5$. Ultimately, a detailed analysis of the actual data together with the studies presented here will give the best estimate of the systematic uncertainty on the measurement.

Because of the wide range in predictions at the LHC, this measurement uncertainty is sufficient to discriminate between the different models of minimum bias interactions. The measurements will also provide sufficient information to re-tune the event generators to better describe pp interactions at the LHC energy scale. The measurements studied here are thus an important first step to finding a model that describes the entire energy range up to the LHC.

Appendices

Appendix A

Event Sample

Simulated events used for this study were taken from a validation sample in preparation for the ATLAS `mc09` production. Non-diffractive, single-diffractive and double-diffractive inelastic pp collisions at $\sqrt{s} = 10$ TeV were generated with PYTHIA version 6.420, configured with the `mc09` 'ATLAS' tune parameter set as defined in [55]. Events were then simulated with GEANT4 and the ATLAS detector description `ATLAS-GEO-08-00-00`. Standard ATLAS software version 15.3.0.2 was used to reconstruct the simulated events. Low-p_T tracking was enabled by setting `InDetFlags.doLowPt = TRUE`. Table A.1 lists the reconstructed datasets used in this analysis, along with their parent datasets from the production.

The *inelastic event sample* was defined from a mixture of non-diffractive, single-diffractive and double-diffractive events. Relative cross sections among the three components correspond to those predicted by PYTHIA (see Table 2.1). The event sample consists of a total of 14,650 events, corresponding to an integrated luminosity of $\int \mathcal{L} \cdot \mathrm{d}t = 2 \times 10^{-7}$ pb^{-1}. The *minimum bias event sample* was defined as the subset of inelastic events passing the `MBTS_2` trigger (see Section 3.3). A total of 13,507 minimum bias events were accepted, corresponding to about 23 minutes of data-taking with a 10-Hz trigger.

Analysis of the reconstructed event sample was carried out entirely on Analysis Object Data (AOD) files, a highly-compressed data format suitable for most physics analyses [77]. The analysis presented here uses only the output of the Inner Detector reconstruction package `InDetRecExample` and the Minimum Bias Trigger Scintillators. No information from the calorimeter or muon system is needed.

Nº	**P. Nº**	**Dataset Name**
1		valid1.105001.pythia_minbias.evgen.EVNT.e380_tid039368
2		valid1.105003.pythia_sdiff.evgen.EVNT.e380_tid044121
3		valid1.105004.pythia_ddiff.evgen.EVNT.e380_tid044123
4	1	valid1.105001.pythia_minbias.simul.HITS.e380_s565_tid075773
5	2	valid1.105003.pythia_sdiff.simul.HITS.e380_s565_tid075887
6	3	valid1.105004.pythia_ddiff.simul.HITS.e380_s565_tid075886
7	4	valid1.105001.pythia_minbias.digit.RDO.e380_s565_tid075773
8	5	valid1.105003.pythia_sdiff.digit.RDO.e380_s565_tid075887
9	6	valid1.105004.pythia_ddiff.digit.RDO.e380_s565_tid075886
10	7	valid3.105001.pythia_minbias.recon.AOD.e380_s565_r744_tid078330
11	8	valid3.105003.pythia_sdiff.recon.AOD.e380_s565_r744_tid078333
12	9	valid3.105004.pythia_ddiff.recon.AOD.e380_s565_r744_tid078332

Table A.1: Inelastic datasets used in the analysis. P. Nº refers to the parent dataset number.

Appendix B

Invariant Cross Section

The invariant cross section $E\mathrm{d}^3\sigma/\mathrm{d}^3p$ is an important characteristic of collision processes since it determines the number of collisions occurring between beams of colliding particles. It is particularly useful for both experimentalists and theorists since d^3p/E remains invariant under Lorentz transformations.

For the purposes of the minimum bias analysis presented in Chapter 6, it is desirable to express the invariant cross section in terms of the measured track parameters η (see Equation 1.1) and p_T. To do so, we start by writing the invariant cross section as a function of the rapidity y (see Equation 1.2) and the transverse momentum p_T. Decomposing the momentum vector $\mathbf{p}$ in cylindrical coordinates, the invariant cross section becomes

$$E\frac{\mathrm{d}^3\sigma}{\mathrm{d}^3p} = E\frac{\mathrm{d}^3\sigma}{p_T\mathrm{d}p_T\mathrm{d}\phi\mathrm{d}p_z}. \tag{B.1}$$

A change of variables from p_z to y is made by substituting the identity $\mathrm{d}y/\mathrm{d}p_z = 1/E$ into Equation B.1:

$$E\frac{\mathrm{d}^3\sigma}{\mathrm{d}^3p} = \frac{\mathrm{d}^3\sigma}{p_T\mathrm{d}p_T\mathrm{d}\phi\mathrm{d}y}. \tag{B.2}$$

An additional change of variables from (y, p_T) to (η, p_T) is needed:

$$E\frac{\mathrm{d}^3\sigma}{\mathrm{d}^3p} = \frac{\mathrm{d}^3\sigma}{p_T\mathrm{d}p_T\mathrm{d}\phi\mathrm{d}\eta}\frac{\mathrm{d}\eta}{\mathrm{d}y}. \tag{B.3}$$

To calculate $\mathrm{d}y/\mathrm{d}\eta$, we first express η in terms of the momentum vector $\mathbf{p}$:

$$\eta = \frac{1}{2}\ln\left(\frac{|\mathbf{p}| + p_z}{|\mathbf{p}| - p_z}\right) \tag{B.4}$$

and then solve for e^{η} and $e^{-\eta}$:

$$e^{\eta} = \sqrt{\frac{|\mathbf{p}| + p_z}{|\mathbf{p}| - p_z}}, \tag{B.5}$$

$$e^{-\eta} = \sqrt{\frac{|\mathbf{p}| - p_z}{|\mathbf{p}| + p_z}}. \tag{B.6}$$

Adding Equations B.5 and B.6, we obtain the relation

$$|\mathbf{p}| = p_T\cosh\eta. \tag{B.7}$$

Subtracting Equation B.6 from B.5, we obtain instead

$$p_z = p_T\sinh\eta. \tag{B.8}$$

We substitute Equations B.7 and B.8 into Equation 1.2, using also $E^2 = p^2 + m^2$. Note that we have set $\hbar = c = 1$ here. We now have an expression for the rapidity y in terms of η and p_T:

$$y = \frac{1}{2}\ln\left[\frac{\sqrt{p_T^2\cosh\eta + m^2} + p_T\sinh\eta}{\sqrt{p_T^2\cosh^2\eta + m^2} - p_T\sinh\eta}\right]. \tag{B.9}$$

We then differentiate this expression with respect to η. The result, after some algebra, is:

$$\frac{\mathrm{d}y}{\mathrm{d}\eta} = \left[1 + \left(\frac{m}{p_T\cosh\eta}\right)^2\right]^{-1/2} \tag{B.10}$$

$$= \frac{p}{E}. \tag{B.11}$$

In the second line, we have used Equation B.7. Substituting Equation B.11 into Equation B.2, we obtain our final result:

$$E\frac{\mathrm{d}^3\sigma}{\mathrm{d}^3p} = \frac{E}{p}\frac{\mathrm{d}^3\sigma}{p_T\mathrm{d}p_T\mathrm{d}\phi\mathrm{d}\eta}, \tag{B.12}$$

where

$$\frac{E}{p} = \sqrt{1+\left(\frac{m}{p_T\cosh\eta}\right)^2}. \tag{B.13}$$

Appendix C

Pixel Detector Service Tests

The electrical services of the ATLAS pixel detector connect the detector to the external control, power, and acquisition systems. Services include all physical interfaces to the outside of ATLAS that provide the required energy input and control signals for operation of the detector. The design of these systems is described in detail in [109–118]. Any services responsible for transferring the acquisition data to the external readout system are not considered here.

Figure C.1 shows an overview of the service chain for the pixel detector. Given the scale and complexity of the system, a hardware and software package has been designed to qualify the full chain of services from the counting room (PP4) to the end of the pixel detector package (PP1) and back, including all interlock functionality. The package includes a comprehensive set of 'service tests', intended to be run on the entire service chain before it is considered safe to make any electrical connections to the detector at PP1. The set of service tests include basic continuity checks, PP4/PP1 measurement cross-checks and dynamic PP2 calibrations.

The service test package, including all tests, is described in detail in this appendix. Results of the tests on the fully-installed services in the ATLAS experimental cavern are also shown here.

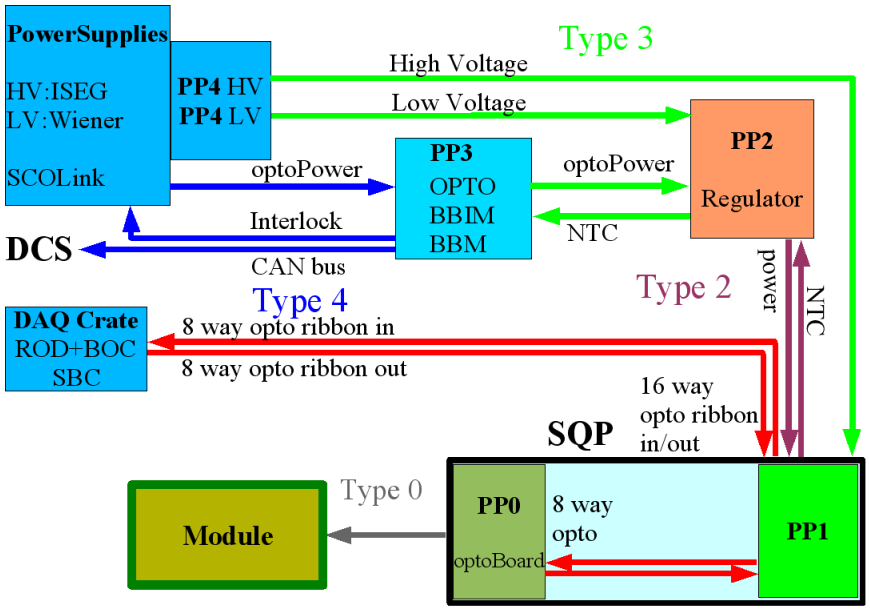

Figure C.1: Overview of the electrical services chain for the ATLAS pixel detector. The figure shows the routing of data links and power supply cables from each side of the pixel detector to the off-detector electronics and power supplies in the service caverns.

C.1 Prerequisites

The service tests described here assume that all individual components have been tested and installed, assuring full-functionality of all channels, and that the complete service chain is in place. This includes: low-voltage (LV) Wiener supplies, SC-OLink supplies, low-voltage PP4 active fan-outs, PP2 regulator crates, high-voltage (HV) ISeg supplies, high-voltage PP4 passive fan-outs, Building Block Matrix (BBM) crates, Building Block Interlock Matrix (BBIM) crates, interlock-matrix logic units, Bake-Out-Box (BOB) logic units, distribution boxes, and PP3-Opto crates.

An additional prerequisite for the service tests is the connectivity mapping of the as-built detector and service chain. This information is implemented in the System Integration Tool (SIT) of the Detector Control System (DCS). The SIT mapping tells DCS which individual hardware components are connected together along the chain and which detector components they provide services for. The SIT mapping can be derived from the connectivity database in a close-to-final form.

C.2 Hardware

Measurements for the service tests are made with GPIB[1]-enabled hardware located at PP1. The setup of the service test package allows testing the services of one Type-2 cable at a given time, for all three flavors: LV, HV and NTC/OPTO. The setup connects to the PP1-end of the Type-2 cables via the LEMO-F interface and steps through all channels using a series of switching matrices and termination loads. The tests for each of the flavors are described in the following sections. The natural procedure is to test all services belonging to two PP0 rows of the detector at a time.

Each LV Type-2 cable contains 7 VDD, 7 VDDA channels and 1 VVDC channel, all with remote sensing capability. Each HV Type-2 cable contains 26 VDET channels, as well as safety interlock pins. Each NTC/OPTO Type-2 cable contains 13 NTC_MOD, 2 NTC_OPTO, 2 VPin, 2 VISet and 2 OPTO_Reset channels. Pinouts for each of these cables can be found in [119]. The service test package can test each type of flavor statically, as well as the LV cable dynamically. The GPIB instruments used to make the measurements at PP1 are:

- 1 × Agilent N3300A System DC Electronic Load;
- 3 × Agilent N3302 load modules, 30 A at 60 V;
- 2 × Keithley 7001 Switch system;
- 1 × Keithley 2700 Multimeter/Data Acquisition system;
- 2 × Keithley 7011-S Quad 1 × 10 Multiplexer;
- 2 × Keithley 7166 1 × 10 Mercury Wetted Relay Card;
- 2 × Keithley 7708 40-channel thermocouple.

The 7708 switching cards are installed in the 2700 multimeter unit. One 7011 switching card and one 7166 are installed in each of the 7001 dedicated switching matrices. The three 3302 load modules are installed in the 3300 load mainframe.

[1] General Purpose Interface Bus

The channels of the switching boards are connected to either resistive loads or the programmable load modules and then to four pigtails with LEMO-F connectors: one LV female, one NTC/OPTO female and two HV male. The connectivity for each of the switching boards can be found in [119].

C.3 Software

The service test software is packaged inside the PVSS-II project `ATLASPixDCS_ServiceTest`. Service tests can be executed via the main user interface, which is written in the PVSS native language. Most of the functionality has been written into libraries specific to the service tests, with the exception of some methods which have been integrated into other `ATLASPixDCS` projects to ensure synchronization. This is particularly true in the case of PP2, where both software and hardware were continually evolving at a fast pace.

The `ServiceTest` project is able to communicate with the hardware components of the electrical services by connecting to the main DCS projects as a distributed system. In this way, the project can access all data point elements under test. The computer running the `ServiceTest` project must therefore be connected to the same network as the DCS machines. The project also needs to communicate with the GPIB-enabled devices listed in Section C.2. To do this from within PVSS, the necessary GPIB functionality is packaged into a 'Generic External Handler' library, which acts as a hook to add functions to the PVSS-II script language. The library, written in Microsoft Visual `C++`, defines a generic External Handler class, inherited from IT-COBE's `BasicExternHandler`, to facilitate implementation as a control DLL from within PVSS.

The only user input given to the program is the geographical address of the readout unit (i.e. sector or half-stave) for which the corresponding services are to be tested. The project then uses the SIT mapping defined in DCS to identify the connectivity of the off-detector components to this geographical address. Advantages of this scheme include simplicity at the user-end and integrated testing of the connectivity information in the SIT mapping and the connectivity database.

C.4 OPTO Tests

Opto channels of a Type-2 NTC/OPTO cable (2 × VPin, 2 × VIset, 2 × Opto_Reset) are terminated with 1 kΩ resistors. The six channels are routed through relay switches of one of the 7011 cards and a single output is sent to the Keithley 2700 multimeter unit for measuring voltage. There is no need for a realistic model of the cable beyond PP1 since the performance is not sensitive to resistance.

VPin and VIset channels are switched on at the SC-OLink to 10.0 V and 0.7 V, respectively; the Opto_Reset channel is always on as long as the SC-OLink is not interlocked. Voltage measurements are made with the 2700 at PP1 and compared to values read out from the SC-OLink. Presence of the Opto_Reset signal is verified by comparing the measured DC voltage to the expected value of 2.5 V. The expected value is used since the voltage of this channel is not measured by the SC-OLink. Expected currents are calculated from the GPIB voltage measurements and compared to values read out from the SC-OLink.

The OPTO tests cover failure of the VPin, VIset and Opto_Reset channels on the SC-OLink, discontinuous Type-3 or Type-2 cables, precision of voltage and current read back from the SC-OLink, and OPTO connectivity information in the SIT mapping. The remaining VVDC channel of the SC-OLink is dynmically tested by the LV tests. The OPTO tests do not test the dynamic properties of the Opto_Reset signal. The test takes about 1 minute per Type-2 cable.

PASS criteria:

- Voltage measured by GPIB for VPin and VIset channels must be within 5% of value read out from SC-OLink.
- Voltage measured by GPIB for Opto_Reset channels must be within 5% of 2.5 V.
- Current read out by SC-OLink for VPin and VIset channels must be within 5% of expected value (Measured voltage / 1 kΩ).

Figure C.2 shows the difference between the voltage measured at PP1 and the value read out by the SC-OLink at PP4, for VPin and VIset channels. The difference is primarily due to the voltage drop along the length of the Type-2 and Type-3 cables. Figure C.3 shows the difference between the measured voltage at PP1 and the expected voltage at the SC-OLink for Opto_Reset channels.

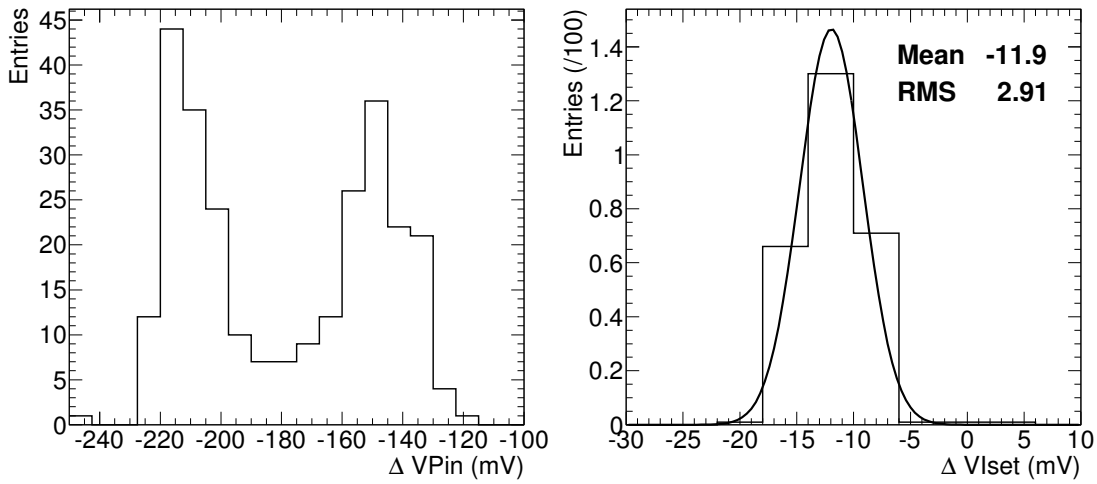

(a) (b)

Figure C.2: Voltage difference between PP1 and PP4 for VPin (a) and VIset (b) channels. Measurements at PP1 are made with the Service Test hardware; measurements at PP4 are made by the SC-OLink. The ΔVIset distribution has been fit with a Gaussian function.

C.5 NTC/Interlock Tests

NTC[2] channels of a Type-2 NTC/OPTO cable (13 × NTC_Mod, 2 × NTC_Opto) are terminated with 10 kΩ resistors, corresponding to a 'nominal' temperature of about 24.8 °C. The inverse relationship between the resistance of the sensor and the measured temperature is given by:

$$R_{\mathrm{NTC}} \quad = \quad 10 \cdot e^{3435(\frac{1}{T+273.15}-\frac{1}{298.15})}, \tag{C.1}$$

where T is the temperature in °C and R_{NTC} is given in kΩ. Each of the NTC channels are connected to a 1 × 20 block (2, 1 × 10 blocks with the outputs jacked) of one of the 7011 switching cards. A

[2]Negative Temperature Coefficient

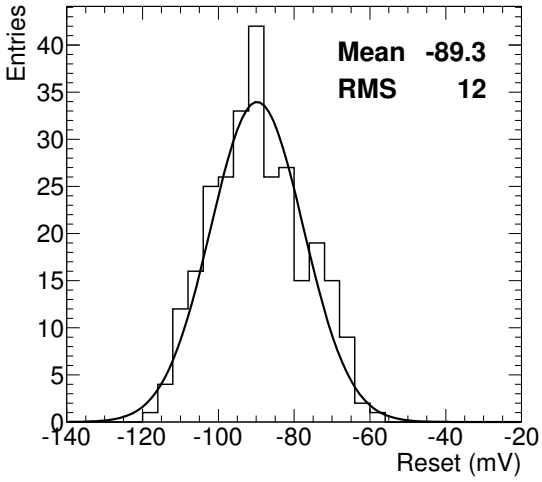

Figure C.3: Difference of voltage measured at PP1 and expected voltage at the SC-OLink for Opto_-Reset channels. Measurements at PP1 are made with the Service Test hardware. The expected voltage of 2.5 V is used here since no measurement is made by the SC-OLink for this channel. The distribution has been fit with a Gaussian function.

resistor of 12 kΩ sits at the output of this block and is added in parallel whenever a channel is closed. If a single channel is closed, the temperature rises to an 'overtemp' of 41.3 °C. This temperature is expected to trigger interlock action for the particular channel under test since it is above the shooting point temperature (40 °C) set at the BBIM. There is no need for a realistic model of the cable beyond PP1 since the performance is not sensitive to resistance.

NTC_Mod channels

For each channel, the NTC value is read out from the BBIM channel via DCS, testing continuity up to the BBIM. Interlocks for the corresponding LV Wiener channels are verified to be disabled and the appropriate ISeg channel is 'acknowledged' to clear any remaining interlocks. If the readout unit is located on the *b*-layer of the detector, the corresponding Bake-Out-Box (BOB) interlock is also verified to be disabled at the appropriate Logic Unit. If this initial connectivity test passes, the HV channels are ramped on to 10 V. The switch is then closed and, following a brief pause of about 2 seconds, the interlocks on the corresponding Wiener channels, BOB channel (if applicable)

and HV channel are checked to have properly interlocked. Finally, the 'overtemp' NTC value on the BBIM is read out.

NTC_Opto channels

For each channel, the NTC value is read out from the BBIM channel via DCS, testing continuity up to the BBIM. Since the SC-OLink does not have interlock monitoring capability, interlocks are checked manually by ramping on the power supply and checking that the voltage drops to zero after an interlock is triggered. The VPin, VIset and VVDC channels are turned on to 10, 0.7 and 6.0 V, respectively and voltages are read out from the SC-OLink to verify that the supply has indeed ramped on. If the initial connectivity test passes, the switch is closed. Following a pause of about 6 seconds, the voltages are again read out. Finally, the 'overtemp' NTC value on the BBIM is read out.

Top PP0s with 6 modules

In the case of 'top' PP0 rows (7 slots) populated only by 6-module sectors or half-staves, the spare channel should NOT cause an interlock when the switch is closed for that channel. This is verified by the 'special case' NTC/Interlock test. Since all channels are hard-wired to termination resistors, it is impossible to verify that the interlock is not enabled when this channel is disconnected.

The NTC/Interlock tests cover the complete interlock chain, from the NTC line at PP1 to the BBIM, to the logic unit and distribution box and finally to the power supplies. The Wiener supplies are not tested for false disables or enables (i.e. an attempt is not made to turn them on/off to check synchronization with their 'Inhibit' status). Low-temperature interlocks are not tested. The most frequent failures are missing readout temperatures caused by poor or broken connections at the NTC/OPTO PP2 interface, incorrect jumper settings at the Logic Unit and improper connections at the interlock input of the Wiener power supplies. The test takes about 6 minutes per Type-2 cable.

PASS criteria:

- All 'nominal' and 'overtemp' NTC values read out from DCS must be within 0.2 °C of expected values.
- NTC_Mod channels (not special case): Interlocks for Wiener, BOB (if *b*-layer PP0) and ISeg supply channels must be disabled at the 'nominal' NTC value and enabled at the 'overtemp' NTC value.
- NTC_Mod channels (special case): For any spare NTC channels, where the BBIM channel under test is not associated to a module on the PP0, the interlocks for Wiener, BOB (if *b*-layer PP0) and ISeg supply channels must be disabled at both 'nominal' and 'overtemp' NTC values.
- NTC_Opto channels: SC-OLink must power on at 'nominal' NTC value and power off when interlocked at the 'overtemp' NTC value.

Figure C.4 shows the NTC values read out for all NTC_Mod and NTC_Opto channels at nominal and overtemp conditions. Both distributions have been fit with Gaussian functions.

C.6 HV Tests

HV channels of a Type-2 HV cable (26 × VDet) are terminated with a voltage divider with a total load of 2.5 MΩ and then routed through a 7708 switching board. A scanning DVM Keithley 2700 is used to measure the voltage delivered across the load, with the measurement between VDet_-return and a 1 MΩ resistor. The purpose of the voltage divider is to ensure that the DVM always sees less than 300 V DC. The setup allows testing three Type-2 HV cables at any given time, using 3 × 26 (out of 80) channels of multiplexing. The electrical properties of the cable are not modeled beyond PP1 since the performance is not sensitive to resistance.

The HV tests check the behavior of HV channels under load conditions to make sure that all connections are present and that voltage and current are delivered correctly. Each channel on the

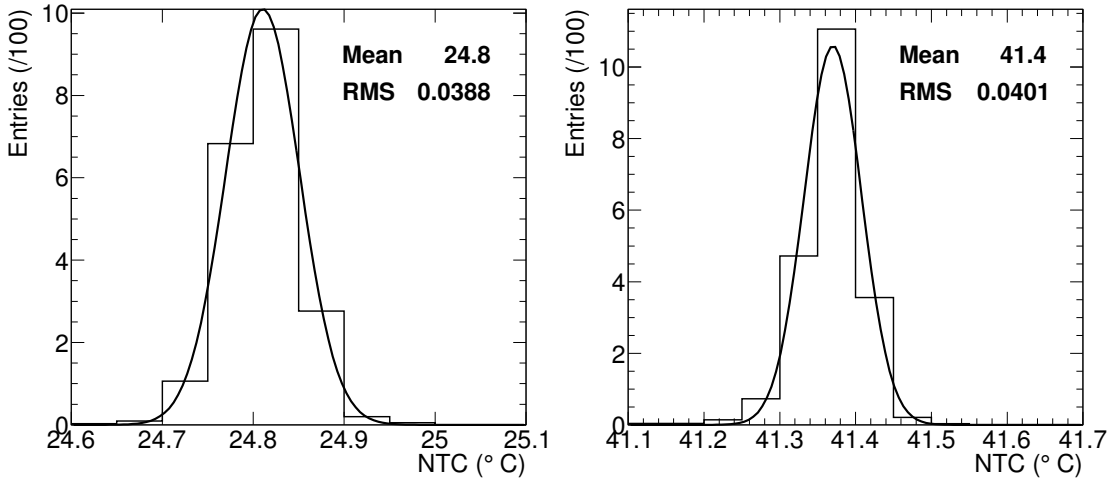

(a) (b)

Figure C.4: NTC temperatures read out at BBIM for NTC_Mod and NTC_Opto channels at nominal (a) and overtemp (b) values. Both distributions have been fit with Gaussian functions.

ISeg is ramped on to $V_{\text{set}} = 600$ V and the output of the voltage divider is measured with the DVM and compared to the expected voltage, approximately 0.366 times the set voltage. The current of each channel is also read out from the ISeg and compared to the expected value of (V_{set} / 2.5 MΩ) per module. This corresponds to 1.68 mA for an ISeg channel servicing a 7-module PP0 and 1.44 mA for a channel servicing a 6-module PP0.

The possibility to 'burn-in' the ISeg power supplies is also supported by the Service Test package since the hardware implementation of the service test package enables a load on every connected channel. However, it is not possible to measure small leakage current because of the background current from the 2.5 MΩ load resistance.

The HV tests cover continuity from the ISeg, to the HV-PP4 passive fanout and through the Type-2 cable. Operation up to the maximum supply voltage of 700 V is possible, giving about 0.3 mA per HV line, or a worst case of 2.1 mA per ISeg channel. This is still safely below the 4 mA current limit of the ISeg channel. Trip conditions in the power supply are not tested. A quick

connectivity test of a Type-2 HV cable takes about 2 minutes. Burn-in can be requested by the user for variable lengths of time.

PASS criteria:

- Voltage measured by GPIB must be within 5% of expected value. The expected value is about $0.366 \times V_{\text{set}}$, a number determined experimentally using the setup in SR1. This value also worked well in the cavern, despite the wide range of Type-2 HV cable lengths (50–80 m).
- Current values read out from the ISeg must be within 5% of expected values: 1.44 mA for an ISeg channel servicing a 6-module PP0, or 1.68 mA for a channel servicing a 7-module PP0.

Figure C.5 shows the measured voltage at PP1 for all HV channels. The distribution has been fit with a Gaussian function. The (relatively) large width of the Gaussian is due to the various Type-2 cable lengths, ranging from 50 to 80 m.

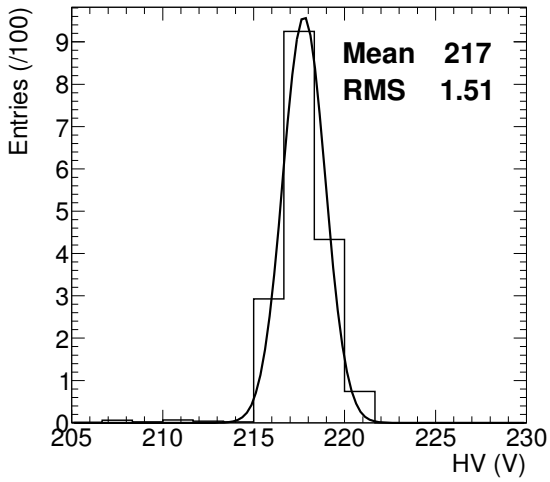

Figure C.5: Voltage measured at PP1 for HV channels. The distribution has been fit with a Gaussian function. The large width of this Gaussian is due to the various Type-2 HV cable lengths, ranging from 50 to 80 m.

C.7 LV Tests

Remote-sensing channels of a Type-2 LV cable (7 × VDD, 7 × VDDA, 1 × VVDC) are connected to three channels of the programmable load. Here, the load generator also doubles as the measuring unit. The multiplexing is done using both of the 7001 switching matrices. The supply and return connections are connected to low-resistance mercury relays (7166 board with 10 DPST[3] relays and 100 mΩ on-resistance) configured to be independent of each other. The sense connections are multiplexed using a higher-density card (7011S quad 1 × 10 DPST card). Each of the sense lines (high-side and low-side) pass through their own relays to allow breaking individual connections as needed. The setup also simulates the approximate electrical behavior of the Type-1 (Service Panel) and Type-0 cables, with the remote sense connection made at the end of the 'Type-0 cable' (i.e. at the load). The additional resistance is 0.3 Ω each way for power channels and 1.32 Ω each way for sense channels.

The LV tests are divided into five separate tests that can be run individually or in any combination determined by the user:

- The **Trimmer** test verifies that each PP2 regulator channel is delivering the proper voltage to the load and that the current compensation potentiometer of the regulator is adjusted properly. It also cross-checks PP4 current measurements with readings from the load.
- The **Vmon** and **Imon** tests calibrate PP2 ADC readings for the output voltage and current of the regulator channel using measurements taken by the programmable load.
- The **Diode** test checks the static and dynamic behavior of the protection circuits in the regulator by opening individual sense lines.
- The **Dynamic** test checks the transient behavior of a set of regulator channels by monitoring the output voltage following a series of steps in the load current.

[3]Double Pole, Single Throw

All tests start by turning on the appropriate Wiener and SC-OLink power supply channels. The VVDC 'opto' channel of the PP0 is tested first (Ch f on the PP2 board). The channel remains on while the test loops over all 'modules' of the same PP0, represented by a pair of regulator channels corresponding to the VDD and VDDA supply for one module.

C.7.1 LV Trimmer test

The LV Trimmer test sets the output voltage of a PP2 regulator channel to a nominal value by adjusting its 'trimmer' position. The relation between trimmer position (an integer from 0 to 99) and output voltage can be parameterized by:

$$U = \frac{r}{(s - \text{trimmer}) + t}, \tag{C.2}$$

where U is the output voltage in V. The fit for r, s, and t is performed at INFN-Milano during the production tests and saved into a calibration file. The Trimmer test assumes that this file has been properly loaded into DCS.

The Trimmer test uses the calibration from Milano to set the trimmer of the regulator channel to the nominal output voltage: 2.1 (2.0) V for VDD, 1.7 (1.6) V for VDDA of barrel (disk) modules and 2.5 V for VVDC. The active load is set to draw a constant current of 750/1200/400 mA for VDD/VDDA/VVDC channels. The output voltage is measured by the load and, if necessary, the trimmer is moved in small increments until the nominal voltage is reached to within ±10 mV. Once the nominal trimmer value is found, it is stored in the `DefaultTrimmerPos` data point element of the regulator channel so that it can later be retrieved if trimmer settings are ever changed or reset.

The regulator channel is then power cycled and the output voltage is re-measured. Current at PP4 is read out from LV-PP4 (VDD/VDDA channels) or from the SC-OLink (VVDC channels). The current compensation behavior of the regulator channel is then tested by measuring the voltage at the load for two values of the load current: 100 and 1000 mA for VDD, 100 and 1300 mA for

VDDA, and 100 and 500 mA for VVDC. The LV Trimmer test takes about 9 minutes per Type-2 cable.

PASS criteria:

- Trimmer calibration must find a trimmer position within ±10 mV of the nominal voltage.
- Output voltage must be within ±10 mV of the nominal voltage.
- Current read out from LV-PP4 must be within 5% of the current measured at the load.
- Output voltages measured at two high/low current values must be within 50 mV of each other.

Figure C.6(a) shows the number of additional trimmer steps needed to properly calibrate the PP2 VDD/VDDA/VVDC channels in the cavern, starting from the trimmer curve parameterization given in the calibration file from Milano. Most regulator channels required no trimmer adjustment from the position calculated with the Milano parameterization. A small fraction of channels required a +1 adjustment. This shows that the current compensation potentiometer is properly tuned for the Service Test setup.

Figure C.6(b) shows the deviation of the output voltage as measured by the programmable load from nominal, for VDD/VDDA/VVDC channels. All channels have output voltages within ±10 mV of the nominal value.

Figure C.6(c) shows the difference in the voltage measured at the load for high and low currents. The regulator channels show good current compensation behavior since there is only an average of ±15 mV difference between high and low currents.

Figure C.6(d) shows the difference between the current measured at the load and the current read out from PP4. LV PP4 current readings show a slight systematic offset from the current measured at PP1.

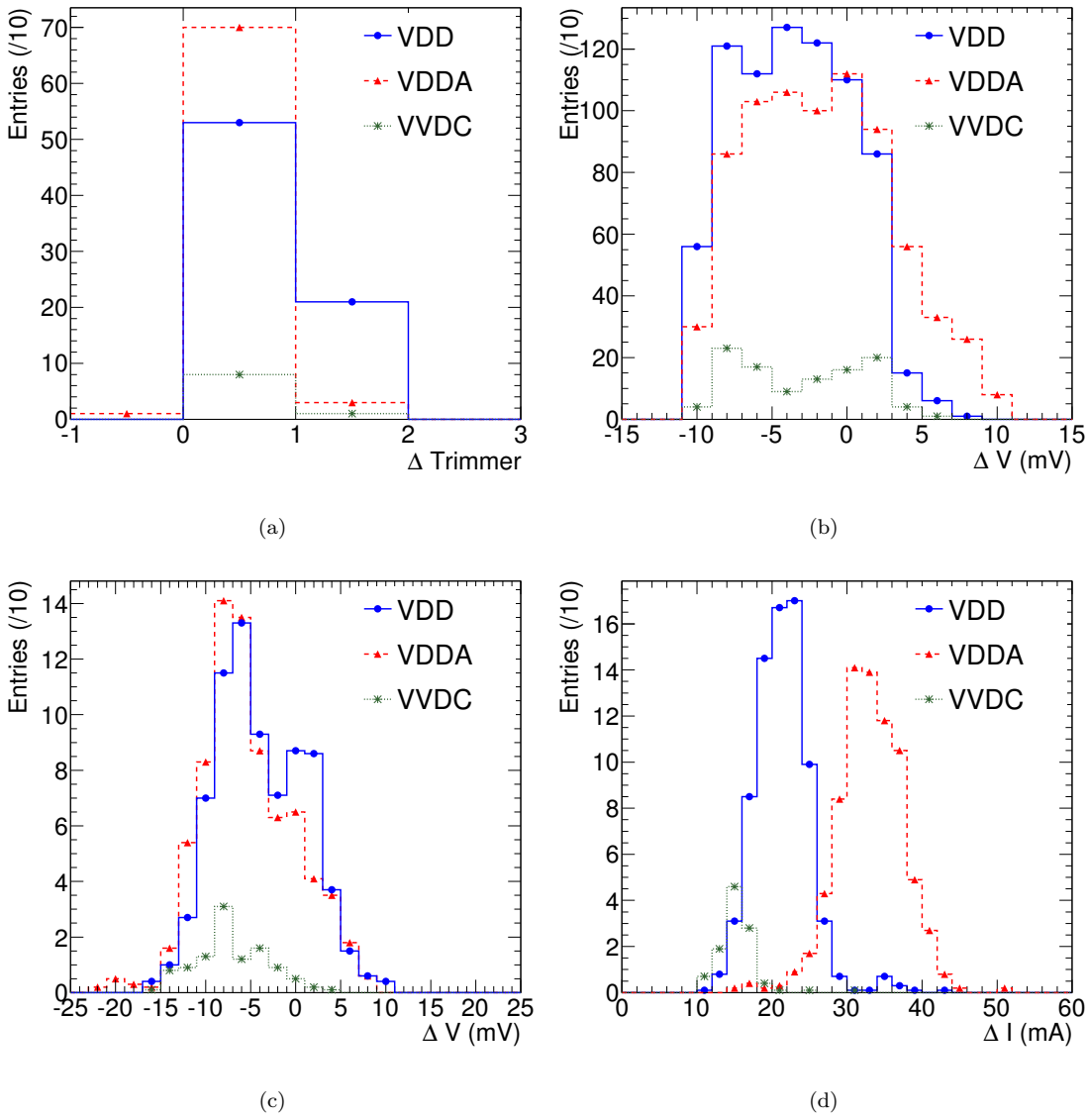

Figure C.6: Results of LV Trimmer tests for VDD (blue circles), VDDA (red triangles) and VVDC (green asterisks) channels. (a) Number of additional trimmer steps needed to properly calibrate each of the PP2 regulator channels. (b) Deviation of output voltage measured at the load from nominal, following calibration. (c) Difference in the voltage measured at the load for high and low load currents. (d) Difference between the current measured at the load and the current read out from PP4.

C.7.2 LV Vmon test

The LV Vmon test uses the Milano configuration file to set the trimmer position of the regulator channel to two output voltages centered around the nominal voltage (±100 mV). The load is set to draw a constant current of 750/1200/400 mA for VDD/VDDA/VVDC channels. At both set voltages, ADC values are read out from the `PDO.Value` data point element of the regulator channel and the output voltage is measured at the load. Five ADC readings are averaged and the Vmon curve is fit with a line. The slope and offset of this line are stored in the polynomial message conversion of the Vmon data point element.

The trimmer value is then reset to its nominal value. Output voltage is measured at the load and the calibrated Vmon from DCS is read out. To check any dependence of the Vmon on the load current, two readings are taken at two different current points. The same current points are used as in the current compensation test of Section C.7.1 to be able to correlate the two tests in a later analysis of the data. The LV Vmon test takes about 13 minutes per Type-2 cable.

PASS criteria:

- Vmon calibration must find suitable parameters to fit the Vmon versus output voltage curve.
- Calibrated Vmon reading must be within ±50 mV of the output voltage measured at the load for the nominal current value of 750/1200/400 mA (VDD/VDDA/VVDC channels).
- Vmon readings at high (configured) and low (un-configured) current values must be within 50 mV of each other.

Figure C.7 shows the difference between the PP2 channel Vmon reading and the actual voltage measured at the load located at PP1. All channels are calibrated to within ±50 mV of the measured voltage.

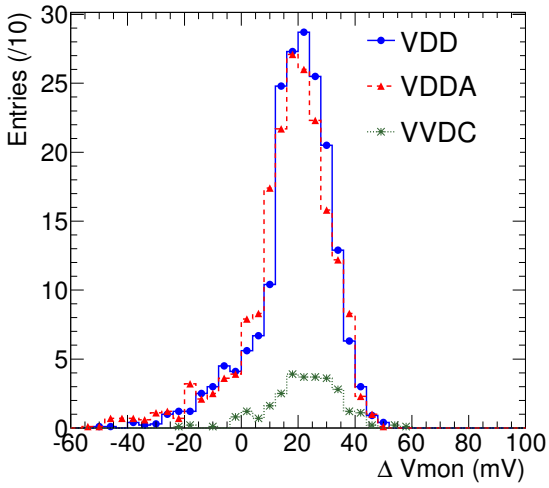

Figure C.7: Difference between the Vmon value read out from the PP2 regulator channel and the actual voltage measured at the load at PP1. The distribution shows that all channels are calibrated properly to within a 50 mV tolerance.

C.7.3 LV Imon test

The LV Imon test sets the active load to draw two currents: 300 and 900 mA for VDD, 400 and 1300 mA for VDDA, and 200 and 500 mA for VVDC channels. At both load currents, ADC values are read out from the `PDO.PDO3.Value` data point element of the regulator channel and the current is measured at the load. Five ADC readings are averaged and the Imon curve is fit with a line. The slope and offset of this line are stored in the polynomial message conversion of the Imon data point element. The R_{Load} value is set to 1 Ω.

The load current is then reset to its nominal current value of 750/1200/400 mA for VDD/VDDA/VVDC channels. Current is measured at the load and the calibrated Imon from DCS is read out. The test takes about 11 minutes per Type-2 cable.

PASS criteria:

- Imon calibration must find suitable parameters to properly fit the Imon versus load current curve.

- Calibrated Imon reading must be within ±30 mA of the current measured at the load for the nominal voltage values of 2.1 (2.0) V for VDD, 1.7 (1.6) V for VDDA of barrel (disk) modules and 2.5 V for VVDC.

Figure C.8 shows the difference between the PP2 channel Imon reading and the actual current measured at the load located at PP1. All channels are calibrated to within ±30 mA of the measured current.

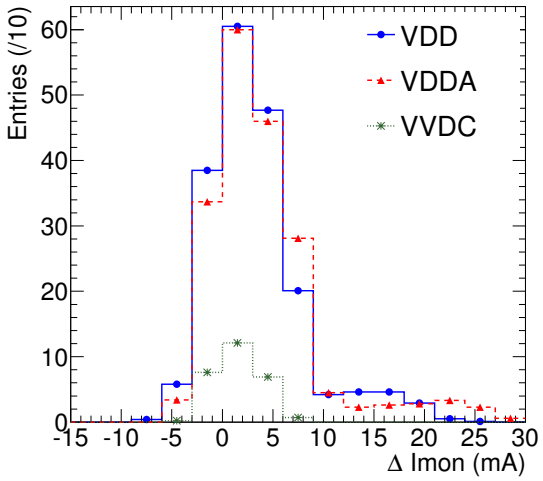

Figure C.8: Difference between the Imon value read out from the PP2 regulator channel and the actual voltage measured at the load at PP1. The distribution shows that all channels are calibrated properly to within a 30 mA tolerance.

C.7.4 LV Diode test

The LV Diode test sets the active load to draw nominal currents (750/1200/400 mA for VDD/VDDA/VVDC channels) and measures four voltages at the load: one with both sense lines closed, one with the high-side sense line open, one with the low-side sense line open and one with both sense lines open. The test can also run in a 'low-current' mode, with nominal currents reduced to values typical of unconfigured modules and opto-boards. The test takes about 4 minutes per Type-2 cable.

PASS criteria:

- Output voltage of regulator channel with both sense lines closed (V_0) must be within ± 10 mV of nominal voltage.
- Output voltage of regulator channel with high sense line open must be less than ($V_0 + 1.9$ V) but greater than ($V_0 + 0.01$ V).
- Output voltage of regulator channel with low sense line open must be less than ($V_0 + 1.4$ V) but greater than ($V_0 + 0.01$ V).
- Output voltage of regulator channel with both sense lines open must be less than ($V_0 + 2.0$ V) but greater than ($V_0 + 0.01$ V).

Figure C.9 shows the difference in the measured voltage for each of the open sense line cases described above.

C.7.5 LV Dynamic tests

The LV Dynamic test checks the transient voltage behavior of the PP2 regulator. Three channels can be tested simultaneously: two channels corresponding to the VDD/VDDA for a particular module and the associated VVDC channel. The load is first set to draw a constant current of 100 mA for all channels. A current step is applied to each of the channels one-by-one while measuring the output voltage of all channels at intervals of 10 μs. The 'configured' current values used are 800/1200/500 mA for VDD/VDDA/VVDC channels. The slew rate is set to 10 kA/s. A 10 μF capacitor is added in series to the load in order to mimic the capacitance of the modules and optoboard.

The transient pulse shape can be characterized by calculating the size of the overshoot and the recovery time. The LV Dynamic test is not performed on all channels by default, but only on request from the user. No **PASS** criteria have been defined for this test. Figure C.10 shows the results of an example dynamic test on a set of three regulator channels.

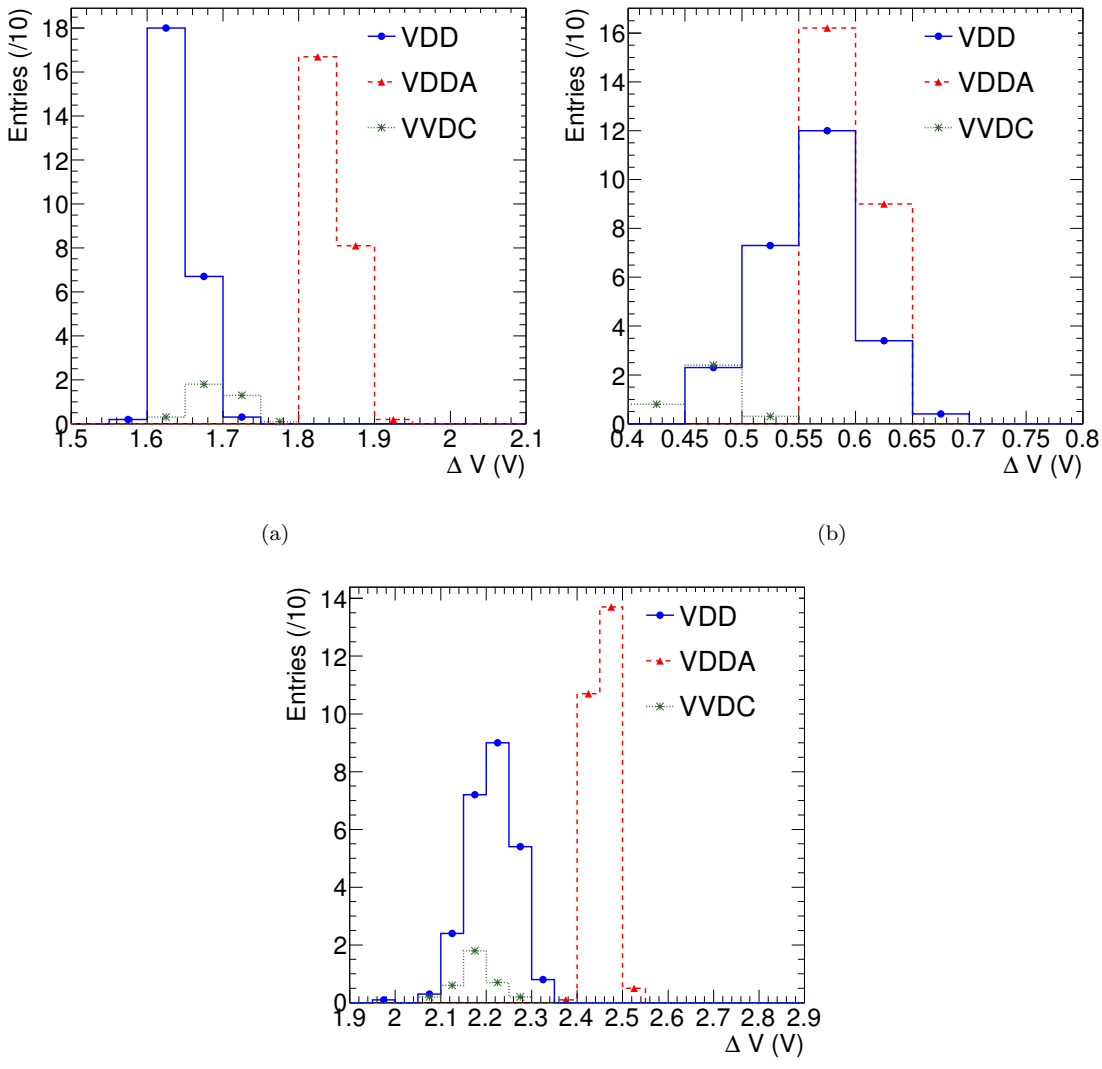

Figure C.9: Difference in the measured voltage at the load from nominal when the high sense line (a), low sense line (b) and both sense lines (c) is/are opened.

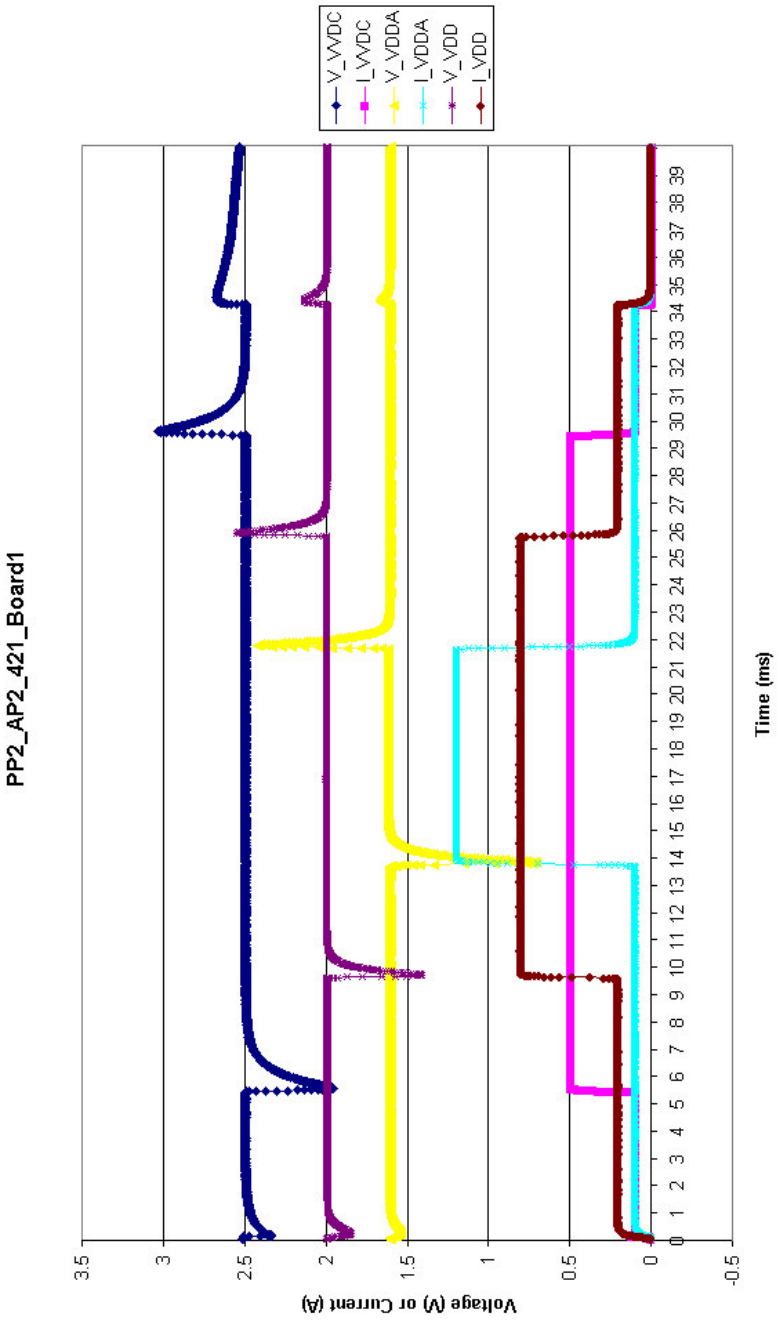

Figure C.10: Results from an LV Dynamic test on three regulator channels corresponding to the VDD and VDDA channels of one module and the VDDC channel for the corresponding optoboard. The plot shows the transient pulse shape after configuring and unconfiguring the module and optoboard.

C.8 Limitations

C.8.1 Untested Services

The following is a list of electrical services that are not tested by the Service Test package:

- Environmental LEMO-F cables and corresponding BBM channels
- Opto Heater LEMO-F cables
- Vref ADC readings for PP2 temperatures
- PP1 and BOC interlocks
- PP2 temperature interlocks
- DSS interlocks

C.8.2 Failure Analysis

It is important to note any potential problems that the service tests are blind to. The most serious are the low temperature interlocks and false enables/disables of the Wiener supply. This includes cases where the 'Inhibit' status of the Wiener supply does not have the intended effect on the on/off state of the channel. Other possible failures involve errors in the SIT mapping since the program relies heavily on this for connectivity information.

Case A: Suppose that a particular 'top' PP0 row is connected to a sector or half-stave with only six modules. The PP0 slots are intended to be populated in a standard way according to the connectivity database. However, a broken trace on one of the slots requires shifting one of the modules to a different slot. The SIT mapping and the jumpers for the corresponding logic unit do not reflect this switch since they were derived from a previous version of the connectivity database. Since the service test program is unaware of the switch, it verifies that six out of seven of the BBIM channels for the PP0 row cause an interlock and that the remaining channel does not

(see Section C.5: 'Top PP0s with 6 modules'). However, the PP0 row is not actually populated in this manner and instead, one of the unused BBIM channels causes an interlock and one of the used channels does not. If an interlock were ever to occur during detector operation on this channel only, the power supply for this PP0 would not switch off and the module would be at risk of overheating.

Bibliography

[1] P. Lefèvre and T. Pettersson. The Large Hadron Collider: Conceptual Design. Technical Report CERN-AC-95-05-LHC, CERN, Geneva, Switzerland, 1995.

[2] L. Evans et al. LHC Machine. *JINST*, 3:S08001, 2008.

[3] ATLAS Collaboration and G. Aad et al. Expected Performance of the ATLAS Experiment, Detector, Trigger and Physics. arXiv:0901.0512 [hep-ex], December 2008.

[4] CERN News, July 2009. `http://user.web.cern.ch/user/news/2009/090716.html`.

[5] ATLAS Collaboration and W. Armstrong et al. ATLAS: Technical Proposal for a General-Purpose *pp* Experiment at the Large Hadron Collider at CERN. Technical Report CERN/LHCC/94-43, CERN, Geneva, Switzerland, 1994.

[6] ATLAS Collaboration and G. Aad et al. The ATLAS Experiment at the CERN Large Hadron Collider. *JINST*, 3:S08003, 2008.

[7] CMS Collaboration. CMS Technical Proposal. Technical Report CERN/LHCC/94-38, CERN, Geneva, Switzerland, 1994.

[8] CMS Collaboration and S. Chatrchyan et al. The CMS Experiment at the CERN LHC. *JINST*, 3:S08004, 2008.

[9] LHCb Collaboration and S. Amato et al. LHCb Technical Proposal. Technical Report CERN/LHCC/98-4, CERN, Geneva, Switzerland, 1998.

[10] LHCb Collaboration and A. Augusto Alves Jr. et al. The LHCb Detector at the LHC. *JINST*, 3:S08005, 2008.

[11] ALICE Collaboration and N. Ahmad et al. A Large Ion Collider Experiment: Technical Proposal. Technical Report CERN/LHCC/95-71, CERN, Geneva, Switzerland, 1995.

[12] ALICE Collaboration and K. Aamodt et al. The ALICE Experiment at the CERN LHC. *JINST*, 3:S08002, 2008.

[13] ATLAS Inner Detector Collaboration. ATLAS Inner Detector Technical Design Report. Technical Report CERN/LHCC/97-16&17, CERN, Geneva, Switzerland, 1997.

[14] J. Weingarten. Results from the Commissioning of the ATLAS Pixel Detector with Cosmics Data. Technical Report ATL-INDET-PROC-2009-008, ATL-COM-INDET-2009-021, CERN, Geneva, Switzerland, 2009.

[15] T. Cornelissen. *Track Fitting in the ATLAS Experiment*. PhD thesis, NIKHEF, 2006.

[16] M. Vos. *The ATLAS Inner Tracker and the Detection of Light Super-Symmetric Higgs Bosons*. PhD thesis, 2003.

[17] ATLAS LAr Unit. Liquid Argon Calorimeter Technical Design Report. Technical Report CERN/LHCC/96-41, CERN, Geneva, Switzerland, 1996.

[18] ATLAS Tile Calorimeter Collaboration. Tile Calorimeter Technical Design Report. Technical Report CERN/LHCC/96-42, CERN, Geneva, Switzerland, 1996.

[19] ATLAS Muon Collaboration. ATLAS Muon Spectrometer Technical Design Report. Technical Report CERN/LHCC/97-22, CERN, Geneva, Switzerland, 1997.

[20] ATLAS Collaboration. ATLAS Detector and Physics Performance Technical Design Report. Technical Report CERN/LHCC/99-14&15, CERN, Geneva, Switzerland, 1999.

[21] ATLAS Level-1 Trigger Group. Level-1 Trigger Technical Design Report. Technical Report CERN/LHCC/98-14, CERN, Geneva, Switzerland, 1998.

[22] ATLAS HLT/DAQ/DCS Group. ATLAS High Level Trigger, Data Acquisition and Controls Technical Design Report. Technical Report CERN/LHCC/2003-022, CERN, Geneva, Switzerland, 2003.

[23] A. Moraes, C. Buttar, and I. Dawson. Prediction for Minimum Bias and the Underlying Event at LHC Energies. *Eur. Phys. J. C*, 50:435, 2007.

[24] M. Peskin and D. Schroeder. *An Introduction to Quantum Field Theory*. Perseus Books, 1995.

[25] F. Mandl and G. Shaw. *Quantum Field Theory*. Wiley, 1993.

[26] F. Halzen and A. Martin. *Quarks and Leptons: An Introductory Course in Modern Particle Physics*. Wiley, 1984.

[27] J. D. Bjorken. Asymptotic Sum Rules at Infinite Momentum. *Phys. Rev.*, 179(5):1547–1553, March 1969.

[28] P. D. B. Collins and A. D. Martin. *Rep. Prog. Phys.*, 45:335, 1982.

[29] P. D. B. Collins and A. D. Martin. *Hadron Interactions*. Adam Hilger, Bristol, 1984.

[30] T. Akesson et al. Double parton scattering in pp collisions at $\sqrt{s} = 63$ GeV. *Z. Phys. C*, 34:163, 1987.

[31] J. Alitti et al. A study of multi-jet events at the CERN $\bar{p}p$ collider and a search for double parton scattering. *Phys. Lett. B*, 268:145, 1991.

[32] F. Abe et al. Study of four jet events and evidence for double parton interactions in $p\bar{p}$ collisions at $\sqrt{s} = 1.8$ TeV. *Phys. Rev. D*, 47:4857, 1993.

[33] F. Abe et al. Measurement of Double Parton Scattering in $p\bar{p}$ collisions at $\sqrt{s} = 1.8$ TeV. *Phys. Rev. Lett.*, 79:584, 1997.

[34] F. Abe et al. Measurement of Double Parton Scattering in $p\bar{p}$ collisions at $\sqrt{s} = 1.8$ TeV. *Phys. Rev. D*, 56:3811, 1997.

[35] T. Sjöstrand and M. van Zijl. *Phys. Rev. D*, 36:2019, 1987.

[36] A. Capella et al. *Phys. Lett. B*, 81:68, 1979.

[37] A. Capella and J. T. T. Van. *Phys. Lett. B*, 93:146, 1980.

[38] A. Capella and J. T. T. Van. *Z. Phys. C*, 10:249, 1981.

[39] A. Capella et al. *Phys. Rep.*, 236:225, 1994.

[40] T. Sjöstrand. *Comput. Phys. Commun.*, 82:74, 1994.

[41] T. Sjöstrand et al. *Comput. Phys. Commun.*, 135:238, 2001.

[42] T. Sjöstrand, S. Mrenna, and P. Skands. PYTHIA 6.4 Physics and Manual. *JHEP*, 05:026, 2006.

[43] T. Sjöstrand and P. Z. Skands. *JHEP*, 03:053, 2004.

[44] T. Sjöstrand and P. Z. Skands. Transverse-momentum-ordered showers and interleaved multiple interactions. *Eur. Phys. J. C*, 39:129, 2005.

[45] R. Engel. PHOJET manual (program version 1.05c, June 96). `http://www-ik1.fzk.de/ẽngel/phojet.html`.

[46] R. Engel. *Z. Phys. C*, 66:203, 1995.

[47] A. Breakstone et al. Charged multiplicity distribution in *pp* interactions at CERN ISR energies. *Phys. Rev. D*, 30:528, 1984.

[48] G. J. Alner. *Phys. Rep.*, 154:247, 1987.

[49] R. E. Ansorge et al. Charged particle correlations in anti-p p collisions at c.m. energies of 200 GeV, 546 GeV and 900 GeV. *Z. Phys.*, C37:191–213, 1988.

[50] R. E. Ansorge et al. *Z. Phys. C*, 43:357, 1989.

[51] F. Abe et al. Transverse-momentum distributions of charged particles produced in $\bar{p}p$ interactions at $\sqrt{s} = 630$ GeV and 1800 GeV. *Phys. Rev.*, 61:1819–1822, 1988.

[52] F. Abe et al. Pseudorapidity distributions of charged particles produced in $\bar{p}p$ interactions at $\sqrt{s} = 630$ GeV and 1800 GeV. *Phys. Rev.*, D41:2330, 1990.

[53] T. Alexopoulos et al. *Phys. Lett. B*, 435:453, 1998.

[54] S. G. Matinyan and W. D. Walker. *Phys. Rev. D*, 59:034022, 1999.

[55] M. Warsinsky. Summary of ATLAS Pythia tune for MC09. Talk given at the ATLAS Monte Carlo Generator Meeting, CERN, June 2009.

[56] G. A. Schuler and T. Sjöstrand. *Phys. Rev. D*, 49:2257, 1994.

[57] R. Field. Min-Bias at the Tevatron. Technical Report CDF/PUB/MIN_BIAS/PUBLIC/8876, FermiLab, Chicago, USA, 2007.

[58] M. Deile. Diffraction and Total Cross-Section at the Tevatron and the LHC. In *Proceedings of the Hadron Collider Physics Symposium*, July 2005.

[59] A. Donnachie and P. V. Landshorff. *Phys. Lett. B*, 296:227, 1992.

[60] M. M. Block and R. N. Cahn. *Rev. Mod. Phys.*, 57:563, 1985.

[61] K. Hahn and J. Ranft. *Phys. Rev. D*, 41:1463, 1990.

[62] J. R. Forshaw and D. A. Ross. *Quantum Chromodynamics and the Pomeron.* Cambridge, 1997.

[63] K. Igi and M. Ishida. *Phys. Lett. B*, 622:286, 2005.

[64] R. Field. Talk given at the Workshop on Advanced Monte-Carlo Use and Tuning at CMS, CERN, December 2008.

[65] R. Assmann, C. Fischer, and D. Macina. Integration of Tertiary Collimators, Beam-Beam Rate Monitors and Space Reservation for a Calorimeter in the Experimental LSS's. Technical Report LHC-LJ-EC-0003, CERN, Geneva, Switzerland, 2004.

[66] R. Spiwoks et al. The ATLAS Level-1 Central Trigger Processor (CTP). Technical Report ATL-DAQ-CONF-2005-030, CERN, Geneva, Switzerland, 2005.

[67] R. Kwee. Studies for the Development of a Minimum Bias Trigger at Low Luminosities in the ATLAS Experiment at the Large Hadron Collider. Master's thesis, Humboldt Universität zu Berlin, 2007.

[68] R. Kwee. Minimum Bias Triggers at ATLAS, LHC. arXiv:0812.0613 [hep-ex], December 2008.

[69] E. Feng and J. E. Pilcher. Triggering ATLAS with Minimum Bias Trigger Scintillators. Technical Report ATL-COM-TILECAL-2007-013, CERN, Geneva, Switzerland, 2007.

[70] A. Artikov, D. Chokheli, J. Huston, B. Miller, and M. Nessi. Minimum Bias Scintillator Counter Geometry. Technical Report AT-GE-ES-0001, CERN, Geneva, Switzerland, 2004.

[71] W. H. Bell. Minimum Bias Physics at the LHC with the ATLAS Detector. Technical Report ATL-COM-PHYS-2009-156, CERN, Geneva, Switzerland, 2009.

[72] P. Jenni and M. Nessi. ATLAS Forward Detectors for Luminosity Measurement and Monitoring. Technical Report CERN-LHCC-2004-010, LHCC-I-014, CERN, Geneva, Switzerland, 2004.

[73] M. Bruschi. The ATLAS Luminosity Monitor. Technical Report ATL-COM-LUM-2009-006, CERN, Geneva, Switzerland, 2009.

[74] P. Jenni et al. Zero Degree Calorimeters for ATLAS. Technical Report CERN-LHCC-2007-001, CERN, Geneva, Switzerland, 2007.

[75] S. Ask. Simulation of Luminosity Monitoring in ATLAS. Technical Report ATL-LUM-PUB-2006-001, CERN, Geneva, Switzerland, 2006.

[76] T. Cornelissen, M. Elsing, S. Fleischmann, I. Garvilenko, W. Liebig, E. Moyse, and A. Salzburger. Concepts, Design and Implementation of the ATLAS New Tracking (NEWT). Technical Report ATL-SOFT-PUB-2007-007, CERN, Geneva, Switzerland, 2007.

[77] P. F. kesson et al. ATLAS Tracking Event Data Model. Technical Report ATL-SOFT-PUB-2006-004, CERN, Geneva, Switzerland, 2006.

[78] A. Salzburger, S. Todorova, and M. Wolter. The ATLAS Tracking Geometry Description. Technical Report ATL-SOFT-PUB-2007-004, CERN, Geneva, Switzerland, 2007.

[79] T. Cornelissen, M. Elsing, I. Garvilenko, W. Liebig, and A. Salzburger. Single Track Performance of the Inner Detector New Track Reconstruction (NEWT). Technical Report ATL-INDET-PUB-2008-002, CERN, Geneva, Switzerland, 2008.

[80] D. Wicke. A New Algorithm for Solving Track Ambiguities. Technical Report DELPHI 98-163 PROG 236 TRACK 92, CERN, Geneva, Switzerland, 1998.

[81] I. Gavrilenko. Description of Global Pattern Recognition Program (xKalman). Technical Report ATL-INDET-97-165, CERN, Geneva, Switzerland, 1997.

[82] R. Duda and P. Hart. Use of the Hough Transformation to Detect Lines and Curves in Pictures. *Comm. ACM*, 15, 1972.

[83] R. Frühwirth et al. Application of Kalman Filtering to Track and Vertex Fitting. *Nucl. Instrum. Meth.*, A262:444, 1987.

[84] A. Salzburger. The ATLAS Track Extrapolation Package. Technical Report ATL-SOFT-PUB-2007-005, CERN, Geneva, Switzerland, 2007.

[85] R. Frühwirth, T. Todorov, and M. Winkler. Estimation of Detector Alignment Parameters using the Kalman Fitter with Annealing. *Journal of Physics G: Nuclear and Particle Physics*, 29, 2003.

[86] R. Frühwirth and A. Strandlie. Track Finding and Fitting with the Gaussian-Sum Filter. In *Proceedings of Computing in High Energy Physics*, September 1998.

[87] R. Frühwirth, A. Strandlie, T. Todorov, and M. Winkler. Recent Results on Adaptive Track and Multitrack Fitting. *Nucl. Instr. Meth.*, 502, 2003.

[88] S. Fleischmann. *Track Reconstruction in the ATLAS Experiment: The Deterministic Annealing Filter*. PhD thesis, Wuppertal, 2003.

[89] P. Avery. *Fitting Theory I: General Least Squares Fitting Theory*. CBX 91-72, Gainesville, 1991.

[90] L. Buggem and J. Myrheim. Tracking and Track Fitting. *Nucl. Instr. Meth.*, 179, 1981.

[91] W. Liebig, K. Prokofiev, and A. Wildauer et al. Vertex Reconstruction in the ATLAS Experiment at the LHC. Technical Report ATL-INDET-PROC-2008-003, CERN, Geneva, Switzerland, 2008.

[92] S. Agostinelli et al. GEANT4: A simulation toolkit. *Nucl. Instrum. Meth.*, A506:250–303, 2003.

[93] A. Gaponenko. Monte Carlo Truth for Tracking. Talk given at the LBNL Tracking Jamboree, April 2007.

[94] J. F. Grosse-Oetringhaus and C. E. Jørgensen. Measuring the Pseudorapidity Density of Primary Charged Particles using the TPC. Technical Report ALICE-INT-2007-005, CERN, Geneva, Switzerland, 2008.

[95] M. Leyton. Measuring the pseudorapidity and transverse momentum distributions of charged particles at $\sqrt{s} = 14$ TeV. Technical Report ATL-COM-PHYS-2007-051, CERN, Geneva, Switzerland, 2007.

[96] G. Arnison et al. Transverse momentum spectra for charged particles at the CERN Proton-Antiproton Collider. *Phys. Lett.*, 118B:167–172, 1982.

[97] C. Tsallis. Possible Generalization of Boltzmann-Gibbs Statistics. *J. Stat. Phys.*, 52:479–487, 1988.

[98] T. S. Biro, G. Györgyi, A. Jakovac, and G. Purcsel. A non-conventional description of quark matter. *J. Phys. G*, 31:S759–S763, 2005.

[99] CMS Collaboration. Measurement of charged hadron spectra in proton-proton collisions at $\sqrt{s} = 14$ TeV. Technical Report CMS PAS QCD_07_001, CERN, Geneva, Switzerland, 2008.

[100] A. Rossi. Residual gas density estimations in the LHC insertion regions IR1 and IR5 and the experimental regions of ATLAS and CMS for different beam operations. Technical Report LHC Project Note 783, CERN, Geneva, Switzerland, 2004.

[101] LHC Commissioning Work Group, `http://lhccwg.web.cern.ch/lhccwg/`.

[102] LHC Commissioning with Beam, `http://lhc-commissioning.web.cern.ch/lhc-commissioning/`.

[103] P. A. Aarnio et al. FLUKA86: User's Guide. *CERN TIS-RP/168*, 1986.

[104] A. Fasso et al. FLUKA: Performances and applications in the intermediate energy range. *Meeting on Shielding Aspects of Accelerators, Targets and Irradiation Facilities*, 1994.

[105] B. Cooper. Alignment of the ATLAS Inner Detector. Technical Report ATL-INDET-PROC-2008-007, ATL-COM-INDET-2008-024, CERN, Geneva, Switzerland, 2008.

[106] T. Goettfert, G. Gorfine, and J. Schieck et al. InDetResidualMisalignment Twiki. https://twiki.cern.ch/twiki/bin/view/Atlas/InDetResidualMisalignment.

[107] E. Bouhova-Thacker et al. Impact of Inner Detector and Muon Spectrometer Misalignments on Physics. Technical Report ATL-COM-GEN-2009-022, CERN, Geneva, Switzerland, 2009.

[108] T. Golling. Validation of Day 1 Alignment. http://golling.web.cern.ch/golling/Alignment_Day1Validation_02042009.pdf.

[109] S. Kersten. Requirements for the Power Supply System of the ATLAS Pixel Detector. Technical Report ATL-IP-ES-0005, CERN, Geneva, Switzerland, 2000.

[110] K. Einsweiler et al. Requirements for the Pixel Detector Services. Technical Report ATL-IP-ES-0007, CERN, Geneva, Switzerland, 2000.

[111] Kersten S and P. Kind. Technical Description of the Interlock Circuit and System for the ATLAS Pixel Detector. Technical Report ATL-IP-ES-0041, CERN, Geneva, Switzerland, 2001.

[112] M. Citterio, A. Eyring, M. Garcia-Sciveres, and S. Kersten. Pixel Electrical Services. Technical Report ATL-IP-ES-0069, CERN, Geneva, Switzerland, 2003.

[113] M. Citterio and C. Meroni. Pixel PP2 Patch Panels Design. Technical Report ATL-IP-ES-0074, CERN, Geneva, Switzerland, 2003.

[114] M. Citterio et al. Voltage-regulation stations for the distributed power supply system of the ATLAS pixel detector. In *Proceedings of the Nuclear Science Symposium Conference*, October 2007.

[115] S. Kersten and P. Kind. Pixel PP3 Patch Panels Design. Technical Report ATL-IP-ES-0075, CERN, Geneva, Switzerland, 2003.

[116] T. Flick, S. Kersten, P. Kind, and S. Kirichu Nderitu. The Power Supply and Control System for the Opto Link of the ATLAS Pixel Detector. Technical Report ATL-IP-ES-0106, CERN, Geneva, Switzerland, 2004.

[117] S. Kersten and P. Kind. The Interlock Matrix of the Pixel Detector Control System. Technical Report ATL-IP-ES-0110, CERN, Geneva, Switzerland, 2004.

[118] S. Kersten and P. Kind. Overview on the Pixel DCS Hardware. Technical Report ATL-IP-CD-0002, CERN, Geneva, Switzerland, 2006.

[119] M. Leyton. Service Tests for the ATLAS Pixel Detector. Technical Report ATL-IP-QA-0026, CERN, Geneva, Switzerland, 2007.